AN ABSTRACT OF THE THESIS OF

WEN-HSIUNG CHEN (Name) for the degree Doctor of Philosophy (Degree)

in PHYSICS (Major Department) presented on March 4, 1975 (Date)

Title: THERMALLY LIMITED SPIN-BATH RELAXATION OF TRIVALENT CERIUM IONS IN CALCIUM FLUORIDE

Redacted for privacy

Abstract approved: H. T. Easterday

Spin-bath relaxation times τ of $Ce^{3+}:CaF_2$ immersed in liquid helium have been measured in external magnetic fields ranging from approximately 1 to 20 kG. In an effort to heat the spin system of the Ce ions, the field was rapidly increased by superimposing a field increment ($\Delta H \simeq 0.3 \sim 0.7$ kG) in a time interval of the order of 10^2 μsec on the dc background field. The full range of magnetic field values was achieved by varying the dc background field. The return to equilibrium at the bath temperature ($\sim 2^{\circ}K$) was determined by monitoring the instantaneous paramagnetic Faraday rotation of the Ce^{3+} ions. The results indicate that the spin-lattice coupling between the Ce ions and the CaF_2 lattice is very strong. In samples containing 0.5, 1.0, and 3.0 at. % Ce^{3+} with the field applied parallel either to the crystal [100] or [111] axis the spin-lattice relaxation time T_1 is

less than 0.1 msec for all temperatures and fields examined. This result cannot be interpreted in terms of commonly known relaxation processes.

The overall return to equilibrium (spin-bath relaxation) at the bath temperature proceeds in an exponential fashion for fields in the range 5$\sim$15 kG with characteristic time constants of 1 to 10 msec. It has been shown that under certain conditions a strongly coupled spin-phonon system whose common relaxation to the temperature of the liquid helium bath is limited by the rate of energy exchange across the crystal-bath interface (Kapitza limitation) exhibits an exponential time dependence. In order that such relaxation times not be incorrectly identified as the spin-lattice relaxation time it is imperative that their magnetic field dependence be examined. The spin-bath relaxation time takes the form $\tau = r_k C_c$, where r_k is the Kapitza resistance per unit crystal-bath interfacial area and C_c is the total heat capacity of the crystal. Investigation of the spin-bath relaxation of Ce^{3+}:CaF_2 has allowed:

(1) An order of magnitude of the Kapitza resistance per unit interfacial area, r_k, for CaF_2 to be determined as $10^{\circ}K/Watt$ at $T \simeq 2^{\circ}K$, which is somewhat larger than that of most other dielectrics measured to date.

(2) The Schottky specific heat of the 3% Ce^{3+} spin system to be estimated by assuming that all samples examined possess effectively

the same value of r_k. This then yields, as an example, $C_s/Nk \simeq 0.05$ at $H/T = 7$ kG/^{o}K. It follows from this that the field switching method can serve as a dynamic means for examining the "Schottky specific heat" of any strongly coupled spin-phonon system as long as the Kapitza limitation exists between the host crystal and the helium bath.

(3) The lattice heating resulting in a crystal temperature rise, δT, to be estimated for the extreme case of $C_s \simeq C_c >> C_L$, where C_s and C_L are respectively the spin and phonon heat capacities. The maximum value of δT so observed was 0.2^{o}K. As a result of this, the possibility arises that the field switching method could serve as a means of contactless heating of dielectrics through the intermediary of doped paramagnetic impurities.

Additionally, it is felt that much of the scatter in "spin-lattice" relaxation times appearing in the literature for which only a temperature dependence has been investigated may arise from insufficient consideration having been given to the role of the surface boundary resistance.

Thermally Limited Spin-Bath Relaxation of Trivalent Cerium Ions in Calcium Fluoride

by

Wen-Hsiung Chen

A THESIS

submitted to

Oregon State University

in partial fulfillment of
the requirements for the
degree of

Doctor of Philosophy

June 1975

APPROVED:

Redacted for privacy

Professor of Physics
in charge of major

Redacted for privacy

Chairman of Department of Physics

Redacted for privacy

Dean of Graduate School

Date thesis is presented March 4, 1975

Typed by Mary Jo Stratton for Wen-Hsiung Chen

ACKNOWLEDGEMENTS

Grateful acknowledgement is made to my major professor, Dr. David J. Griffiths, for his interest, guidance, and counsel during the course of this work. The research was supported by a grant from the Research Corporation; part of this grant provided support as a research assistant during the summer terms. This is gratefully acknowledged. Dr. Harry T. Easterday deserves thanks for standing in as major professor while Dr. Griffiths was on leave. Thanks also go to the other members of my committee, Drs. Allen L. Wasserman, Melvin Cutler, and Clifford E. Fairchild, as well as to former committee member Dr. Wilson Au.

I would also like to extend my appreciation to Dr. H. Hollis Wickman and to members of his group in the Department of Chemistry for their helpful discussions and for providing an excellent EPR spectrometer.

Finally, I wish to acknowledge my wife, Yin-tze, whose love, patience, and understanding have played an important role in the final stage of completion of this degree.

TABLE OF CONTENTS

LIST OF TABLES

LIST OF FIGURES

THERMALLY LIMITED SPIN-BATH RELAXATION OF TRIVALENT CERIUM IONS IN CALCIUM FLUORIDE

1. INTRODUCTION

Assume that an experimental arrangement can be visualized to consist of three parts--a spin system, a lattice (phonon) system, and a bath (heat reservoir) as illustrated in Fig. 1. Besides the constant temperature of the bath (T_B), T_s and T_L are designated to be the respective temperatures of the spin and phonon systems. It is our intention to investigate the propagation of energy from the source of disturbance through the spin system into the heat reservoir. A study of the rate at which T_s, via certain processes, returns to T_B after the system has been disturbed will be the subject of this work. Since the complete relaxation process is inherently a two-step one, the rate of energy transfer between spins and bath depends on the coupling not only between spins and phonons but also between phonons and bath. Therefore, depending on the strength of coupling between the systems, the experimentally measurable spin-bath relaxation time, τ, will be largely determined by whether T_1, the spin-lattice relaxation time, or τ_{ph}, the phonon lifetime, is longer.

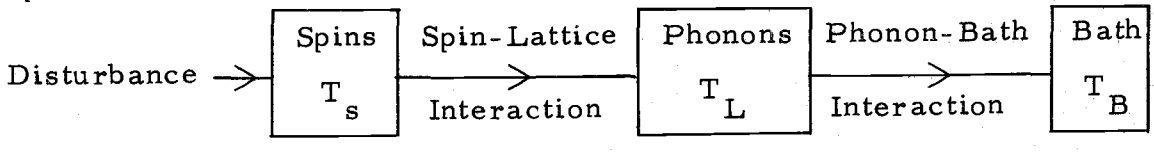

Figure 1. Schematic representation of the energy flow from the spin system through the phonon system to the bath.

In a more realistic picture one should separate the lattice system into hot phonons and thermal phonons and be aware of the presence of other spin species between which cross-relaxation might occur. By hot phonon we mean those excess phonons with energies approximately equal to the spin energy level spacings. Figure 2 indicates that hot phonons can relax by either transferring their energy to the bath directly, or they can pass it on to other phonons by inter-phonon processes. Figure 1 thus implies that inter-phonon coupling is stronger than the hot phonon-bath coupling. Different spin species in our case may appear in the forms of clusters or different Zeeman species (i.e., spins of different spectroscopic splitting factors, the g values). Since the exchange interaction between rare-earth ions in a crystal is in general fairly weak, we do not expect any serious clustering effect. The cross-relaxation between Zeeman species also seems unlikely because of the relatively large difference in their g-values and since the method of disturbing spins affects all spins. The most general situation is illustrated in Fig. 2.

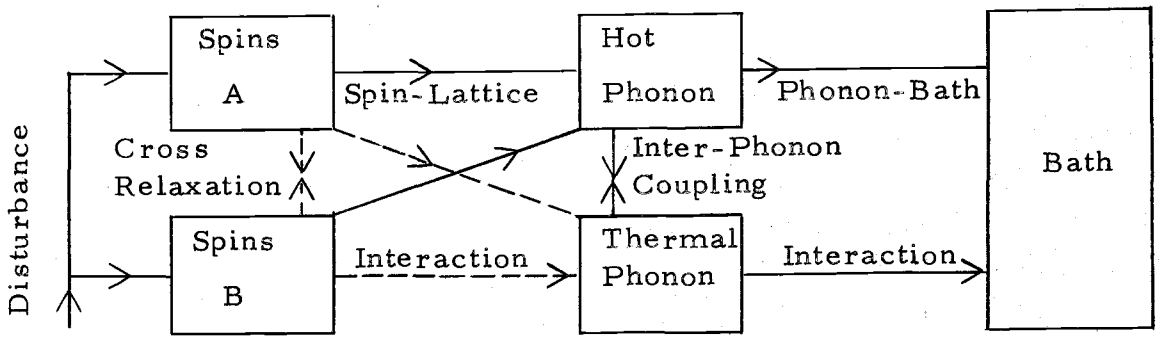

Figure 2. Relaxation diagram showing all possible processes. Those not occurring in our system are indicated by dashed lines.

In our investigation, the spin system was heated by rapid field switching through adiabatic magnetization. Since the entrophy of a simple spin system at $kT >> g\beta H$ (where β is the Bohr magneton) is a linear function of H/T, the final adiabatic spin temperature can be given by $T_f = (H_f/H_i)T_B$, where H_f and H_i are respectively the final and initial external magnetic fields. The rise of temperature is $\delta T = T_f - T_B = (\Delta H/H_i)T_B$, where $\Delta H \equiv H_f - H_i$. This heating technique was first described by Kalbfleisch (1, 2) and Daniels and Rieckhoff (3). The subsequent return to the equilibrium bath temperature (T_B) revealed in the differential spin population was monitored by observing the instantaneous paramagnetic Faraday rotation of the ion. The fact that the Faraday rotation can be used to detect changes in spin population was first predicted by Kastler (4). A theory including various types of disturbance was developed by Opechowski (5). The influence of paramagnetic resonance on the Faraday rotation was first detected by Daniels and Wesemeyer (6) in neodymium ethylsulphate (NdES). Subsequently Daniels and Rieckhoff (3), and also Rieckhoff and Griffiths (7), used the effect to measure the spin-lattice relaxation time of NdES by microwave pulsing. Griffiths and Glättli (8) employed the same technique to study spin-lattice relaxation phenomena in PrES. Other work on rare-earth ethylsulphates has been done by combined methods of Faraday effect and periodic field pulsing (1, 9, 10).

The trivalent cerium ion, Ce^{3+}, was chosen to constitute the spin system for the work described in this thesis. The reasons are the following:

(1) It has the simplest atomic and nuclear structure of paramagnetic ions in the rare-earth group, having one unpaired electron in the 4-f subshell and a nuclear spin of zero, the latter fact precludes any hyperfine interaction and should simplify the spin-lattice part of the overall relaxation a great deal.

(2) It is a Kramers ion of which the Zeeman energy levels are fully controllable by an external magnetic field and whose coupling with the lattice is expected to be weak (this implies very long spin-lattice relaxation times could be anticipated).

(3) The system possesses appreciable paramagnetic Faraday rotation which is necessary in view of the technique we employ.

(4) The field dependence of the spin-phonon-bath relaxation of Ce^{3+} : CaF_2 immersed in liquid helium has never been investigated.

The Ce^{3+} ion is doped into a CaF_2 crystal as an impurity. Electron paramagnetic resonance (EPR) spectroscopic study of this system was first reported by Baker et al. (11). The temperature dependence of the spin-lattice relaxation time of Ce^{3+}:CaF_2 as well as other rare-earth ions in CaF_2 was measured by Bierig et al. (12). Zapasskii et al. (13, 14, 15) made an intensified study of spin-lattice relaxation of Dy^{3+} in CaF_2 and also the CaF_2:Dy^{3+} system. Both

temperature and field dependent spin-lattice relaxation of $Tm^{2+}:CaF_2$, SrF_2, and BaF_2 were reported by Sabisky et al. (16). Our work was mainly concentrated on the field dependence of spin-bath relaxation processes of $Ce^{3+}:CaF_2$ in various concentrations of Ce^{3+} ion and crystallographic orientations. The necessity of a field dependent study of this system (and others) lies in the fact that any of the common spin-lattice relaxation processes, especially the direct process, arising from crystal field theory cannot be identified solely by temperature dependence unless there is also an indication of correct field dependence. During the experiment, an EPR spectrum of each of the $Ce^{3+}:CaF_2$ crystals was first taken to identify the site symmetry of the ion, which is necessary in the calculations of spin-lattice relaxation times and spin specific heats. The optical calibration of each crystal involving the measurement of the Faraday rotation of the ion versus the field at nearly constant temperatures then followed. This enabled us to obtain the maximum response signal in the observation as well as linearity of response at each field switching as detailed in Chapter 3. The results indicate a very strong spin-lattice coupling such that T_L is almost the same as T_s over a wide range of the values of magnetic field with the two temperatures subsequently relaxing to T_B together. The process appears to be limited by the phonons at the boundary of the crystal, due to acoustic mismatch between it and the liquid helium.

In 1941 Kapitza (17) observed the existence of a small temperature difference, δT, between the wall of a metal and the bulk of liquid helium (at T_B) caused by a boundary resistance, the Kapitza resistance R_k, to the flow of thermal current across the surface. The processes causing heat exchange between a solid body and helium II were discussed by Khalatnikov (18), Challis et al. (19) and others. Fairly detailed reviews on this topic have been given by Pollack (20) and, most recently, by Challis (21). For small δT ($\delta T << T_B$), R_k can be defined by $\delta T = R_k f$, where f is the thermal current density. If one equates the time rate of change of the internal energy of the combined spin-lattice system (which we will call crystal for short) to the Kapitza limited thermal current and solves the differential equation under the assumption that the spin specific heat is much greater than the phonon specific heat, one finds that the boundary resistance limited spin-bath relaxation time τ can be given by $\tau = R_k C_c / S$, where C_c is the heat capacity of the crystal and S is the crystal-bath interfacial area. The dependence of τ on R_k was first proposed by Van den Broek et al. (22) in their work on spin-lattice relaxation in rare-earth ethylsulphate. Glättli (23) utilized the preceding ideas to measure R_k between CeES and liquid helium II. A related theoretical analysis, based on the Kapitza resistance, of the experimental data for PrES measured by Griffiths et al. (8) was also reported in the same year by Atsarkin (24).

Our results indicate that the spin-bath relaxation process of our system (Ce^{3+}x%:CaF_2)is limited by the Kapitza resistance. In all crystals, the T's were found to be proportional to R_k. The measured R_k's are of the order of 100 $cm^2 \cdot {}^oK$/watt (for a crystal with interfacial area $S \simeq 10$ cm^2) and appear to be independent of magnetic field at fixed temperature within the range of applicability of the Kapitza resistance model. Our results also show clearly that relaxation measurements made at a given magnetic field present all the appearance of true spin-lattice behavior. The correct identification of the processes taking place can only be made when the response of the relaxation times over an extensive field range is examined.

Chapter 2 of this thesis summarizes theoretical background relevant to the present study. Chapter 3 deals with some details of interest in connection with the experimental apparatus and procedures. In Chapter 4 the experimental data are presented and discussions are given in Chapter 5. The last chapter, Chapter 6, contains a summary of conclusions drawn from the foregoing chapters.

2. THEORETICAL BACKGROUND

2-1. Trivalent Cerium as an Impurity in CaF_2

(1) The Ce^{3+} Ion

Cerium, $_{58}Ce^{140}$, is the first element of a series of 14 elements whose 4f-subshell is incomplete. The series is known as the first inner transition series or rare-earth elements. The Cerium atom has an electronic configuration $(1s^2)(2s^2 2p^6)(3s^2 3p^6 3d^{10})(4s^2 4p^6 4d^{10} 4f^1)(5s^2 5p^6 5d^1)(6s^2)$ which becomes a trivalent ion by losing the 3 electrons in the 5d and 6s subshells. The unpaired 4f electron is optically and magnetically active and is responsible for the ground ^2F term. In the case of the free ion, the ^2F term is further split by the spin-orbit interation into $^2F_{5/2}$ and $^2F_{7/2}$ with the former lying lower and the separation between them being approximately 2253 cm^{-1} (25).

(2) The Host Crystal, CaF_2

Calcium fluoride has a crystalline structure (26) which can be visualized as a cubic lattice of fluorine ions in which every other body center is occupied by a divalent calcium ion. The lattice constant a is 5.4527 Å at 25°C and 5.4355 Å at 6.4°K (27). Trivalent cerium ions enter the crystal by substituting for Ca^{2+} ions and in so doing create

the need of a charge compensation mechanism which, in turn, changes the point group symmetry at the site of Ce^{3+} (11, 26). The most common method of such compensation is achieved by placement of a F^- ion in one of the six nearest-neighbor interstitial sites at a distance a/2 as shown in Fig. 3. The presence of the extra F^- ion changes the crystal field symmetry at the Ce^{3+} site from cubic (O_h) to tetragonal (C_{4v}). A less common but still possible way is by insertion of a F^- ion at (a/2, a/2, a/2); an even lower site symmetry, trigonal (C_{3v}), is then felt by the Ce^{3+} ion.

(3) Ground State of Ce^{3+} in CaF_2 —Crystal Field Treatment

From the electronic configuration of the cerium ion we readily see that the 4f electron, like those of the other rare-earth ions, is at least partially shielded from outside influences by those electrons in the 5s and 5p subshells. As a result the crystal field interaction is considerably reduced from that found in the other transition ions of the 3-d group and thus becomes much weaker than the spin-orbit interaction in such a way that the total angular momentum J remains nearly a good quantum number. This then allows us to restrict our consideration to the ground J manifold, $^2F_{5/2}$.

To approach the problem by crystal field treatment we first write down the Hamiltonian of the system; Ce^{3+} ion situated in

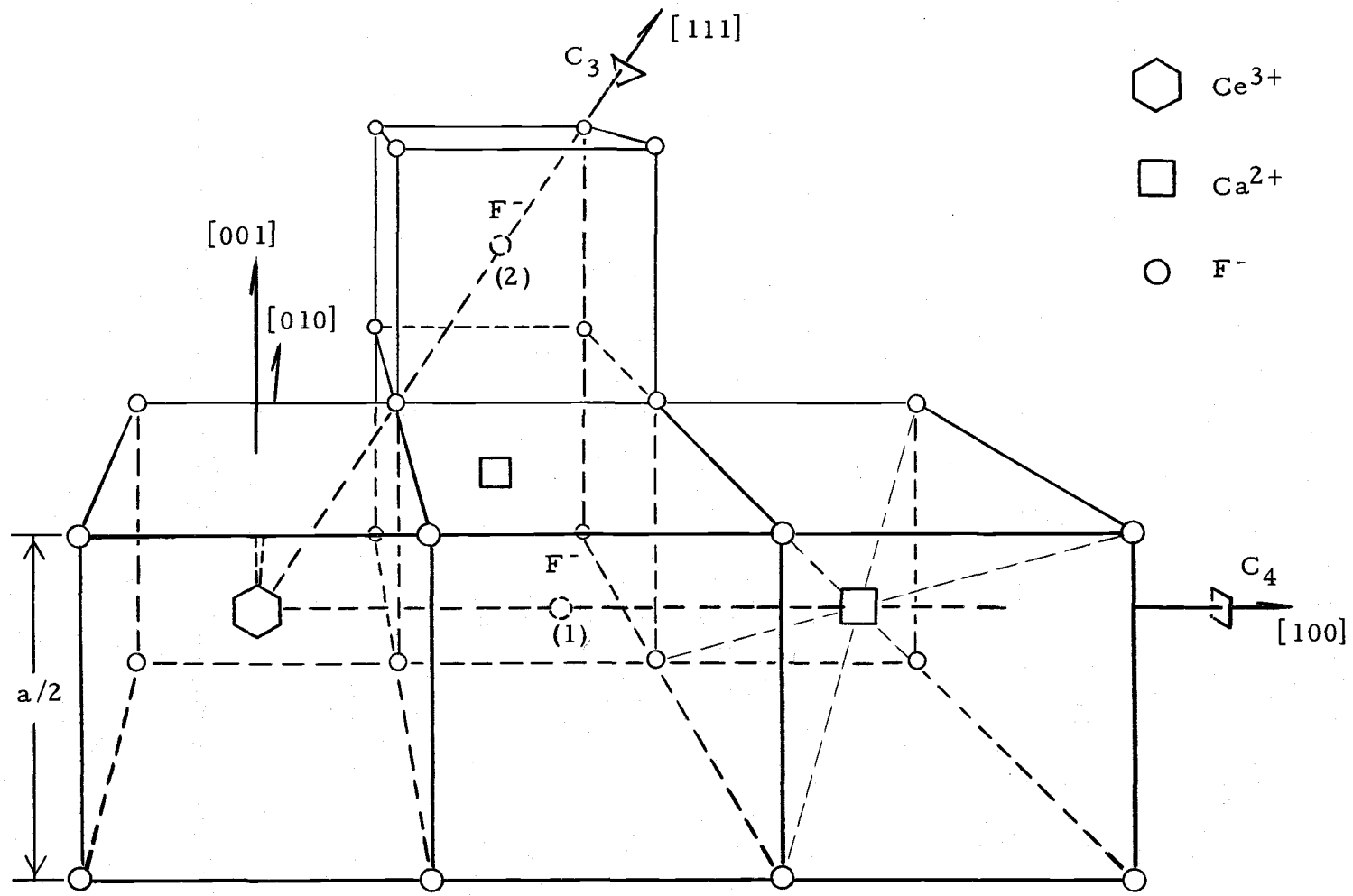

Figure 3. Crystal structure of CaF_2 and site symmetries of Ce^{3+}. The figure shows 0_h symmetry of Ca^{2+} site, C_{4v} symmetry of Ce^{3+} site when F^- is at position (1), and C_{3v} symmetry of Ce^{3+} when F^- is at position (2).

certain crystal site symmetry:

$$\mathcal{H} = \mathcal{H}_0 + V_c ,$$

where $\mathcal{H}_0$ is the free ion energy including spin-orbit interaction and V_c is the weak crystal field perturbation. Assuming no overlapping of paramagnetic ion wavefunctions onto the ligands, V_c satisfies Laplace's equation, $\nabla^2 V_c = 0$, and has a general solution expressible by spherical harmonic functions $Y_n^m(\hat{r})$.

$$V_c = \sum_{n,\,m} A_n^m \, r^n \, Y_n^m (\hat{r}) .$$

If we examine matric elements such as $\langle Jm_J | V_c | Jm'_J \rangle$ the properties of which are determined by $\langle Lm_L | V_c | Lm'_L \rangle$ with L = 3 for a 4f electron, we see that non-zero elements occur only for even integer values of n and terminate at n = 6. Actually, if the calculation is restricted to within the J = 5/2 manifold, the resultant maximum value of n is 4. Hence V_c takes the form

$$V_c = \sum_{\substack{n=0,2,4 \\ -n \le m \le n}} A_n^m \, r^n \, Y_n^m (\hat{r}) .$$

The perturbation, V_c, must also reflect the symmetry of the crystal field. If a tetragonal (C_{4v}) field symmetry is assumed, the 4-fold rotations in C_{4v} require m = 0,4, 8, ... Thus, V_c can be further simplified to

$$V_c = A_0^0 + A_2^0 r^2 Y_2^0 + A_4^0 r^4 Y_4^0 + A_4^4 r^4 Y_4^4 + A_4^{-4} r^4 Y_4^{-4} .$$

Rather than evaluate the matrix elements of V_c directly, it is more common to employ the operator equivalent method developed by Stevens (28). Following his method, we first cast Y_n^m into Cartesian coordinates, then use the total angular momentum operators to replace the coordinate operators. The substitution needs only numerical corrections plus consideration of the hermiticity of the angular momentum representation of the crystal field interaction V_c. Thus

$$V_c = A_2^0(3z^2-r^2) + A_4^0(35z^4-30r^2z^2+3r^4) + A_4^4(x^4-6x^2y^2+y^4)$$

implies $V_c = A_2^0\langle r^2\rangle\chi_2\hat{O}_2^0 + A_4^0\langle r^4\rangle\chi_4\hat{O}_4^0 + A_4^4\langle r^4\rangle\chi_4\hat{O}_4^4$, where $\hat{O}_2^0 = 3J_z^2 - J(J+1)$, $\hat{O}_4^0 = 35J_z^4 - [30J(J+1)-25]J_z^2 - 6J(J+1) + 3J^2(J+1)^2$, $\hat{O}_4^4 = \frac{1}{2}(J_+^4+J_-^4)$, and the parameter χ_2 and χ_4 are just Stevens' α and β (28). For Ce^{3+}, $\alpha = \chi_2 = -2/35$ and $\beta = \chi_4 = 2/7x45$. Note that the constant term A_0^0 in V_c has been dropped and the last term is a linear combination of Y_4^4 and Y_4^{-4}. It is common to lump χ_n, $\langle r^n\rangle$, and A_n^m together and call $B_n^m \equiv \chi_n A_n^m\langle r^n\rangle$ the crystal field parameter, which can be obtained experimentally from optical absorption measurements. Finally we write V_c as

$$V_c = B_2^0\hat{O}_2^0 + B_4^0\hat{O}_4^0 + B_4^4\hat{O}_4^4 .$$

When ordinary static perturbation theory is employed, V_c partially removes the degeneracy in $J = 5/2$ manifold by splitting it into three doublets. This is consistent with the result predicted both from

Kramers' theorem (29) and crystal point group considerations. The energy shifts and wave functions can be listed as follows:

Energies	Wave functions
$E_3 = E_0(J=5/2) + \epsilon_+$	$\cos\theta \mid \pm 3/2> - \sin\theta \mid \mp 5/2>$
$E_2 = E_0(J=5/2) + \epsilon$	$\mid \pm 1/2>$
$E_1 = E_0(J=5/2) + \epsilon_-$	$\cos\theta \mid \mp 5/2> + \sin\theta \mid \pm 3/2>$

where $$\epsilon_{\pm} = 4(B_2^0 - 15B_4^0) \pm 6[(B_2^0 + 20B_4^0)^2 + 20(B_4^4)^2]^{1/2}, \qquad (2-1-1)$$

$$\epsilon = -8(B_2^0 - 15B_4^0), \qquad (2-1-2)$$

and $$\tan 2\theta = 2\sqrt{5}B_4^4 / (B_2^0 + 20B_4^0). \qquad (2-1-3)$$

When a magnetic field H is applied the doublets are split by an amount proportional to H. The relation $\Delta E = g\beta H$, where ΔE is the energy spacing and β is the Bohr magneton, defines g, the spectroscopic splitting factor. Suppose H is applied parallel to the crystal C_{4v} axis (taken as z-axis), the splitting of the lowest ground doublet is $\Delta E = 2\Lambda\beta H <a \mid J_z \mid a> = g_{\parallel}\ \beta H = 2\Lambda\beta H <b \mid J_z \mid b>$, where $\mid a>$ and $\mid b>$ are the wave vectors of E_1 with $\mid a>$ taking the bottom signs, and $\Lambda = 6/7$ is the Lande splitting factor. This yields $g_{\parallel} = \Lambda(4\cos 2\theta + 1)$. On the other hand, if H is perpendicular to the z-axis, the splitting becomes $\Delta E = 2\Lambda\beta H <a \mid J_x \mid b> = 2\Lambda\beta H <a \mid J_y \mid b> = g_{\perp}\beta H$, which yields $g_{\perp} = \sqrt{5}\sin 2\theta$. The experimental values of g (11) are $g_{\parallel} = 3.038 \pm 0.003$ and $g_{\perp} = 1.396 \pm 0.002$. Employing these values and relations for $g_{\parallel}(\theta)$ and $g_{\perp}(\theta)$, we found $\tan 2\theta \simeq 1.15$, which, in turn, yields

the calculated values of g; $g_{\parallel} = 3.11$ and $g_{\perp} = 1.45$. The energy spacing $\Delta_1 = E_2 - E_1 \simeq 110\ cm^{-1}$ and $\Delta_2 = E_3 - E_1 \simeq 579\ cm^{-1}$ has been recently measured by Manthey (30) from fluorescence. We shall show this in Fig. 4. Using the known values of $\tan 2\theta$, Δ_1, and Δ_2, we found the values of crystal parameters from eq's. (2-1-1, 2, 3) $B_2^0 = -5.02\ cm^{-1}$, $B_4^0 = -1.33\ cm^{-1}$, and $B_4^4 = -8.14\ cm^{-1}$.

When the Ce^{3+} ion is situated in a trigonal (C_{3v}) crystal field symmetry, the perturbation assumes the form (31)

$$V_c = B_2^0 \hat{O}_2^0 + B_4^0 \hat{O}_4^0 + B_4^3 \hat{O}_4^3 .$$

Similar calculations then give $g_{\parallel} = 3\Lambda = 18/7 \simeq 2.57$ and $g_{\perp} = \Lambda = 6/7 \simeq 0.86$, which are to be compared with the experimental values (31) $g_{\parallel} = 2.38 \pm 0.03$ and $g_{\perp} < 0.1$.

The perturbation describing the undistorted cubic (O_h) crystal field symmetry may be written as (31)

$$V_c = B_4^0(\hat{O}_4^0 + 5\hat{O}_4^4) + B_6^0(\hat{O}_6^0 - 21\hat{O}_6^4).$$

Under the action of V_c the ground $J = 5/2$ manifold splits into a doublet (Γ_7) and a quartet (Γ_8), the latter being lower in energy (32). Allowed transitions within the split quartet when H is parallel to a crystal C_4 axis yield $g = 7\Lambda/3 = 2$ and $11\Lambda/3 \simeq 3.14$ which are to be compared with the experimental values (33) $g = 2.00$ and 3.1 ± 0.1.

In the foregoing calculation we have assumed complete ionic binding in the crystal and used the so-called "point charge" crystal

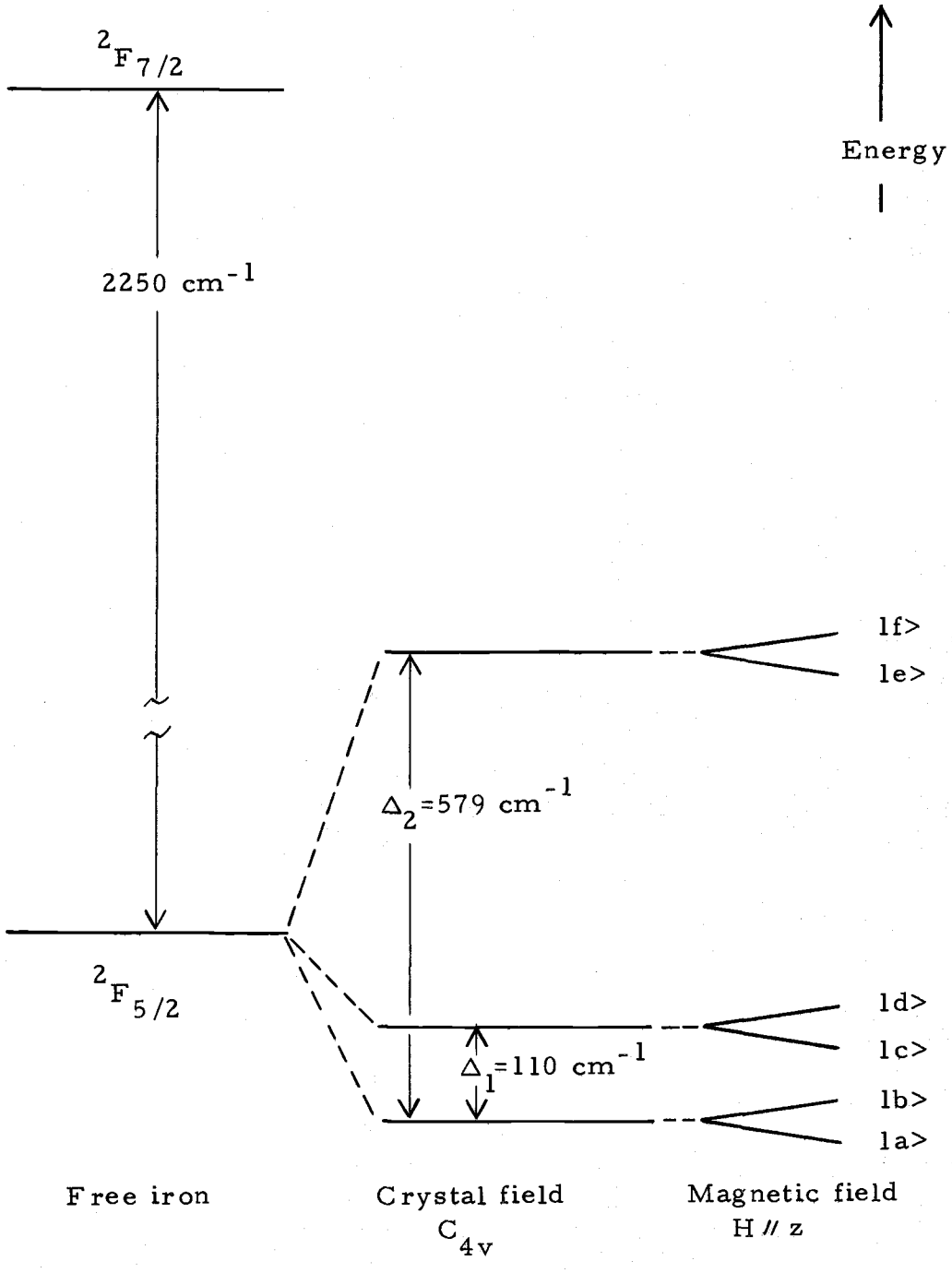

Figure 4. Energy level diagram of tetragonal site symmetry of Ce^{3+} in CaF_2 (Zeeman splittings are greatly exagerated).

field theory. This model gives fairly good qualitative account of the magnetic properties of these paramagnetic ions. Although the molecular field theory makes the model more realistic and renders closer agreement with experiments in some aspects, it plays no role in the magnetic behavior of these ions.

Additionally, it should be noted that at liquid helium temperatures only the lowest Kramers degenerate state will have appreciable population. Thus all we need to concern ourselves with is this state and transitions arising from it.

2-2. Spin-Lattice Relaxation

Since paramagnetic ions (spins) are imbedded in a crystal host, any change of spin temperature must ultimately be felt by the lattice and some relaxation process must take place to re-establish thermal equilibrium between these two systems. Two major relaxation mechanisms have been proposed. Both have suggested that the dominant spin-lattice coupling is via a thermal modulation of well known static interactions. The first was given by Waller (34) based on dipolar interaction between neighboring paramagnetic ions. Modulation of the dipolar interaction ($\sim r^{-3}$) by lattice vibrations provides the coupling between the spin system and the lattice. This mechanism was found not feasible to account for the relaxation of magnetically dilute salts. The second mechanism based on the interaction of the

paramagnetic ion with the dynamic crystalline field was suggested by Kronig (35), examined in detail by Van Vleck (36), and more recently, by Mattuck et al. (37) for the 3-d group, and Orbach (38) for the rare-earth group. Since our experiment deals with diluted rare-earth ions, we shall concentrate on the second mechanism, and follow Orbach's phenomenological approach in its theoretical treatment.

The Hamiltonian describing the electronic ground state may be taken as $\mathcal{H} = \mathcal{H}_{so} + \mathcal{H}_{c} + \mathcal{H}_{z}$, the terms representing the spin-orbit, crystal field, and Zeeman interactions, respectively. Here we have ignored nuclear effects. As we have stated in §2-1, when an ion is placed in a crystal, spatial isotropy is destroyed by various inhomogeneous electric fields. The free ion energy levels hence are split. In the rare-earth ions the spin-orbit splitting ($\sim 10^{3}$ cm^{-1}) is considerably much greater than the crystal field splitting ($\sim 10^{2}$ cm^{-1}), Δ_1, Δ_2, ..., so that the total angular momentum J stays nearly a good quantum number. Each of the crystal field split levels of a J manifold is therefore expressed by some linear combination of the z-axis projection of J, namely $\{|J, J_z\rangle\}$. For ions with an odd number of electrons each of these states has at least Kramers degeneracy (29). For ions with an even number of electrons, some of the states may be singlets, but we assume that a magnetic doublet lies lowest. The degeneracy of the ground doublet is then lifted by $\mathcal{H}_{z}$. We have called these states $|a\rangle$ and $|b\rangle$ and shall call the other final excited

states $|c\rangle$, $|d\rangle$, ..., etc. Their Zeeman spacing, δ, is in general of the order of 1 cm^{-1}. A typical energy level diagram of this sort is shown in Fig. 4 (not necessarily to scale).

As a result of the point charge approximation, $\mathcal{H}_c$ satisfies the Laplace equation and can be expanded in this manner:

$$\mathcal{H}_c = \sum_{n,m} B_n^m r^n Y_n^m (\hat{r}) , \qquad (2\text{-}2\text{-}1)$$

where we have taken the origin to be at the paramagnetic ion. We shall take ξ to be the coordinate of a ligand ion and expand $B_n^m(\xi)$ in a Taylor's series about the ligand equilibrium position ξ_0. In other words, consideration of thermal fluctuations of the lattice allows us to write down $B_n^m(\xi)$ in following form:

$$B_n^m(\xi) = B_n^m(\xi_0) + (\partial B_n^m/\partial \xi)_0(\xi - \xi_0) + (1/2)(\partial^2 B_n^m/\partial\xi\,\partial\xi')_0(\xi - \xi_0)(\xi' - \xi_0) + \ldots \qquad (2\text{-}2\text{-}2)$$

The quantity $(\xi - \xi_0)$ when divided by ξ yields the lattice thermal strain ϵ, therefore eq. (2-2-1) is expressible by ϵ's if eq. (2-2-2) is employed

$$\mathcal{H}_c = \sum_{n,m} B_n^m(\xi_0) r^n Y_n^m + \epsilon \sum_{n,m} \xi (\partial B_n^m/\partial \xi)_0 r^n Y_n^m + (1/2)\epsilon\epsilon' \sum_{n,m} \xi\xi'(\partial^2 B_n^m/\partial\xi\,\partial\xi')_0 r^n Y_n^m + \ldots ,$$

which is commonly written as $\mathcal{H}_c = V_c + \mathcal{H}_c' + \mathcal{H}_c'' + \ldots$. The first term, $V_c \equiv \sum_{n,m} B_n^m(\xi_0) r^n Y_n^m = \sum_{n,m} V_n^m$, is simply the static crystal

field interaction introduced in §2-1. The second term, $\mathcal{H}_c' \equiv \epsilon \sum_{n,m} \xi (\partial B_n^m/\partial \xi)_0 r^n Y_n^m \simeq -\epsilon \sum_{n,m} V_n^m$, is the lowest time-dependent component of $\mathcal{H}_c$ to first order in the effective thermal strain ϵ and is responsible for the one-phonon direct process, the two-phonon real excitation Orbach process, and the higher order two-phonon virtual excitation Raman process. The third term, $\mathcal{H}_c'' \equiv \frac{1}{2} \epsilon\epsilon' \sum_{n,m} \xi\xi' (\partial^2 B_n^m / \partial\xi \partial\xi')_0 r^n Y_n^m \simeq \epsilon\epsilon' \sum_{n,m} V_n^m$, is the fluctuation in $\mathcal{H}_c$ of second order in the effective thermal strain and contributes also to the higher order two-phonon Raman process. In the above expressions of the dynamic crystal field interaction, the approximations $B_n^m(\xi_0) \simeq -\xi (\partial B_n^m/\partial\xi)_0 \simeq \frac{1}{2} \xi\xi' (\partial^2 B_n^m/\partial\xi\partial\xi')_0$ are made under the assumption $B_n^m(\xi) \propto \xi^{-(p+1)}$, where p is not large enough to alter the order of magnitude of the final results.

(1) The Direct Process

In the direct process, the transition between spin states $|a>$ and $|b>$ is accompanied by absorption or emission of a single phonon of energy δ as illustrated in Fig. 5(A). The direct process spin-lattice relaxation rate, T_{1d}^{-1}, calculated by first-order time dependent perturbation theory under dynamic crystal field interaction $\mathcal{H}_c'$ is given by (39) as

$$T_{1d}^{-1} = (3/2\pi\rho v^5\hbar)(\delta/\hbar)^3 \left| <a| \sum_{n,m} V_n^m |b> \right|^2 \coth(\delta/2kT), \quad (2-2-3)$$

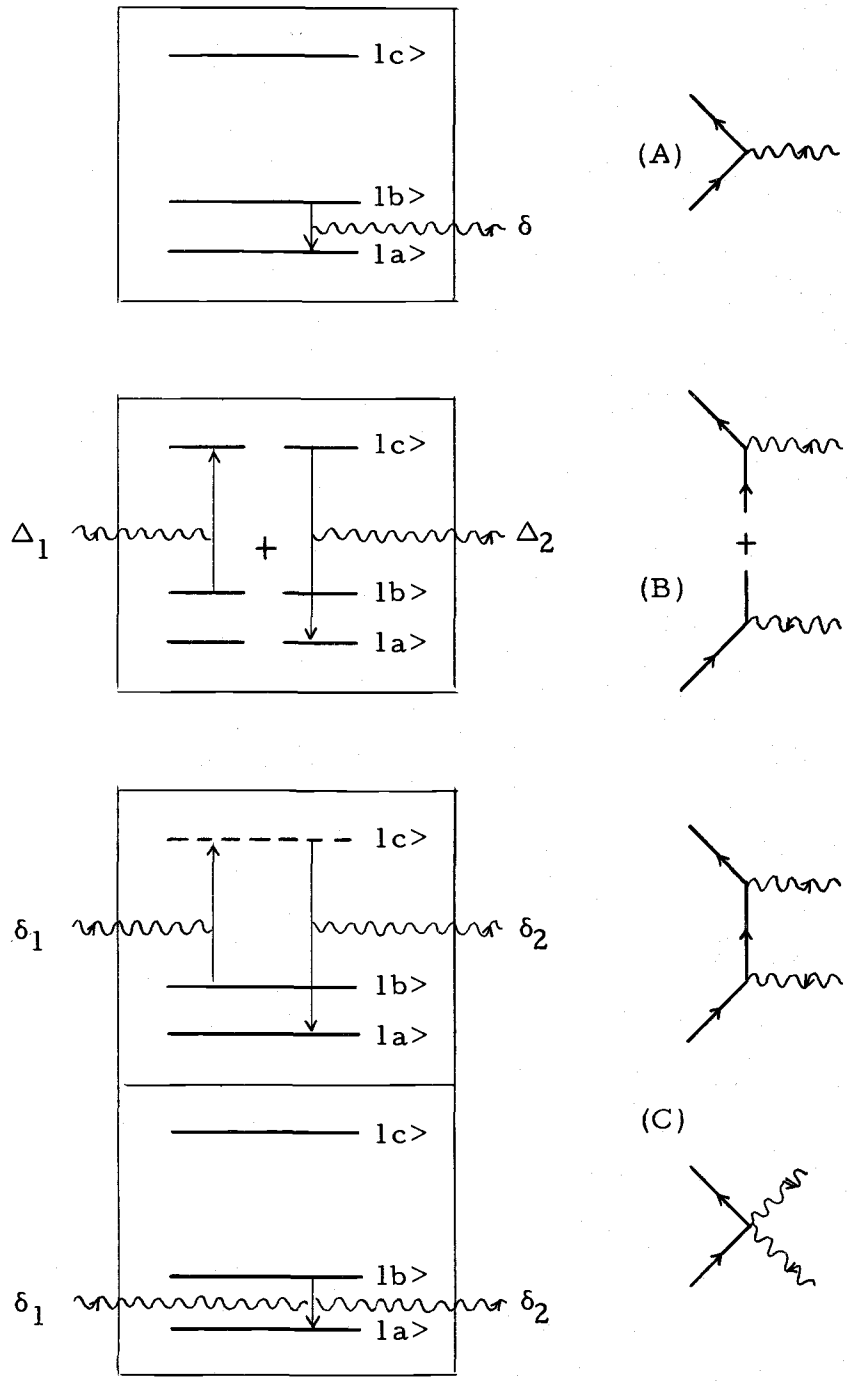

Figure 5. Schematic diagrams to illustrate: (A) the direct process, (B) the Orbach process, and (C) the Raman process.

where ρ is the mass density of the crystal, v is an average phonon velocity, δ is the Zeeman energy spacing between spin states $|a\rangle$ and $|b\rangle$, and V_n^m's are components of the static crystal field interaction. In the case of a Kramers doublet, invariance of the Hamiltonian under time-reversal requires that matrix elements of the crystal field interaction $\langle a|\sum_{n,m} V_n^m|b\rangle$ vanish identically, and we must take account of the admixture of $|a\rangle$ and $|b\rangle$ with $|c\rangle$ and $|d\rangle$, at an energy Δ_1, produced by the Zeeman perturbation $\Lambda\beta\vec{H}\cdot\vec{J}$. The relaxation rate in this case becomes (39)

$$T_{1d}^{-1} = (3/2\pi\rho v^5\hbar)(\delta/\hbar)^3(2\beta\Lambda H/\Delta_1)^2[\langle a|\hat{h}\cdot\vec{J}|c\rangle\langle c|\sum_{n,m} V_n^m|b\rangle + \langle a|\sum_{n,m} V_n^m|c\rangle\langle c|\hat{h}\cdot\vec{J}|b\rangle]^2 \coth(\delta/2kT). \qquad (2\text{-}2\text{-}4)$$

Since $\delta = \beta gH$, when H is not too high at liquid helium temperatures, $\delta << 2kT$, eq. (2-2-4) can be expressed by

$$T_{1d}^{-1} = (12kg^2\beta^4\Lambda^2/\pi\rho v^5\hbar^4\Delta_1^2)[\langle a|\hat{h}\cdot\vec{J}|c\rangle\langle c|\sum_{n,m} V_n^m|b\rangle + \langle a|\sum_{n,m} V_n^m|c\rangle\langle c|\hat{h}\cdot\vec{J}|b\rangle]^2 \cdot TH^4 \equiv A'TH^4, \qquad (2\text{-}2\text{-}4)'$$

where A' is the right-hand side of eq. (2-2-4)', excluding TH^4, and $\hat{h}$ is defined by $\vec{H} = H\hat{h}$. The direct one phonon relaxation rate, T_{1d}^{-1}, for Kramers ions is thus characterized by a fourth power field and a first power temperature dependence.

(2) The Orbach Process

In cases where the crystal field splitting Δ_1 is less than the maximum phonon energy $k\theta_D$, θ_D being the Debye temperature, relaxation between $|a\rangle$ and $|b\rangle$ may proceed by a two-step process involving real transitions to and from an excited state $|c\rangle$ accompanied by the absorption and emission of two phonons having energies of the order of Δ_1 as indicated in Fig. 5(B). The relaxation rate for the Orbach process, T_{1o}^{-1}, has been found (39) to be

$$T_{1o}^{-1} = (3/2\pi\rho v^5\hbar)(\Delta_1/\hbar)^3 \left|\langle a|\sum_{n,m} V_n^m|c\rangle\right|^2 \cdot \exp(-\Delta_1/kT)$$

$$\equiv B \cdot \exp(-\Delta_1/kT). \qquad (2\text{-}2\text{-}5)$$

In the case of a Kramers ion, $\left|\langle a|\sum_{n,m} V_n^m|c\rangle\right|^2$ must be replaced by $\sum_c \left|\langle a|\sum_{n,m} V_n^m|c\rangle\right|^2$ where the sum extends over all excited states at energy Δ_1.

(3) The Raman Process

The Raman process involves the simultaneous absorption of a phonon of energy δ_1 and emission of another of energy $\delta_2 = \delta_1+\delta$, along with a transition of the spin from $|b\rangle$ to $|a\rangle$. Figure 5(C) illustrates this inelastic phonon scattering induced spin flip. The Raman relaxation rate has two contributing components. One is computed from first-order time dependent perturbation theory with a second-order perturbation in strain $\mathcal{H}_c'$. The result is (39)

$$(9x6!)/4\pi^3\rho^2v^{10})(k/\hbar)^7 \left|\langle a\left|\sum_{n,m} V_n^m\right|b\rangle\right|^2 T^7 \equiv CT^7. \qquad (2\text{-}2\text{-}6)$$

The other is calculated from second-order time dependent perturbation theory with a first-order perturbation in strain $\mathcal{H}_c$. The result is (39)

$$(9x6!/4\pi^3\rho^2v^{10}\Delta_1^2)(k/\hbar)^7 \left|\langle a\left|\sum_{n,m} V_n^m\right|c\rangle\right.$$

$$\cdot \left.\langle c\left|\sum_{n',m'} V_{n'}^{m'}\right|b\rangle\right|^2 \equiv C''T^7 . \qquad (2\text{-}2\text{-}7)$$

The two components are added to give the relaxation rate $T_{1R}^{-1} = (C+C'')T^7$ for non-Kramers ions at low temperatures.

For Kramers ions in the low temperature region the rate of the first component is replaced by (39)

$$(9!\hbar^2/\pi^3\rho^2v^{10}\Delta_1^4)(k/\hbar)^9 \left|\langle a\left|\sum_{n,m} V_n^m\right|c\rangle\right.$$

$$\cdot \left.\langle c\left|\sum_{n',m'} V_{n'}^{m'}\right|b\rangle\right|^2 T^9 \equiv C'T^9 . \qquad (2\text{-}2\text{-}8)$$

The second component contains a factor $(2\Lambda\beta H/\Delta_1)^2$ and is much smaller than the first component. Thus the rate is commonly given by $C'T^9$ only.

To summarize, we represent the total relaxation rate for Kramers ions, such as Ce^{3+}, by the summation of the rates of three common processes

$$T_1^{-1} = T_{1d}^{-1} + T_{1o}^{-1} + T_{1R}^{-1} = ATH^4 + B \cdot \exp(-\Delta_1/kT)$$

$$+ C'T^9 . \qquad (2\text{-}2\text{-}9)$$

In the above expression not all three terms are competing at all times. For example, at liquid helium temperatures, the field dependent first term, T_{1d}^{-1}, usually dominates.

Most recently, Bernstein et al. (40) have reviewed the preceding common processes and rederived their relaxation rates by utilizing a description of lattice dynamic in terms of normal modes of vibration transforming as spherical harmonics. Their results also show the conventional field and temperature dependencies of these relaxation rates as anticipated.

2-3. Rate Equations for Spin-Phonon-Bath Relaxation

If the characteristic time τ of the spin-bath relaxation is determined mainly by phonon processes, the relaxation is said to be phonon limited and the spin-lattice relaxation is often partially or totally hidden by them. This phenomena is known as the "phonon bottleneck" and was first recognized by Van Vleck (41). Analyses which are valid under certain bottleneck conditions have been reported by Faughnan et al. (42) as well as many others (39, 43, 44). In Stoneham's thermodynamic approach (43) a pair of linearized equations describing the transfer of heat from the spin system to the bath was written in the following manner:

$$\frac{dU_s}{dt} = C_s \frac{dT_s}{dt} = \frac{C_s}{T_1}(T_L - T_s) \qquad (2\text{-}3\text{-}1)$$

$$\frac{dU_L}{dt} = C_L \frac{dT_L}{dt} = \frac{C_s}{T_1}(T_s - T_L) + \frac{C_L}{\tau_{ph}}(T_B - T_L), \quad (2\text{-}3\text{-}2)$$

where U_s and U_L are the internal energy densities of the spin and the phonon systems, T_s and T_L are their respective temperatures, and $C_s = \partial U_s / \partial T_s$ and $C_L = \partial U_L / \partial T_L$ are the corresponding specific heats. T_1 and τ_{ph} are the characteristic times describing the thermal coupling between the systems and are defined by

$$\frac{dT_s}{dt} = -\frac{T_s - T_L}{T_1} \quad \text{and} \quad \frac{dT_L}{dt} = -\frac{T_L - T_B}{\tau_{ph}} .$$

Therefore T_1 is the usual spin-lattice relaxation time and τ_{ph} is the phonon lifetime in the absence of the spin system. It should be noted that the above coupled linear equations (2-3-1) and (2-3-2) are valid only under the assumptions $T_B \simeq T_s$ and $g\beta H << 2kT$ and have been written in various essentially equivalent forms by other authors (39, 42). Solutions of these equations, based on $C_s >> C_L$, exhibit two time constants, τ' and τ:

$$\tau' \simeq \tau_{ph}(1+\sigma)^{-1} ,$$

where $\sigma \equiv C_s \tau_{ph} / C_L T_1$, corresponding to the short time constant associated with equalization of T_s and T_L, and

$$\tau \simeq T_1(1+\sigma)$$

being the long time constant associated with the relaxation to T_B of the equalized T_s and T_L. In the extreme case where $\sigma >> 1$ or $\tau >> \tau'$ we can assign a temperature T_c common to both spin and

phonon systems in the crystal and use one equation with one characteristic time τ to describe the evolution of crystal temperature T_c into T_B

$$\frac{dU_c}{dt} = C_c \frac{dT_c}{dt} = -C_c \frac{T_c - T_B}{\tau} ,$$

where $C_c = C_s + C_L = \partial U_c / \partial T_c$ is the total heat capacity of the crystal. We proceed to find the explicit form of τ when the relaxing process is limited by the Kapitza resistance R_k. From the definition of R_k (Chapter 1) and the equation of continuity of thermal current, we have

$$\frac{dU_c}{dt} = -C_c \frac{T_c - T_B}{\tau} = -fs = -\frac{T_c - T_B}{R_k} S = C_c \frac{d(T_c - T_B)}{dt}$$

or

$$\frac{d}{dt}(T_c - T_B) + \frac{S}{C_c R_k}(T_c - T_B) = 0 . \qquad (2-3-3)$$

The solution of which is readily seen to be

$$T_c - T_B = A \cdot \exp(-St/C_c R_k) = A \cdot \exp(-t/\tau) ,$$

where A is an arbitrary constant of t and $\tau \equiv C_c R_k / S$ is the Kapitza limited spin-bath relaxation time. If at the end of field switching the crystal has a temperature T_c^*, the time evolution of T_c is

$$T_c = T_B + (T_c^* - T_B) \exp(-t/\tau) . \qquad (2-3-4)$$

It is clear that at $t = 0$, $T_c = T_c^*$, and at $t \to \infty$, $T_c = T_B$, with T_c behaving exponentially during the relaxation.

2-4. Faraday Rotation

Since the knowledge of Faraday rotation is indispensable to our experimental method and data analysis, we felt it is relevant to incorporate a brief survey of the theory in this chapter.

By Faraday rotation we mean the rotation of the plane of polarization of linearly polarized light upon traversing a dielectric medium in the presence of a magnetic field H. An empirical equation depicting the rotation in length x may be given by $\phi = VHx$. The factor of proportionality is the Verdet constant to be associated with each medium and frequency of light. The kinematic origin of the rotation is a kind of double refraction in which the stable modes of polarization are right and left circularly polarized waves. Taking the direction of incidence as the x-axis and considering a plane ($\hat{y}$-polarized) wave of amplitude D, we visualize the problem as a linear oscillation decomposed into two circular oscillations with $\hat{\epsilon}_{\pm} = (\hat{y} \pm i\hat{z})/\sqrt{2}$ as the respective left and right circular polarization unit vectors each propagating through the medium with different wave vector $k_{\pm} = n_{\pm}\,\omega/c$. When these waves emerge from the medium of thickness x, their resultant, after recombining, is

$$
\begin{aligned}
&(D/\sqrt{2})\,[\,\hat{\epsilon}_{+}\exp(i\omega t - i\omega n_{+}x/c) + \hat{\epsilon}_{-}\exp(i\omega t - i\omega n_{-}x/c) \\
&\quad = (D/\sqrt{2})\left\{\hat{\epsilon}_{+}\exp[-i\omega(n_{+}-n_{-})x/2c] + \hat{\epsilon}_{-}\exp[i\omega(n_{+}-n_{-})x/2c]\right\} \\
&\qquad\qquad \cdot \exp[i\omega t - i\omega(n_{+}+n_{-})x/2c] \\
&\quad = D\hat{p}\cdot\exp[\,i(\omega t - kx)\,]\,, \qquad (2\text{-}4\text{-}1)
\end{aligned}
$$

where $\hat{p}$ (which is real) is the polarization unit vector of the emerging wave and takes the form:

$$\hat{p} = \hat{y}\cos[\omega(n_+ - n_-)x/2c] + \hat{z}\sin[\omega(n_+ - n_-)x/2c]$$
$$= \hat{y}\cos\theta + \hat{z}\sin\theta \ . \qquad (2\text{-}4\text{-}2)$$

Therefore, the emergent wave is again a plane polarized wave but with its plane of polarization rotated through an angle $\theta = \omega(n_+ - n_-)x/2c$. The rotation per unit length per unit field strength is thus $V = \omega(n_+ - n_-)/2c$.

Classical considerations based on Larmor's theory and a simple atomic model yield the so-called Becquerel formula (45)

$$\phi = \frac{eHx}{2mc^2}\,\omega\frac{dn}{d\omega} \ . \qquad (2\text{-}4\text{-}3)$$

A quantum mechanical treatment, by use of the Kramers-Heisenberg dispersion relation (46) and taking into account the effect of magnetic field on the energy states of the atom, has been applied by Rosenfeld (47) and others. The results of Rosenfeld show, for the case of multiple widths small compared to kT, that when the incident frequency is far removed from any resonance the rotation can be expressed as a sum of terms of two types which are respectively independent of and inversely proportional to the temperature and are usually called the diamagnetic and paramagnetic parts of the Faraday rotation. The diamagnetic terms can be cast into eq. (2-4-3) if the dispersion relation is employed. A general expression of

paramagnetic rotation in a crystal containing a Kramers ion has been given by Kramers (29). Theory for rare-earth ions in crystals was treated by Van Vleck et al. (48) by employing Kramers' result and by taking into account the influence of crystalline field upon the ions. The theory has also been reviewed more recently by Bloembergen et al. (49). The diamagnetic rotation arising from the Zeeman effect and in general being over-shadowed by the paramagnetic rotation at low temperature (48) has been ignored in their treatments and the dominant paramagnetic rotation has been given by

$$\phi_p \propto \sum_m m \cdot \exp(-mg\beta H/kT) , \qquad (2-4-4)$$

provided that only the ground J multiplet is occupied. Although the most general theory probably is the one given by Shen (50) who generalized the Kramers-Heisenberg dispersion relation by considering all multipole transitions and not just the electric dipole transition, his result essentially merges into the Kramers' expression (29) and hence eq. (2-4-4) when the incident frequency is not close to resonance.

The quantity summed over m in eq. (2-4-4) gives rise to a Brillouin function $B_J(x)$, where $x \equiv g\beta H/kT$. Therefore, ϕ_p can be cast into being directly proportional to the magnetization, $\langle M_z \rangle$, of the system. If one introduces a proportionality constant, $\phi_\infty(s, \omega, l)$, known as the saturation rotation and associated with each medium characterized by the sample index, s, incident frequency, ω, and length of traversal, l, eq. (2-4-4) becomes

$$\phi_p = \phi_\infty(s, \omega, l) B_J(x) . \qquad (2\text{-}4\text{-}5)$$

When the temperature is so low that only a ground doublet is populated, the Brillouin function reduces to tanh(x/2), and under conditions where $H/T << 2k/g\beta$, ϕ_p is a linear function of H/T.

The dependence of ϕ_∞ on s (the sample) at given ω and l requires further specification. The saturation rotation, ϕ_∞, as treated by Shen (50), essentially shows a linear dependence on the magnetic ion concentration N and a functional dependence both on the average index of refraction <n> and the optical frequencies between all possible transition states. The possible transition states take into account the influence of the crystalline field but ignore the presence of the magnetic field. The Zeeman energy here is considered as a perturbation on the crystalline field and its contribution to the rotation is negligibly small. In this regard, if a system consists of several spin species each with effective spin 1/2, eq. (2-4-5) can be given by

$$\phi_p = \phi_\infty \sum_i c_i \tanh(g_i \beta H/2kT) , \qquad (2\text{-}4\text{-}6)$$

where c_i and g_i are respectively the relative spin concentration and g value of the ith spin species with respect to a given field orientation.

3. EXPERIMENTAL SETUPS AND PROCEDURES

3-1. Apparatus and Procedures for Measuring Spin-Bath Relaxation Times

(1) Apparatus

The apparatus is quite similar to that used in the investigation of the magnetic properties of hollow cylindrical superconductors (51) and paramagnetic relaxation of $CaF_2:Ce^{3+}$ initiated by flux jumping (52) by Griffiths. Detailed descriptions of the main features of the apparatus as well as the experimental procedure shall be given in this and following sections.

(i) The Dewar System: The dewar is of a convoluted four wall design as shown in Fig. 6 and is capable of holding about 10 liters of liquid helium in its inner section and approximately the same amount of liquid nitrogen in its outer section. This design avoids the introduction of any nitrogen bubbles into the light path with subsequent degradation of the signal. The dewar has an overall length of 124 cm and an average outer diameter of 20 cm. A superconducting solenoid holding the sample in its geometrical center is attached to a stainless steel connecting tube which in turn is attached to a steel disc with a window cut in its center. The disc houses an O-ring and seals the dewar from the top and in addition supports the solenoid. A small

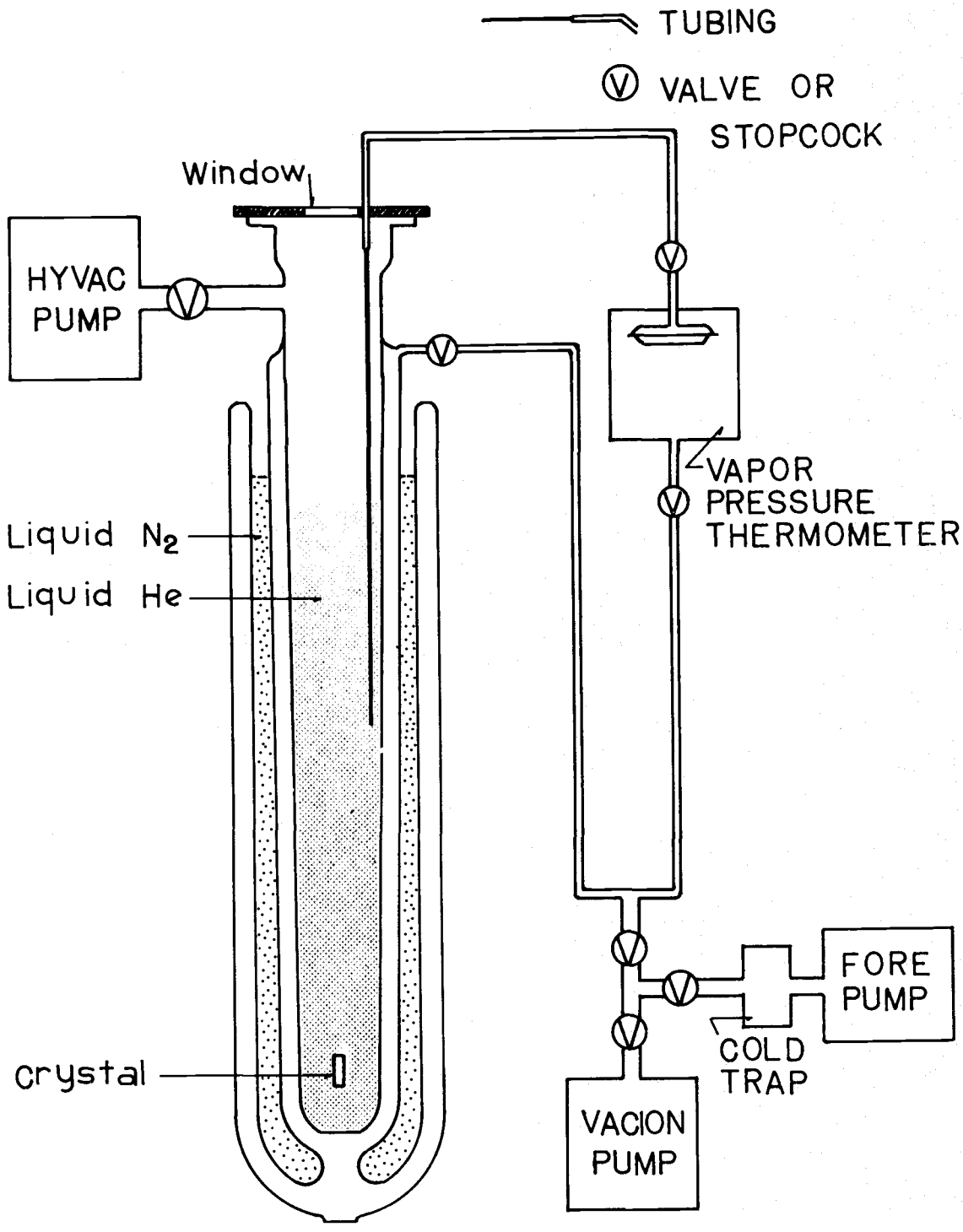

Figure 6. Schematic diagram of the dewar and pumping systems.

vacuum cell was built on the disc in order to avoid frosting which would block off the optical transmission. Electrical connections to the solenoid and the ΔH-coil (both to be described later), helium feed throughs and connection to the vapor pressure thermometer are all on the disc. The foregoing items mentioned with the exception of the dewar itself have been put together into one piece and are referred to as "head and solenoid mount." The details are depicted in Fig. 7, which shows that light is allowed to pass freely along the cylindrical symmetry axis.

(ii) The Pumping System: Figure 6 also shows the pumping system used in conjunction with the dewar system. A Varian (921-0007) vacion pump is employed to bring the pressure of the dewar wall down to a fraction of 10^{-7} torr and to pump a Wallace and Tiernan He^4 vapor pressure sensitive thermometer which measures the temperature of the liquid helium by indicating its vapor pressure. An Edwards ED 500 high vacuum pump is used to pump the helium vapor in the inner dewar and hence control the temperature. Normally it took about 20 min to pump the liquid helium down to the λ-point from $4.2^{\circ}K$. The lowest attainable temperature was about $1.70^{\circ}K$.

(iii) The Field Producing Devices: The dc external magnetic field was produced by a superconducting solenoid (American

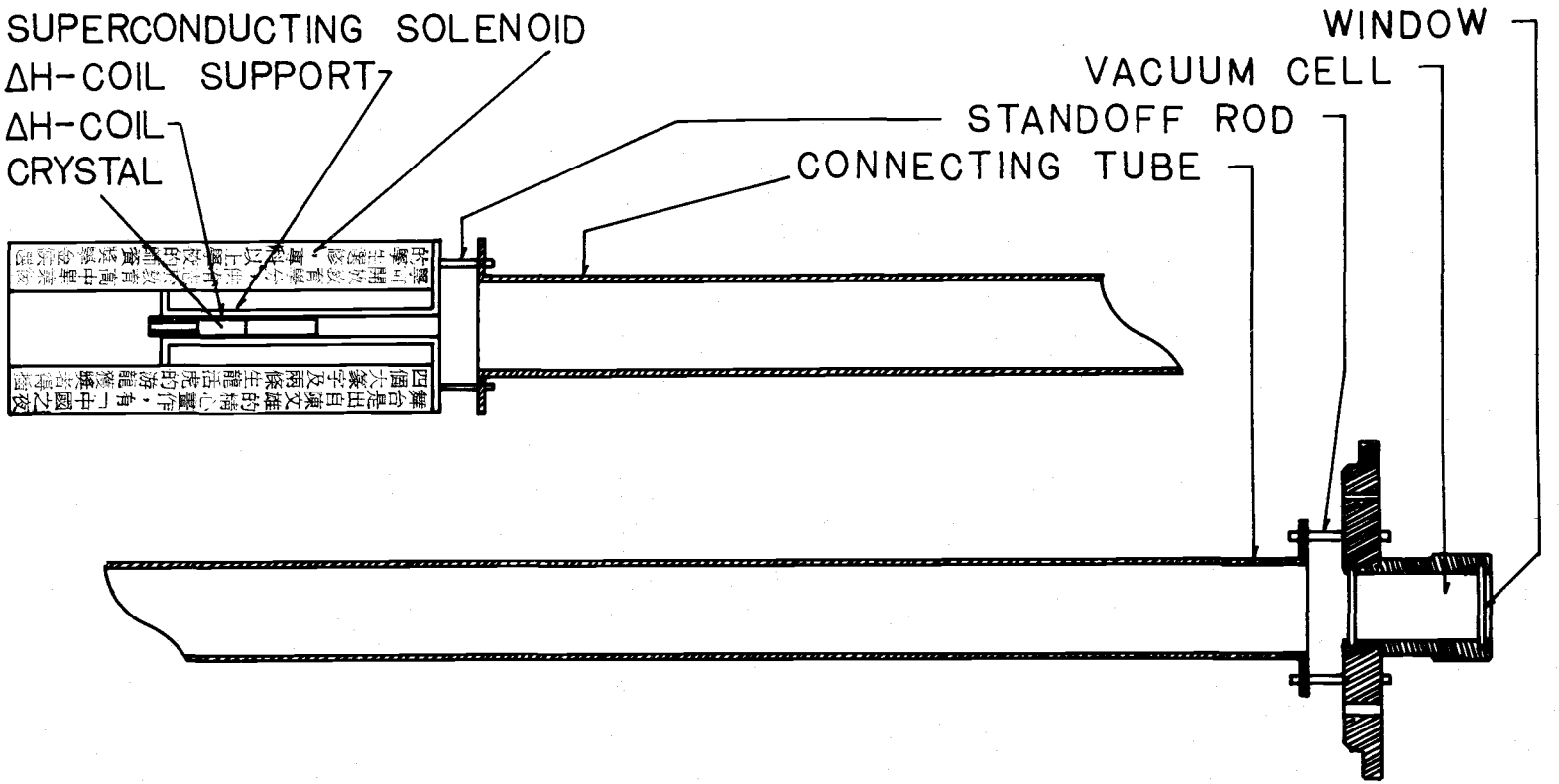

Figure 7. The head and solenoid mount of the dewar.

Magnetics) capable of generating fields up to 56 KOe (an equivalent unit, Kilo-gauss (KG), is also used throughout the text) with a field constant of 971.411 Oe/amp. The physical dimensions and weight are $\pi (1.83)^2$ x 8.75 inch^3 with an 1.55 inch clear bore and 13.75 lb., respectively. The solenoid was energized by a Varian X4101 power supply which can supply regulated current (from 0 to 25 amp) by two selective ramp modes (increase and decrease) in suitable discrete ramp times (5, 10, 25, 50, 100, 250, 500, and 1000 min).

The ΔH-coil (field jumping coil) was made by winding three layers of 0.014" diameter Westinghouse HI-120 superconducting wire, each containing about 178 turns, on a black hollow lucite cylinder of about 1.1 cm outer diameter and 8.0 cm long thus producing a field constant of 95.64 Oe/amp. Under normal operating conditions, it was energized by current of only a few amperes so as to generate a field jump of a few hundred oersteds on top of the static field provided by the main solenoid. The ΔH-coil was coaxially situated in the bore of the main solenoid and the position was so adjusted that the sample was located at the center of both, the ΔH-coil and the main solenoid. This ensures parallelism and uniformity of the fields acting on the sample. The detailed structure of this part is also shown in Fig. 7. For the purpose of rapid switching we built a very simple R-L circuit as indicated in Fig. 8. Six 12 volt batteries were connected in series to provide a 72 volt emf. When switch S4 is closed, the current

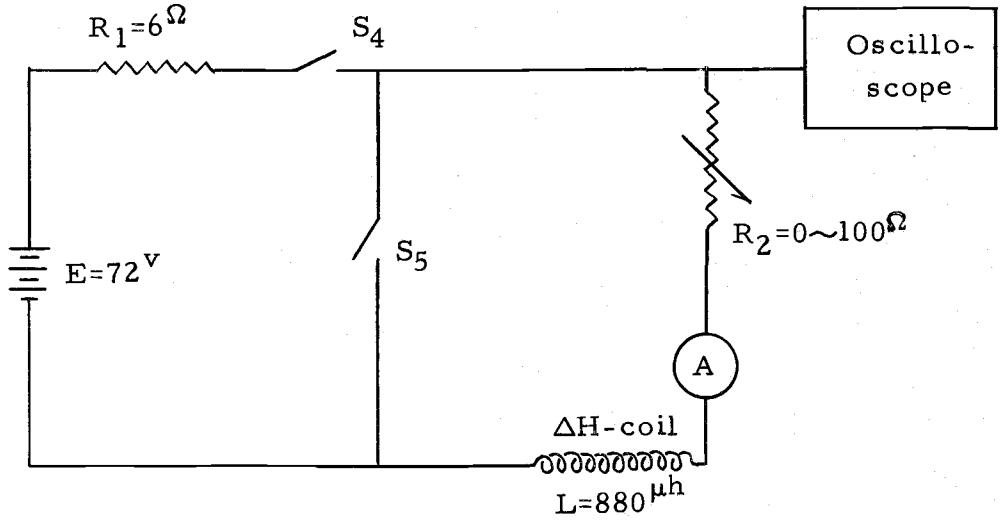

Figure 8. The R-L field switching and triggering circuit.

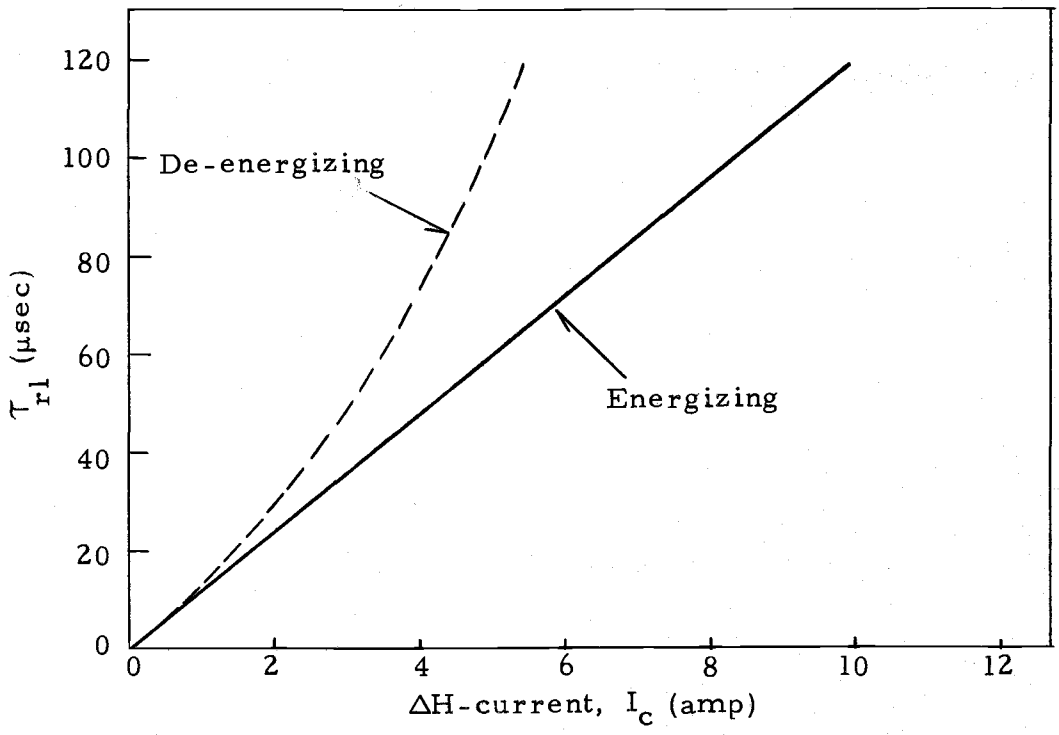

Figure 9. The L/R time constant of ΔH versus ΔH-coil current.

surges through variable resistors R_1 and R_2 and inductor L, thus energizing the ΔH-coil. The current was measured by a Simpson 1701 dc ammeter, the value of which when multiplied by the ΔH-coil field constant gives the ΔH-field. By varying the resistance we were able to switch currents varying from zero to approximately 12 amp corresponding to 1150 Oe. As the resistance decreases the R-L time constant τ_{r1} increases, so that in the large current region (low resistance values) τ_{r1} may become too long to be an effective field switching time. In most of the experimental cases we switched a current of under 8 amp, and, in fact, most of the switching was done at a value of about 3 amp. As indicated in Fig. 8 when S5 is closed, the R_2-L load is shorted and the field in L decays with a longer time constant as shown in Fig. 9. Finally, the voltage across R_2 is taken to trigger the oscilloscope.

(iv) The Optical System: The optical system contains a light source, filters, lenses, prisms, and a polarizer-analyzer combination. A schematic diagram of their arrangement is shown in Fig. 10, which also includes the field producing device just described and the signal detection system to be described later. The light source was an air-cooled Hanovia (901B-11) 200 Watt Hg-Xe arc lamp housed in a Schoeffel Instrument (LH 150) lamphousing and operated by a Schoeffel Instrument (LPS 251) lamp power supply capable of achieving 10 amp maximum output. Light emerges from the lamp by passing through

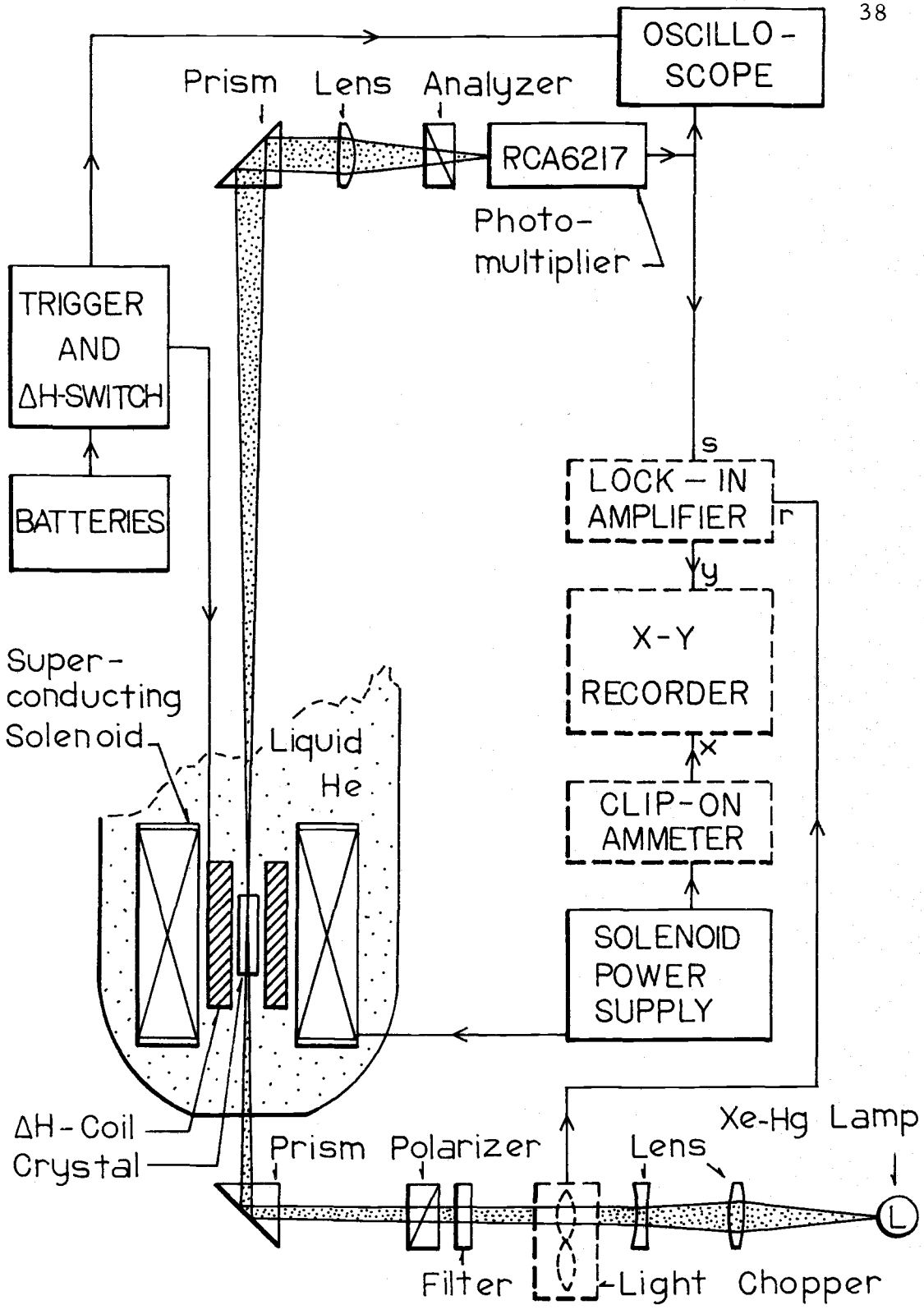

Figure 10. Apparatus arrangement used in the study of spin-phonon-bath relaxation processes employing Faraday effect and field switching technique. The illustration shows both optical and electrical paths.

an Oriel Optics (B-32-40) arc lamp collimator, mounted on the light housing, and is filtered by a suitable Corning Glass C. S. series filter, before being polarized. The transmitted wavelengths of some C. S. series filters are given in the following table.

Table 1. List of Corning C. S. series filters.

C. S. No.	Transmitted wavelengths (Å)		Dimensions W x H x T (inches)
3-110	5780	(yellow)	2 x 2 x 0.25
4-102	5461	(green)	2 x 2 x 0.50
5-74	4358	(blue)	2 x 2 x 0.20
5-62	4047	(purple)	2 x 2 x 0.43
7-83	3654	(indigo)	2 x 2 x 0.25

After being filtered, the nearly monochromatic light is polarized by a 1 cm^2 cross-section Glan-Thompson polarizer, and then undergoes internal reflection with a gimbals-mounted prism, which results in the beam being deflected through 90°. The light is then allowed to traverse the crystal. In order to focus the light beam at this point a divergent lens of focal length f = -1.33 m is placed about 1.5 cm in front of the nozzle of the collimator which is approximately 77 cm distant from the prism face. While transversing the crystal, the light suffers a rotation of its plane of polarization and upon emerging is picked up and again deflected through 90° by a prism atop the dewar. Finally, the light is analyzed by a 1 cm^2 cross-section

analyzer (Karl Lambrecht Crystal Optics) and is focused into an RCA 6217 photomultiplier through a converging lens of focal length f = 20.0 cm. The distance between the prism face and the photomultiplier is about 39 cm. Small distance adjustment is allowed for and must be done before each run in order to obtain the best experimental conditions.

(v) Signal Detection: The signal detection system showing in Fig. 10 mainly consists of a photomultiplier, an oscilloscope, and a X-Y recorder. The change of intensity of the plane polarized light has a cosine squared dependence on the angle of rotation since the rotation is monitored by a polarizer and analyzer pair. It is the photomultiplier that is responsible for converting incident intensity into a voltage signal. The RCA 6217 photomultiplier was powered by twelve 90 volt telegraph batteries connected in series. The anode load was provided by a 10 kΩ resistor across which a 0.001 μf condenser was connected to eliminate high frequency noise. The RC time constant is 10 μsec, and thus for the examination of relaxation times down to the order of 0.1 msec no distortion should be encountered. The voltage across the 10 kΩ resistor was then taken as the output to be fed into either a Hewlett-Packard 7005B X-Y recorder for crystal calibration or a Tektronix 547 oscilloscope for spin-bath relaxation time measurement. If the X-Y recorder was employed,

we normally sent the signal to the signal channel of a Princeton Applied Research 120 lock-in amplifier for better results, the output of which was in turn sent to the y-axis of the recorder. The x-axis was driven by a voltage signal provided either by a Hewlett-Packard 428B clip-on ammeter or by the Varian superconducting solenoid power supply. The signals of both were proportional to the energizing current to the main solenoid generated by the power supply. The reference channel of the lock-in amplifier was connected to a Princeton Applied Research 125 light chopper operating at 667 Hz, which generates an ac signal and at the same time provides the reference signal for the amplifier. The oscilloscope is equipped with a type 1A1 dual-trace plug-in unit so that it can be used to display both traces of relaxation (photomultiplier output) and ΔH rise simultaneously when triggered. The traces were photographed by a Hewlett-Packard 196B oscilloscope camera using polaroid 47 (3000 ASA equivalent) film.

(vi) The Samples: The crystals were provided and cut by Optovac Inc., North Brookfield, Mass. 01535. Their impurity concentration, size (roughly 3/8 in. dia. x 1 in. cylinder), and cut can be compared from Table 2. Since we will encounter each of the samples so many times throughout the text, we will, from here on, call them only by their impurity concentration (Ce^{3+} at. %) and

Table 2. List of the Ce^{3+}:CaF_2 crystals used as samples.

Ce^{3+} Impurity Concentration (%)	Orientation of Cylindrical Axis	Physical Dimensions diameter (mm) x	length (mm)
3	[100]	9.7	26.7
1	[100]	9.6	25.7
1	[111]	9.5	26.5
0.5	[100]	9.7	28.1
0.5	[111]	9.8	27.8

crystallographic orientation. For example, the 3%, H // [100] crystal will refer to the one containing 3% Ce^{3+} with its cylindrical axis cut parallel to the crystal [100] direction along which the H field is applied.

(2) Procedure

(i) Preparation: Successful data collection depends critically on the following steps. Therefore, they must be done before each run is scheduled.

a) The head and solenoid mount of the dewar is first removed from its position for mounting the crystal, the ΔH-coil, as well as the solenoid itself, and for connecting all the electronic leads. At the same time the inner dewar is cleaned. After these things have been done, the whole section is put back into the dewar. Plugs on

the head then relay the connections to the electronic instruments outside the dewar. The liquid and gaseous helium transfer pipe and tubing are mounted afterward. Coarse inspection of the sealing of the dewar system then is done. This is accomplished by pumping the system down until the vapor pressure sensitive thermometer indicates a temperature of less than $1^{\circ}K$ (pressure less than 10 microns) and then checking the needle. If the needle of the thermometer indicates no significant rise of temperature during a period of a few hours or so, the dewar can be considered to be well sealed. Otherwise leak detection must be done and the necessary corrections made.

b) Detection of the signal depends on proper alignment of the optics. While the alignment must be done ahead of each run, small adjustments, however, may be needed during the run. Prisms and lenses play the most crucial roles in this stage, especially the gimbals-mounted prism. Often tremendous care and patience have to be taken in aligning these particular optical elements.

c) The walls of the dewar must be pumped down to at least 10^{-7} torr in order for it to serve as a good liquid nitrogen and helium vessel. Meanwhile the vapor pressure gauge is also pumped to the proper pressure (1 micron or less).

d) Sufficient time is allowed to warm up the electronic

instruments. Some of them require calibration and this must be done before data taking.

e) The inner dewar must be precooled by filling it to a depth of several inches with liquid nitrogen and allowing it to boil off over night. Next day (the day a run is scheduled) the inner dewar is flushed by dry helium through a "pump-out and fill" procedure which is repeated about five times. The liquid transfer starts soon after the inner dewar is well flushed. It normally takes one and one-half to two hours to make a complete transfer. The amount of liquid helium used is about 20 liters, since about half of that is used to bring down the temperature of the system from slightly higher than liquid nitrogen temperature to liquid helium temperature. After transferring, the end of the transfer tube is sealed and the helium vapor pressure is reduced by pumping. The λ-point is reached after approximately 20 min of pumping below which temperature the liquid becomes a superfluid with so great a thermal conductivity that no boiling takes place in the bulk of the liquid, thus eliminating any major disturbances to the light beam.

(ii) Calibration of the Crystal and the ΔH-Coil

a) Calibration of the crystal was done with the aid of the X-Y recorder. The x-axis of the plot represents the solenoid current (or magnetic field) and the y-axis indicates the cosine squared function of

the paramagnetic Faraday rotation. The resultant curve is then converted into one of rotation versus H/T such as Figs. 21-23 displayed in §4-2. This piece of information is necessary for the ΔH-coil calibration and for the correct analyzer setting to be described later. The same procedure was repeated for all samples and wavelengths available at known temperatures.

b) Calibration of the ΔH-coil was also done by the aid of a $\cos^2\theta$ versus H/T plot on the X-Y recorder. We initially let the recorder pen reside at a point "i" on the curve corresponding to field H_i as indicated in Fig. 11, then switched a known current I_c to energize the ΔH-coil so that the pen moved to a point "f" off the curve. We then project "f" on to the curve at the point "f' " corresponding to a field H_f. The change in field $\Delta H = H_f - H_i$ was, of course, caused by the ΔH-coil current I_c. The field constant of the ΔH-coil is equal to $\Delta H/I_c$ with the polarity in this case being antiparallel to that of the steady dc field. This procedure was repeated for different I_c's and the ΔH-coil field constant was taken from the slope of the ΔH versus I_c curve so generated.

(iii) Measurement of Spin-Bath Relaxation Times: Field dependent data of relaxation times were collected by switching to different H_f's to disturb the spin populations at known temperature and observing the subsequent relaxation traces. When these traces were

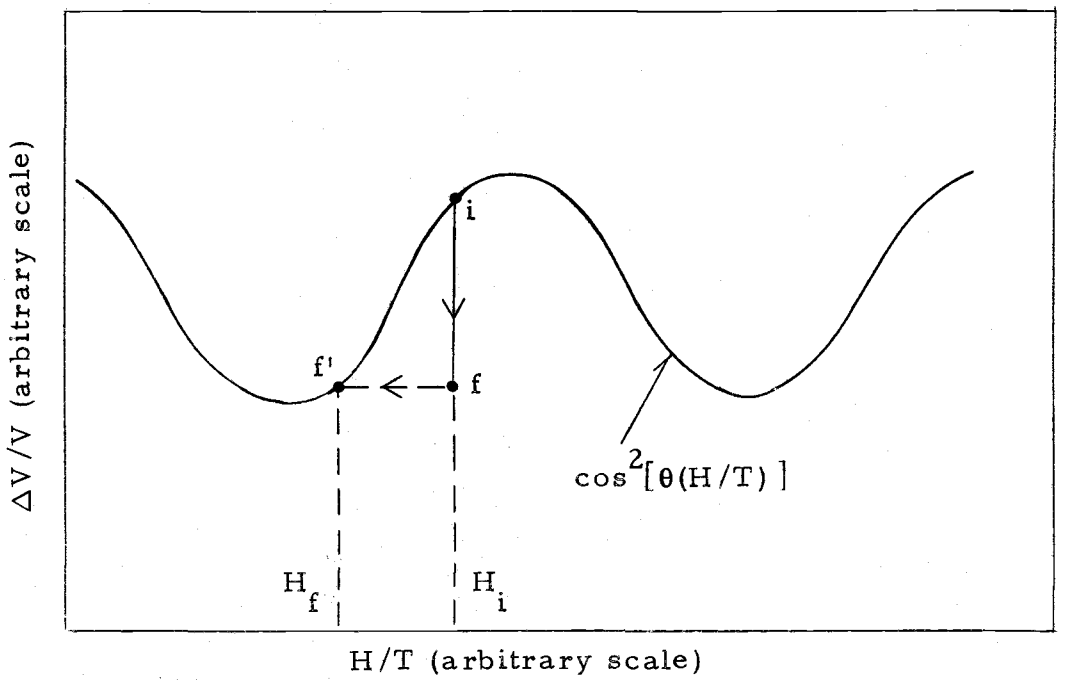

Figure 11. $\cos^2\theta$ Curve used in calibration of ΔH-coil.

displayed on the oscilloscope screen, the y-axis depicted the output signal of the photomultiplier which is proportional to the cosine squared of the Malus angle, $\theta = \phi - \phi_a$, where ϕ and ϕ_a are respectively the Faraday rotation and the angle of the transmission plane of the analyzer, i.e., the analyzer setting, both measured from the plane of the polarizer. The x-axis was the time base. Suppose a trace was seen to relax from V_i to V_f, where V's are the signal heights, the instantaneous signal V(t) can be described by

$$V(t) = V_0 \cos^2 \theta(t) = V_0 \cos^2 [\phi(t) - \phi_a] \qquad (3\text{-}2\text{-}1)$$

with the initial and final conditions satisfying $V(0) = V_i = V_0 \cos^2 \theta_i$ and $V(\infty) = V_f = V_0 \cos^2 \theta_f$, respectively. Since $\phi(t)$ is proportional to n(t), the instantaneous spin population difference, the trace indirectly provides the information of $n = n(t)$ through eq. (3-2-1), i.e., $\phi(t) = \cos^{-1} \sqrt{V(t)/V_0} + \phi_a$. If fortunately the dependence of n on t is exponential, the decay time can be drawn from the slope of the semi-logarithmic plot of n (or it is the same, ϕ) versus t. The time constant so obtained will be interpreted as the relaxation time associated with the final field value, $H_f = H_i + \Delta H$. In the case where n(t) consists of several exponential decays of very different time constants, there is still hope of resolving that one having the longest relaxation time. The relaxation initiated in this fashion may proceed from an initial condition of complete saturation ($H_i = 0$), partial saturation

($H_i > 0$ and $\Delta H > 0$) or negative saturation ($H_i > 0$ and $\Delta H < 0$). To analyze a trace from the oscilloscope screen we always need to know the temperature, the time base, the value of I_s used to produce H_i, and the coil current I_c used to initiate ΔH. The relaxation time, τ, so acquired from the photograph taken, then merely provides a single point on the curve of a τ versus H plot. In order to cover a wide range of magnetic field we have to repeat the same procedure of picture taking and analyzing at each selected value of H at a fixed temperature.

To obtain the plot of n(t) or $\phi(t)$ versus t from the foregoing description of functional conversion for each trace taken would be a formidable job since we had so many pictures to be done. An alternative method which simplifies the analyzing yet yields no significant distortion was taken. The method used approximates eq. (3-2-1) by $V(t) = -V_0[\phi(t) - \phi_a - \pi/4 - 0.5]$, where ϕ's are to be measured in radians. This enabled us to analyze n(t) or $\phi(t)$ directly from V(t), i.e., the trace itself, without committing any functional conversion first. We shall show that under certain circumstances such an approximation is justified. Suppose we can manage to arrange the ΔH-field together with the analyzer setting ϕ_a such that while the field switching causes the additional rotation $\Delta\phi = \phi_f - \phi_i \simeq 30^\circ$ the condition $(\phi_f + \phi_i)/2 - \phi_a = 45^\circ$ is also fulfilled. These then require $\theta_i = \phi_i - \phi_a \simeq 30^\circ$ and $\theta_f = \phi_f - \phi_a \simeq 60^\circ$ as calculated from the initial

and final conditions of eq. (3-2-1). Bearing this in mind we proceed to examine the straight line whose slope is given by the tangent to the cosine square curve at $\theta = 45^{\circ}$ as shown in Fig. 12. This straight line is seen to be in excellent agreement with the curve defined in the angular range $\theta \epsilon (30^{\circ}, 60^{\circ})$ and thus can be taken to approximate the cosine squared curve, regardless of the actual functional form of $\theta(t)$ without causing any serious error. A concrete example is shown in Fig. 13 by taking $\theta(t) = 60^{\circ} - 30^{\circ} \cdot \exp(-t/\tau)$. The exact normalized trace obeys $V(t)/V_0 = \cos^2 [60^{\circ} - 30^{\circ} \cdot \exp(-t/\tau)]$ which relaxes from $V(0)/V_0 = \cos^2 30^{\circ} = 0.75$ to $V(\infty)/V_0 = \cos^2 60^{\circ} = 0.25$ nearly exponentially. Its linearlized form $V(t)/V_0 = 0.2382 + 0.5236 \cdot \exp(-t/\tau)$, obtained from the line equation $V(t) = -V_0 [\phi(t) - \phi_a - \pi/4 - 0.5]$, decays from $V(0)/V_0 = 0.7618$ to $V(\infty)/V_0 = 0.2382$ exponentially with the time constant τ and is to be compared with the exact trace. The difference in the traces is about 4.7% at the extremes and is about of the same order as the attendant noise imposed on the signal. Such a linearization can be achieved without any difficulties since ΔH and ϕ_a are fully experimentally controllable and ϕ_i can be obtained from a ϕ versus H/T curve as given in the next chapter.

3-2. The Electron Paramagnetic Resonance Spectrometer

The apparatus employed to obtain the EPR spectra consisted of a helium dewar and a standard Varian E-9 EPR spectrometer with a

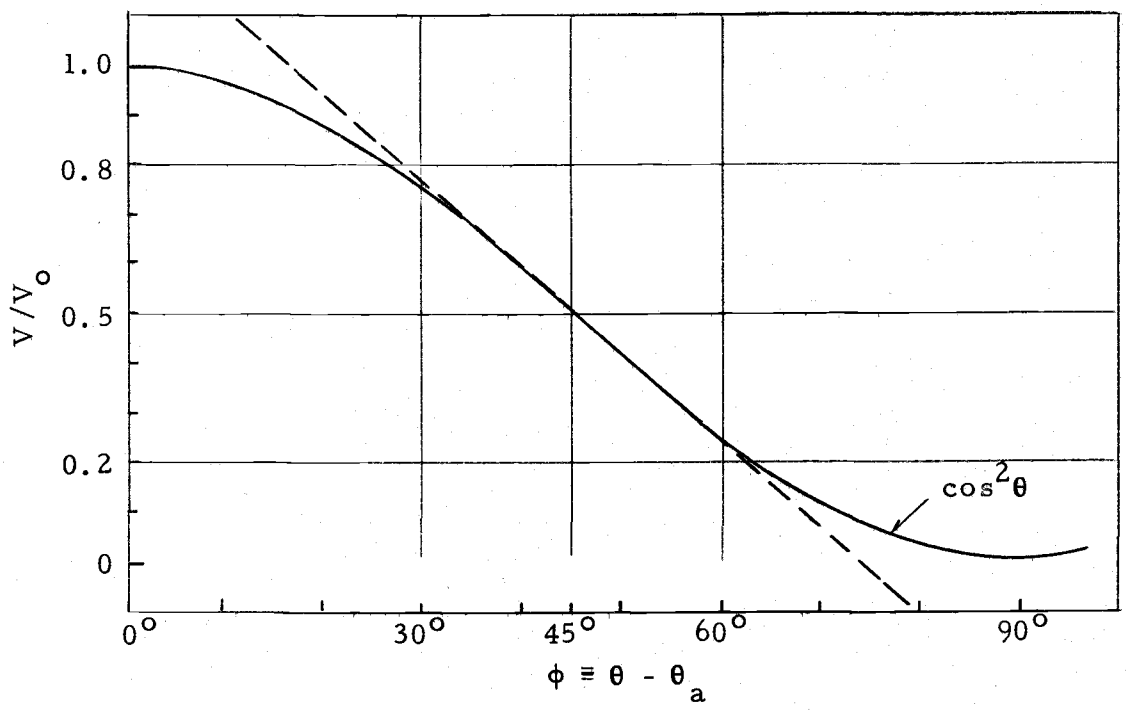

Figure 12. Diagram to show that the segment of arc of a cosine squared curve around $\theta=45^{\circ}$ can be approximated by its tangent at $\theta=45^{\circ}$.

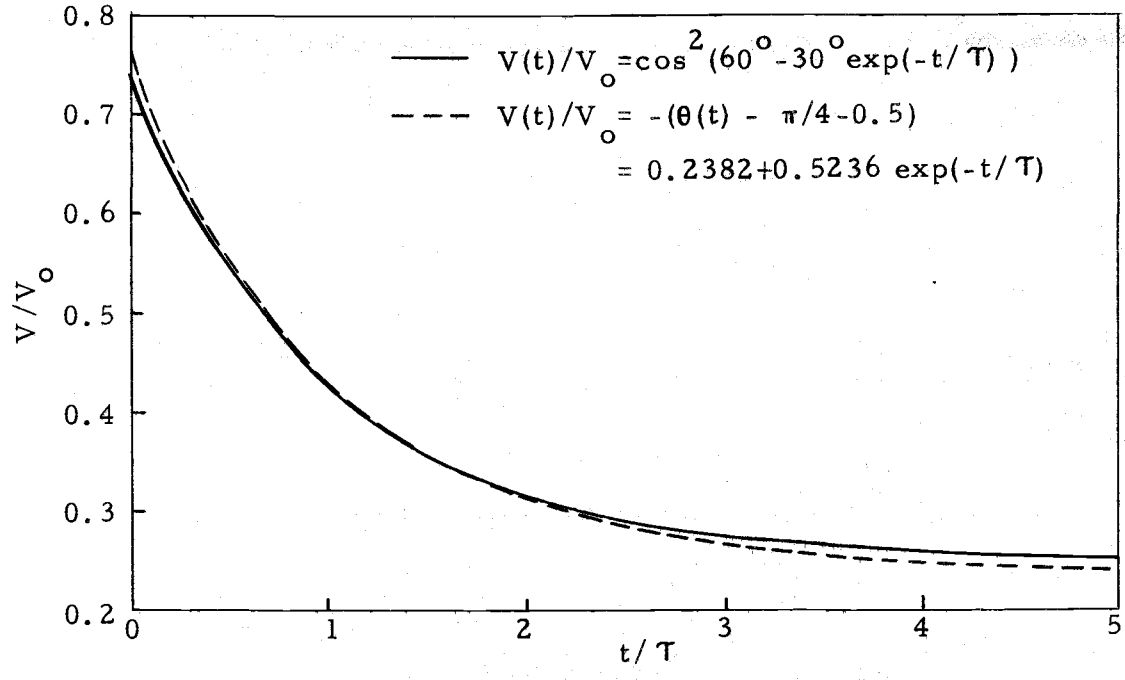

Figure 13. Plot of $V(t)/V_o=\cos^2\theta(t)$ and $V(t)/V_o = -(\theta(t) - \pi/4-0.5)$ versus t/T to show the close fit of the two curves.

modified resonance cavity and low frequency modulation coils. The resonance cavity consists of a simple wave guide section with a silver-plated end piece (iris) and with a teflon rod for impedance matching as described by Gordon (53). The cavity was operated in the TE_{102} mode, and the sample in it is located at the narrow side about 1/4 of the total cavity length from the reflection end so that the microwave H field is always perpendicular to the external magnetic field. The modulation coils were mounted outside of the helium dewar producing an ac modulation field parallel to the external field. The spectrometer itself consists of the following basic elements:

(1) E-101 Microwave Bridge: The bridge contains a microwave circuit (frequency range: $8.8 \sim 9.6$ GHz), a Klystron power supply, a preamplifier and automatic frequency control and serves the function of detecting the EPR signal reflected from the sample cavity.

(2) E-3425 Electromagnet with a power supply, a cooling system, and a control unit (E-203) whose 9 in. diameter poles provide a uniform (10^{-4} gauss/cm^3) variable ($0 \sim$ 9KG) field for experimental use. The bottom tip of the helium dewar containing the cavity is centered in this magnet gap.

(3) E-204 Low Frequency Modulation Unit: The unit contains a transmitter and a receiver. The former drives the cavity signal from the detector crystal and preamplifier in the bridge and converts

it to a dc voltage for the recorder Y-axis.

(4) E-80A Recorder: The recorder displays the EPR spectrum as a function of time. The recording time may be selected in increments from 30 secs to 16 hrs.

The experimental procedure was routine. The sample was first mounted in the cavity. The cavity was then recoupled to the wave guide. After inserting the guide and cavity into the dewar and connecting the guide to the microwave bridge, liquid N_2 was poured into the outer dewar with the inner dewar being precooled by helium exchange gas. Then liquid helium was transferred. It normally took 2-3 liters (dewar capacity 1 liter) of helium. Operation of E-9 spectrometer system included system turn on, bridge tuning, modulation frequency selection, field control and recorder settings on the console, and spectra taking. For the field alignment and the change of field orientation, the sample can be rotated about a horizontal axis from outside of the dewar for about $\pm 45^{\circ}$ from vertical. The external field, together with the modulation field, was rotatable $\pm 95^{\circ}$ about a vertical axis.

4. EXPERIMENTAL RESULTS

4-1. EPR Spectra

EPR spectra reveal information on crystal site symmetry which is essential to the calculation of spin-lattice relaxation times and spin specific heats, and hence are essential in our analysis of experimental data. In this section we present six spectra of Ce^{3+}:CaF_2, having different Ce^{3+} concentrations and crystallographic orientations, taken at sample temperatures of approximately $1.4^{\circ}K$.

Figure 14 shows the spectrum of the 1% crystal with H// [100] taken at a frequency of $\nu_0 = 9.345$ GHz. The spectrum consists of two intense resonances, corresponding to $g_{\parallel} = 3.07$ and $g_{\perp} = 1.39$ due to the tetragonal site symmetry. The presence of two g values arises from the fact that the axial direction of the tetragonal distortion occurs along a cube edge. Therefore, for the case of the external magnetic field being applied along a [100] direction one-third of the tetragonal sites will find their axial direction parallel to that of the field while two-thirds will have their axial direction located in the plane perpendicular to H. Weak additional resonances also showed up at fields around 2.70, 3.30, and 5.64 KG, respectively. The structure centered at $H \simeq 3.30$ KG ($g \simeq 2.02$) may be associated with some complexing involving sites of cubic symmetry ($g = 2.00$) or minor

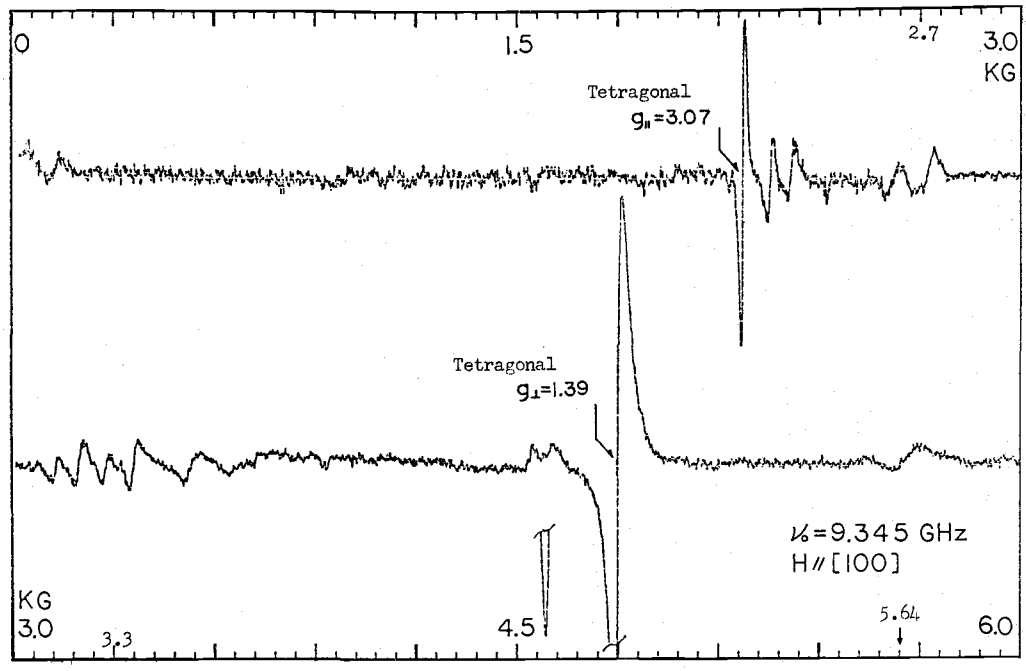

Figure 14. EPR spectrum of 1% Ce^{3+}:CaF_2, H//[100].

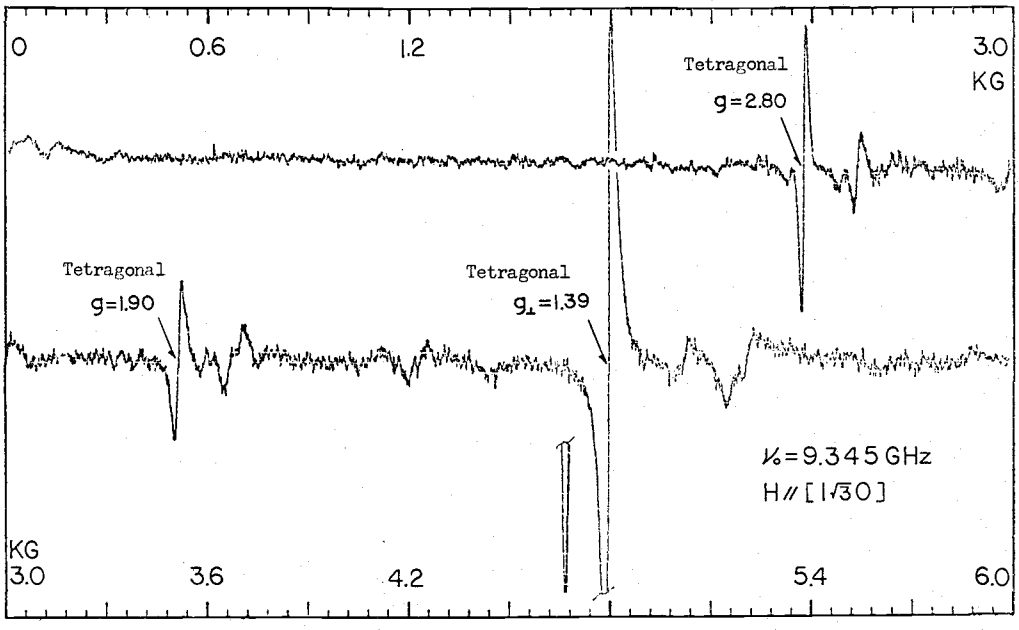

Figure 15. EPR spectrum of 1% Ce^{3+}:CaF_2, H//[1 $\sqrt{3}$ 0].

contamination from DPPH tracer or 3-d ions (most likely in the cavity) and the other two structures are probably caused by the presence of sites of lower symmetries in the crystal. The results of the spectrum are comparable to those reported by other authors (11, 31). Figure 15 is the same spectrum except with H // [1 $\sqrt{3}$0] and was taken to confirm the identification of the tetragonal sites by following the changes in g for the three non-equivalent sites of tetragonal variety. Three main resonances, g = 1.39, 1.90, and 2.80, of the tetragonal site symmetry were present together with weak additional resonances. The calculated g values using $g_{\perp}$ = 1.396 and $g_{\parallel}$ = 3.038 (11) are 1.40, 1.94, and 2.74.

Figure 16 shows the spectrum of the 1% crystal with H// [111] and ν_0 = 9.317 GHz. Calculation based on the previous g values (11) predicts one resonance of g = 2.09 (H = 3.138 KG) for the tetragonal site symmetry. The spectrum indicated three intense resonances, corresponding to g = 2.09, 2.11, and 2.13, arising from imperfect field alignment along the crystal [111] axis. In spite of the appearance of weak additional resonances, the spectrum indicated the strong domination of the tetragonal sites. It is interesting to point out that the resonance occurring at H = 2.77 KG ($g_{\parallel}$ = 2.40) can be associated with the trigonal site symmetry with the field along its C_3 axis and that occurring near H = 5.64 KG as seen in the 1%, H// [100] case also appeared here. The dc drift of the recorder level appearing in

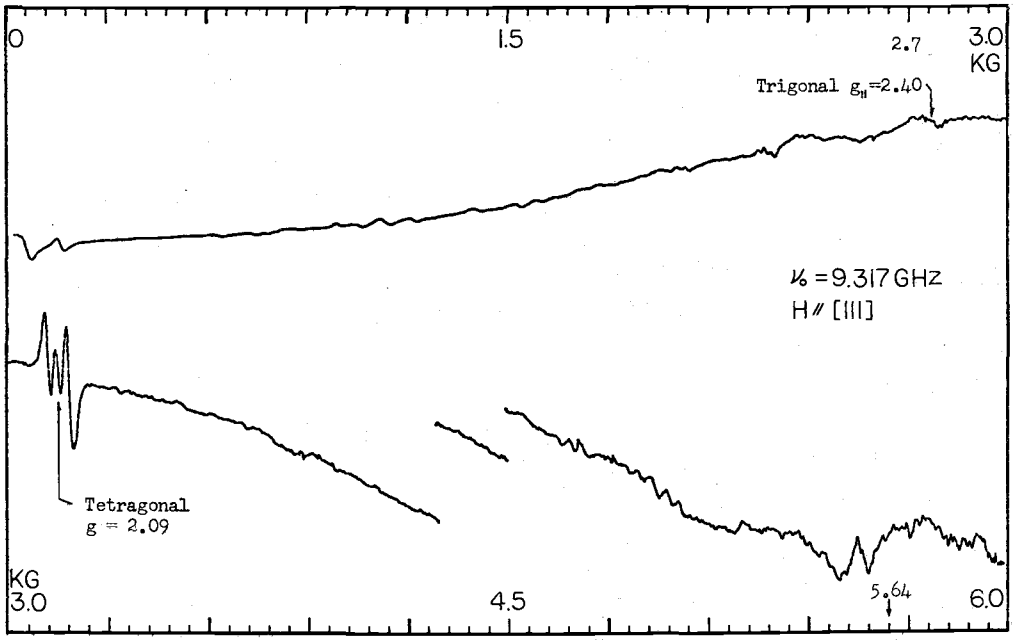

Figure 16. EPR spectrum of 1%, Ce^{3+}:CaF_2, H//[111].

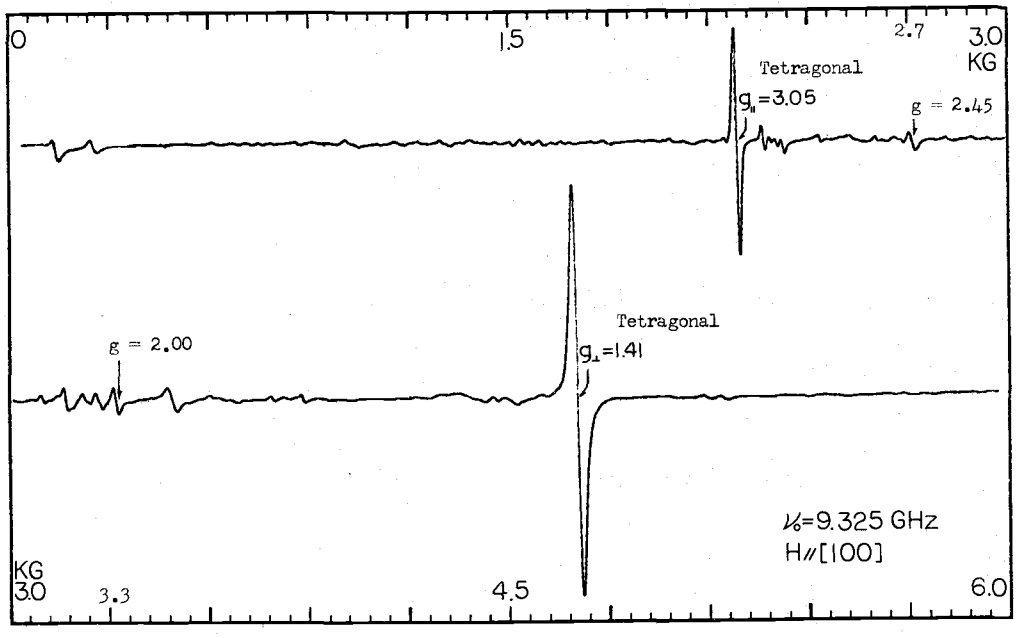

Figure 17. EPR spectrum of 0.5 Ce^{3+}:CaF_2, H// [100].

the spectrum is due to a temporary mismatch of the reference and signal phase in the lock-in amplifier.

Figure 17 gives the result of 0.5% crystal with H// [100] and ν_0 = 9.325 GHz. The spectrum shows almost the same resonances when compared with its 1% counterpart. The effect of lower impurity concentration smears out the weak resonance near H = 5.64 KG and renders a weaker resonance intensity and hence a clearer spectrum. The two major resonances equivalent to $g_{||}$ = 3.05 and $g_{\perp}$ = 1.40 are of course due to the tetragonal site symmetry. Other weak resonances are probably caused by the same reasons as stated in the case of the 1% crystal.

The spectrum of the 0.5% crystal with H// [111] and ν_0 = 9.317 GHz appears in Fig. 18 exhibiting three close intense resonances corresponding to g = 2.00, 2.07, and 2.10. The first resonance was contributed by the DPPH tracer used for microwave tuning and field calibration, which was not used in the other cases. The rest of the resonances could be ascribed to the imperfect alignment of the field along the crystal [111] axis in a tetragonal site symmetry. A perfectly oriented field was expected to yield g = 2.09 as stated in the description of Fig. 16. When compared to its 1% counterpart (Fig. 16) we see the structure occurring near H = 5.64 KG was not present in this case but the contribution from the trigonal site symmetry ($g_{||}$ = 2.40) still showed up and the spectrum possessed an overall

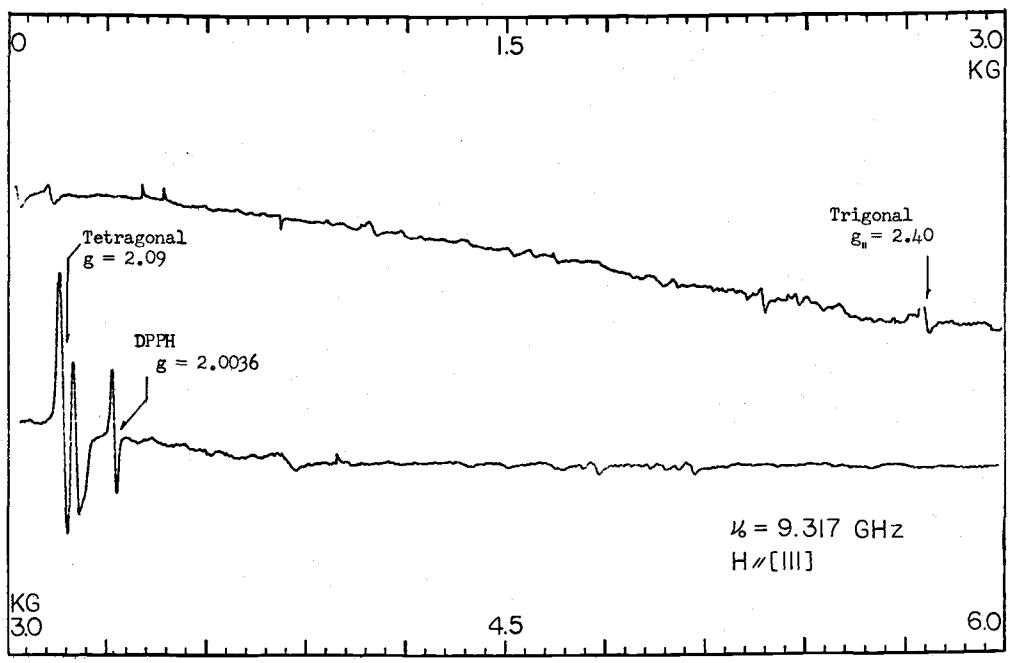

Figure 18. EPR spectrum of 0.5% Ce^{3+}:CaF_2, H // [111].

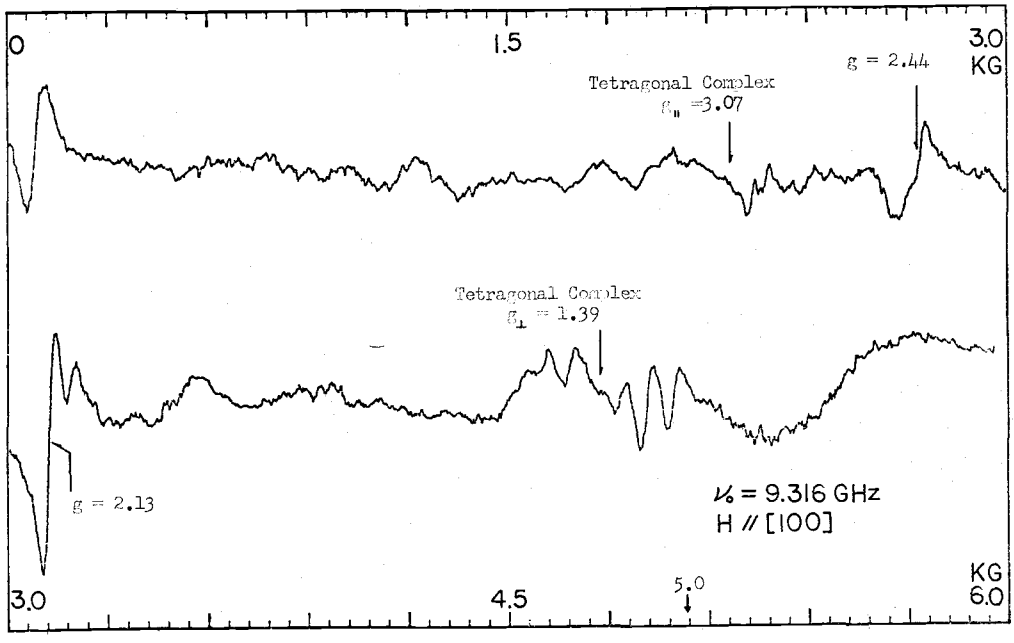

Figure 19. EPR spectrum of 3% Ce^{3+}:CaF_2, H // [100].

weaker resonance intensity. It should be noted that the trigonal contribution when H is applied along [100] axis yields g = 1.39 and hence is overshadowed by the strong resonance of $g_{\perp}$ = 1.39 arising from the tetragonal site symmetry. Therefore the H//[111] case renders an excellent opportunity of observing the existence of the trigonal sites, although the spectrum indicates its contribution is negligible.

The spectrum of the 3% crystal with H//[100] and ν_0 = 9.316 GHz is given in Fig. 19. The resonance of g = 2.13 (H = 3.12 KG) was the most intense one but was not identifiable with any crystal site symmetry higher than trigonal. The structures around $g_{\parallel}$ = 3.07 (H = 2.17 KG) and $g_{\perp}$ = 1.39 (H = 4.79 KG) apparently can be associated with the complexing of the tetragonal site symmetry. The resonance occurring at g = 2.44 (H = 2.73 KG) is seen enhanced in this case as compared to its lower impurity concentration counterparts. The high field structure is seen not only enhanced but also broadened. The resonance band covers fields from H$\simeq$ 5.0 to 6.2 KG as seen from other runs with a higher range setting. The overall anomaly of this spectrum indicates that the system has entirely different paramagnetic nature from the 1% and 0.5% systems, i.e., the spectrum is not merely respectively three and six times the resonance intensity of the 1% and 0.5% cases but must be ascribed to the presence of lower site symmetries and stronger ion-ion interactions due to higher concentration.

The minor resonances in each case, though unidentified, can not serve the purpose for cross-relaxation since their lines are in general too far removed from our lines of interests. Also their Faraday rotation will be small itself due to low concentration if they are rare-earth ions and almost zero due to the orbital angular momentum quenching if they are 3-d ions.

4-2. Rotatory Dispersion and Faraday Rotation of $Ce^{3+}:CaF_2$

The paramagnetic Faraday rotation per unit length of $Ce^{3+}:CaF_2$ in various Ce^{3+} concentrations and magnetic field orientations was measured at different wavelengths in the visible range. The dispersion curves are shown in Fig. 20. It is seen that greater rotation occurs at the shorter wavelengths and that the amount of rotation is roughly proportional to the Ce^{3+} concentration. In order to acquire the greatest sensitivity available we picked 3654 Å as our working wavelength through the entire experiment. The low-energy side of the nearest absorption band (30) associated with the J = 5/2 multiplet at liquid helium temperatures starts at approximately 3250 Å which is 3402 cm^{-1} away from 3654 Å. Therefore, there should be no problem of disturbing the spin populations of the ground states of J = 5/2 in the 4f term. In other words, at this frequency, the paramagnetic Faraday rotation should be still proportional to the magnetization of

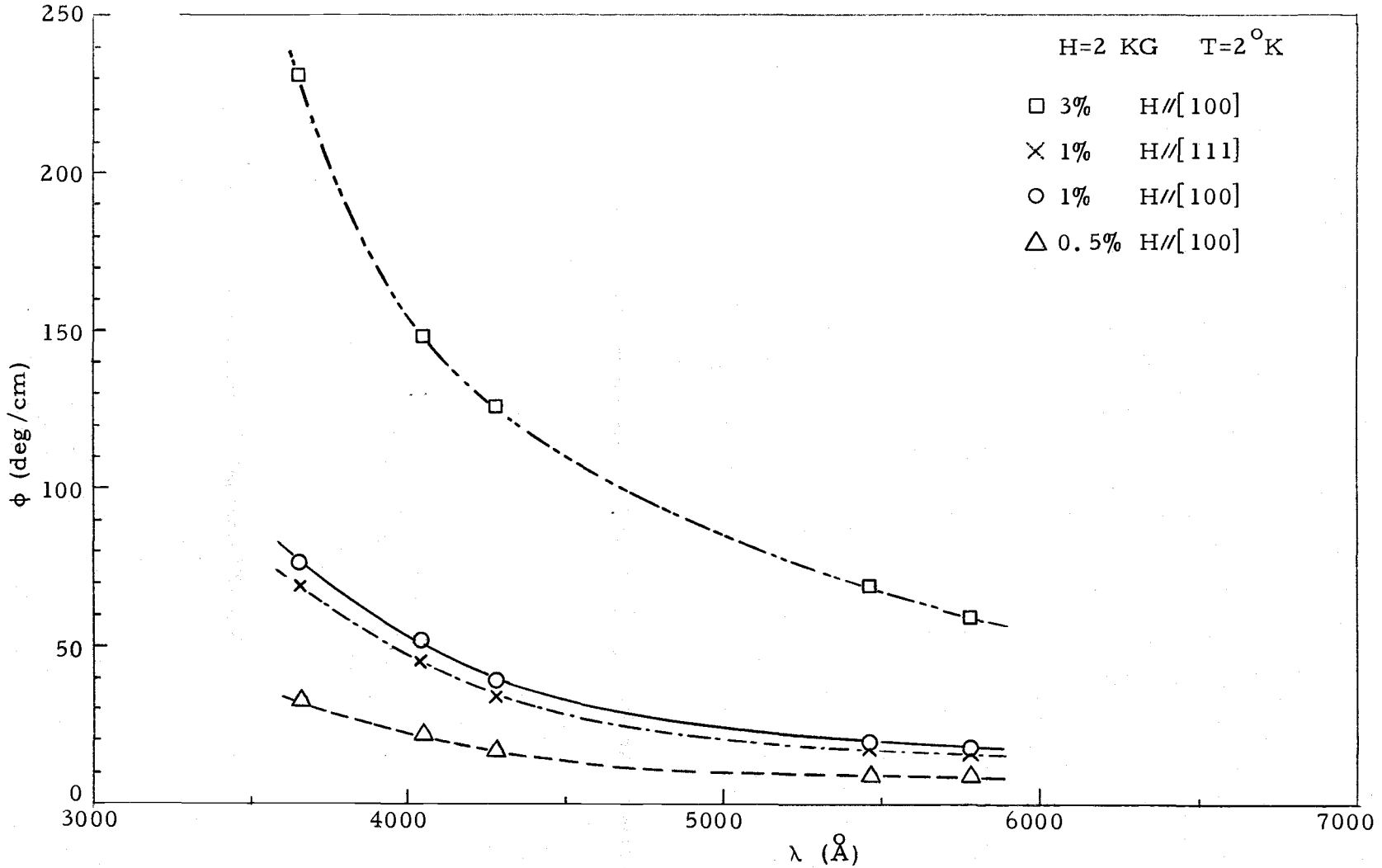

Figure 20. Rotatory dispersion curves of x% Ce^{3+} : CaF_2.

the system. We shall see this in Figs. 21 and 22.

Figure 21 gives the results of rotation measurements on the 1% crystal with H//[100] and H//[111]. In the former case, the spin system consists of two Zeeman species, namely $g_{\perp} = 1.396$ and $g_{\parallel} = 3.038$ with the former weighted twice as much as the latter. Theoretically the rotation is to be expressed by addition of two Brillouin functions (eq. (2-4-6)):

$$\phi = \phi_{\infty}^{a} [(2/3)\tanh(g_{\perp}\beta H/2kT) + (1/3)\tanh(g_{\parallel}\beta H/2kT)] . \quad (4-2-1)$$

Again, here and below ϕ_{∞}^{i} is to stand for the saturation rotation per cm of the system. Since our maximum field attainable was far below the saturation value, ϕ_{∞}^{a} cannot be determined accurately. Nevertheless, a representative value can be given by $\phi_{\infty}^{a} = 1110^{o}$. Points calculated with this value are shown at H/T = 5, 8, and 10 KG/^{o}K in Fig. 21 with "x" signs. In the H//[111] case, the spin system is of a sole species with g = 2.092. The rotation is expressible by

$$\phi = \phi_{\infty}^{b} \tanh(g\beta H/2kT) , \quad (4-2-2)$$

where ϕ_{∞}^{b} takes the value 940^{o} and points calculated from it are shown with "•" signs in the same figure at the same H/T values.

The results of rotation measurements on the 3% Ce^{3+}:CaF_2 with H//[100] appear in Fig. 23 while Fig. 22 gives those on the 0.5% crystals for both field orientations. Testing points resulting from respectively

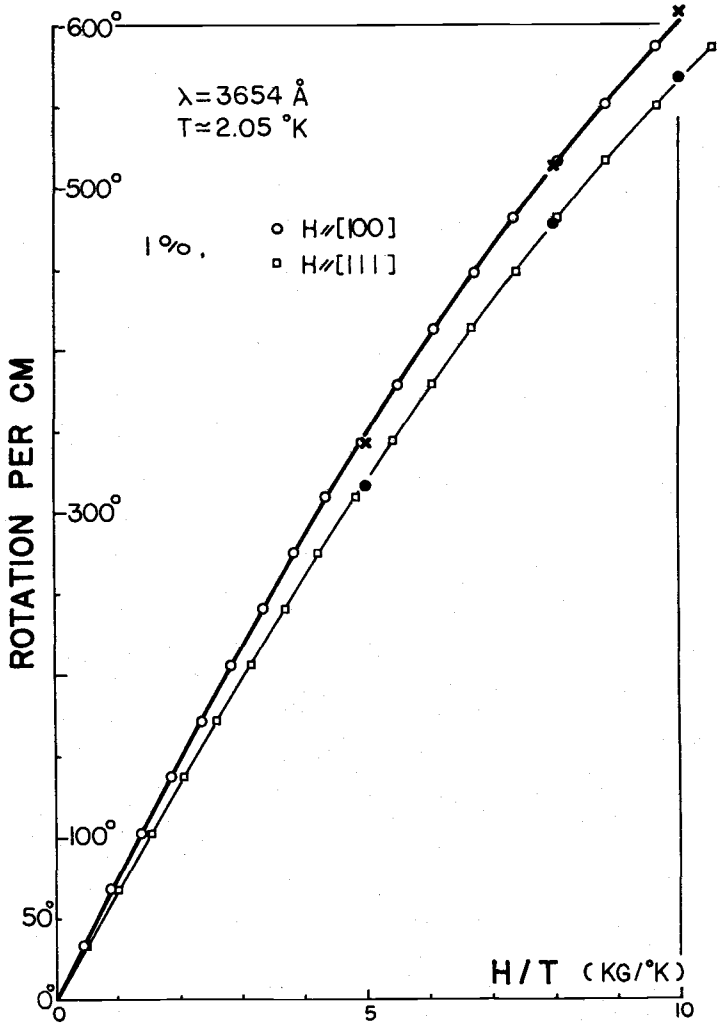

Figure 21. Rotation versus H/T for 1%, H//[100] and H//[111] crystals.

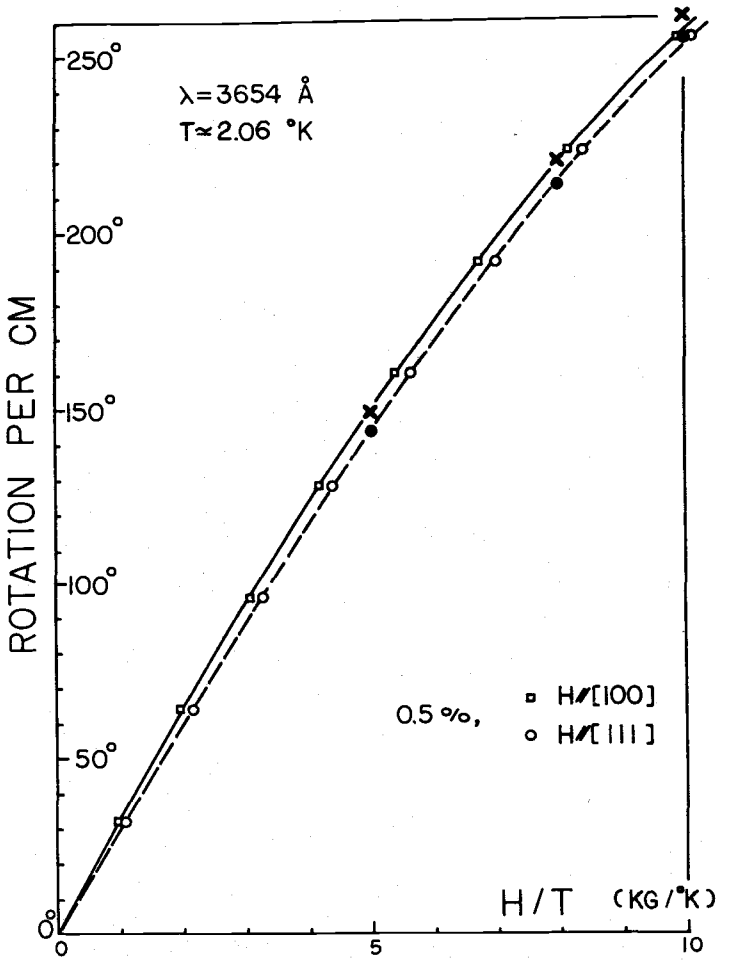

Figure 22. Rotation versus H/T for 0.5%, H // [100] and H// [111] crystals.

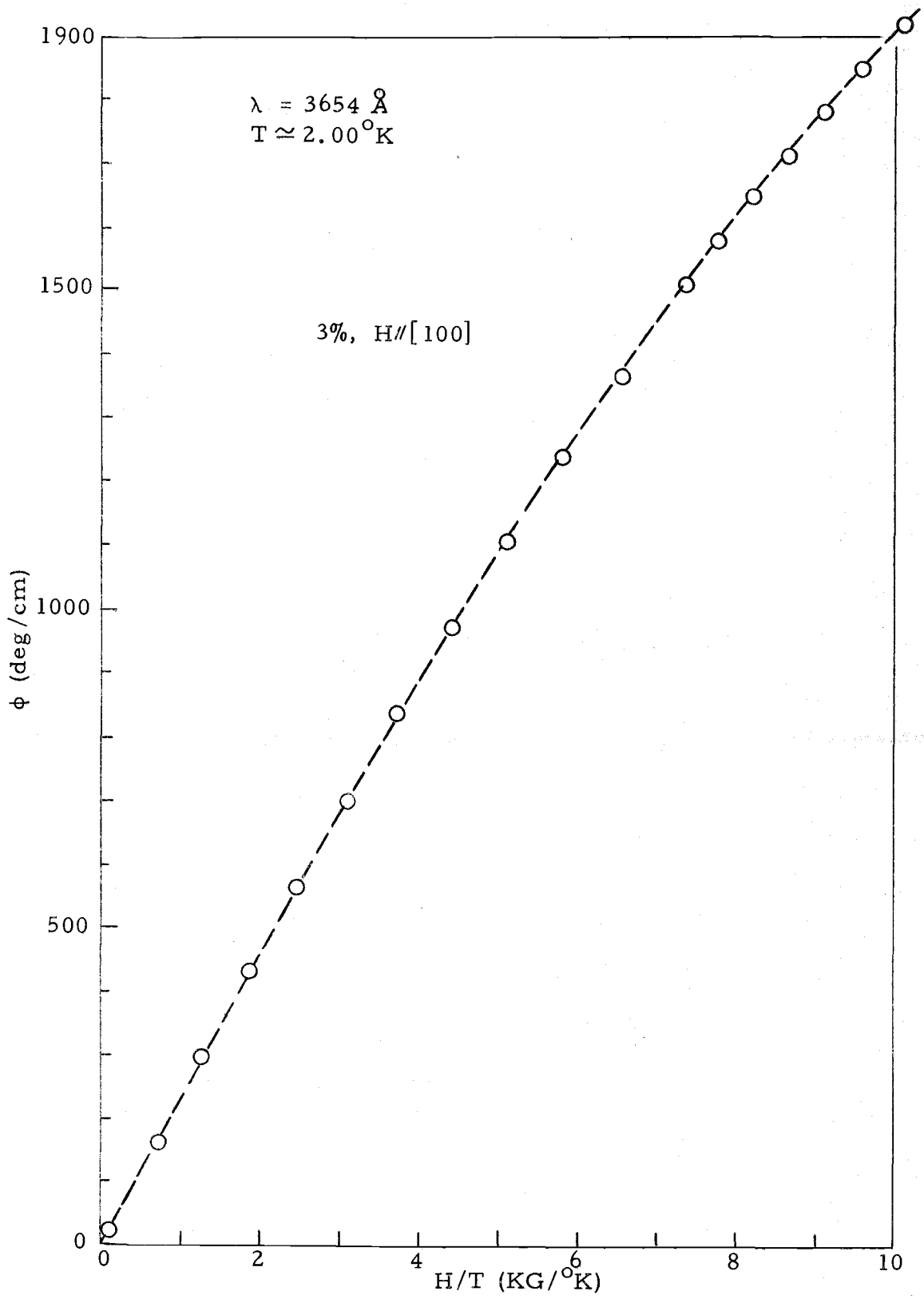

Figure 23. Rotation versus H/T for 3%, H//[100] crystals.

$$\phi = \phi_{\infty}^{c} \left[(2/3)\tanh(g_{\perp} \beta H/2kT) + (1/3)\tanh(g_{\parallel} \beta H/2kT)\right] \qquad (4\text{-}2\text{-}3)$$

and $$\phi = \phi_{\infty}^{d} \tanh(g \beta H/2kT) \qquad (4\text{-}2\text{-}4)$$

at H/T = 5, 8, and 10 KG/^{o}K for 0.5%, H//[100] and H//[111] crystals are shown in Fig. 22 with "x" and "•" signs upon the results of rotation measurements on these systems. Here we have taken ϕ_{∞}^{c} = 478^{o} and ϕ_{∞}^{d} = 424^{o}.

According to the consideration given in §2-4, we should have seen $\phi_{\infty}^{a} = \phi_{\infty}^{b} = 2\phi_{\infty}^{c} = 2\phi_{\infty}^{d}$, but this is not quite the case and their deviation varies from 10% to 15% depending on the paramagnetic systems being compared. We do not believe this to arise from the magnetic anisotropy of ϕ_{∞} but rather from the combined effects of deviation in N, i.e., variation of the nominal concentration 1%, 0.5%, etc., a possible slight misalignment of the crystal in its holder with respect to the field direction, presence of spin species not accounted for, and deviations in c_i, the relative spin populations, appearing in front of the hyperbolic tangents.

4-3. Field Dependent Spin-Bath Relaxation Times

(1) Kapitza Boundary Resistance Limited Spin-Bath Relaxation Times of 1% Ce^{3+}:CaF_2, H//[100] Crystal

The spin-bath relaxation times τ(H) have been measured as a function of the field H at temperatures around 2^{o}K, employing the

techniques described in Chapter 3. The results are shown in Fig. 24 (a plot of equivalent data at a fixed temperature via suitable normalization taking into account the nature of the Kapitza resistivity on temperature will produce a more sharply defined dependence of τ on H alone). Each of the points shown in the figure was obtained from a relaxation trace at known H and T, such as shown in Fig. 25 together with its signal height versus time plotted on semi-logarithmic scales. The relaxation traces obtained at fields roughly between 5 KG and 15 KG in general showed exponential response and displayed only one well defined relaxation time as seen from the trace analyzing (semi-logarithmic plot) and Fig. 26(A) where the trace was taken at a much faster time base. Data points in Fig. 24 (as well as Figs. 27, 28, and 29) showing error bars came from particularly noisy relaxation traces. The error bars are estimates of the range of relaxation times from these traces. The remaining data points represent traces with sufficient low noise levels for obtaining accurate relaxation times. The two dashed curves (τ vs. H) are generated from $\tau = C_c(H) r_k(T)$ (§ 2-3), using respectively $r_k = 1.28 \times 10^{-6}\ ^{o}K \cdot sec/erg$ for $T = 1.99^{o}K$ and $0.90 \times 10^{-6}\ ^{o}K \cdot sec/erg$ for $T = 2.06^{o}K$ (§ 5-2(2)), and known $C_c(H)$. Although a single trace presents all the appearance of true spin-lattice behavior, Fig. 24 shows that the aggregated relaxation times tend to lengthen as the external field increases in such a way that it cannot be accounted for by any common spin-lattice

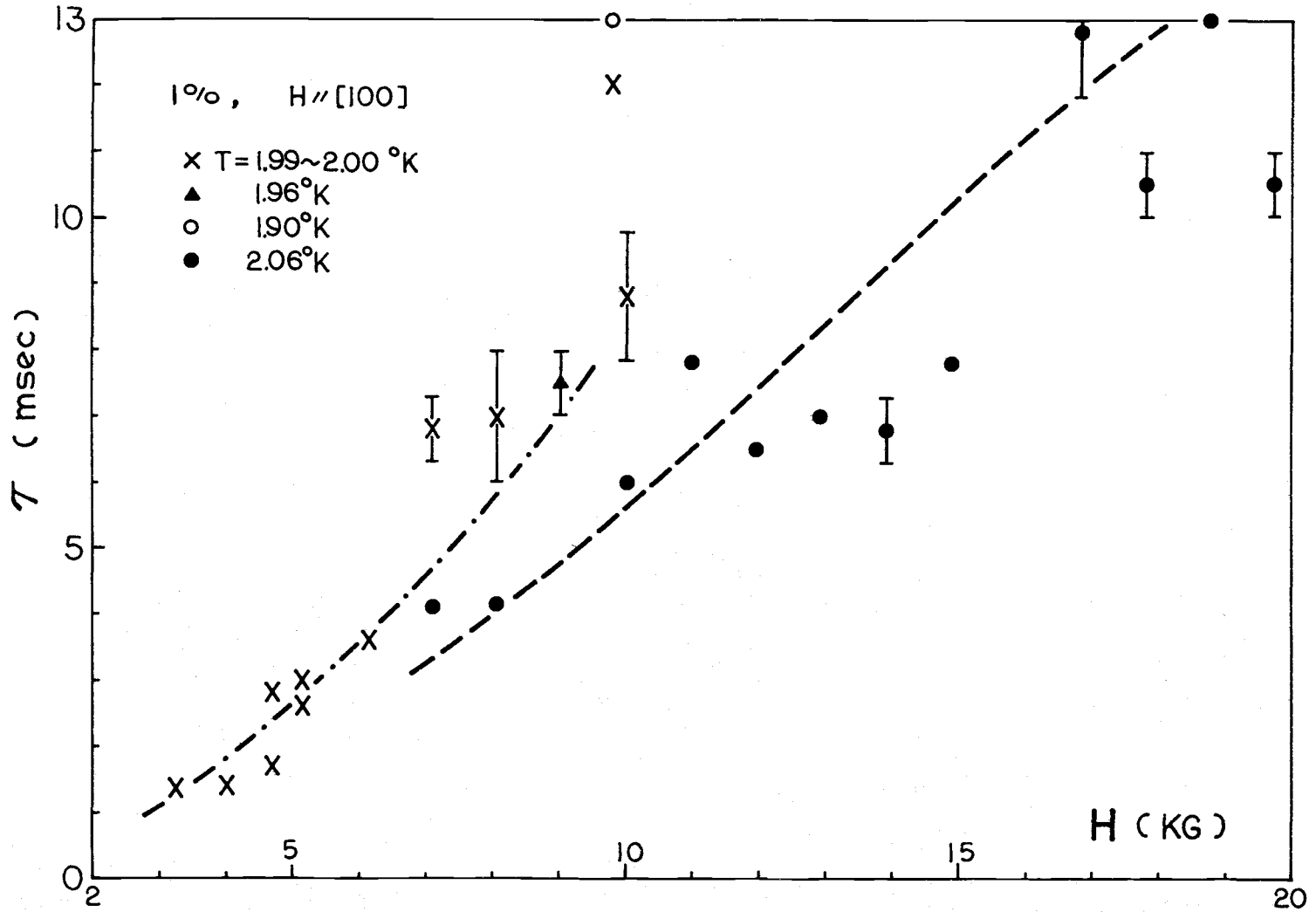

Figure 24. Field dependent spin-bath relaxation times of 1%, H//[100] crystal

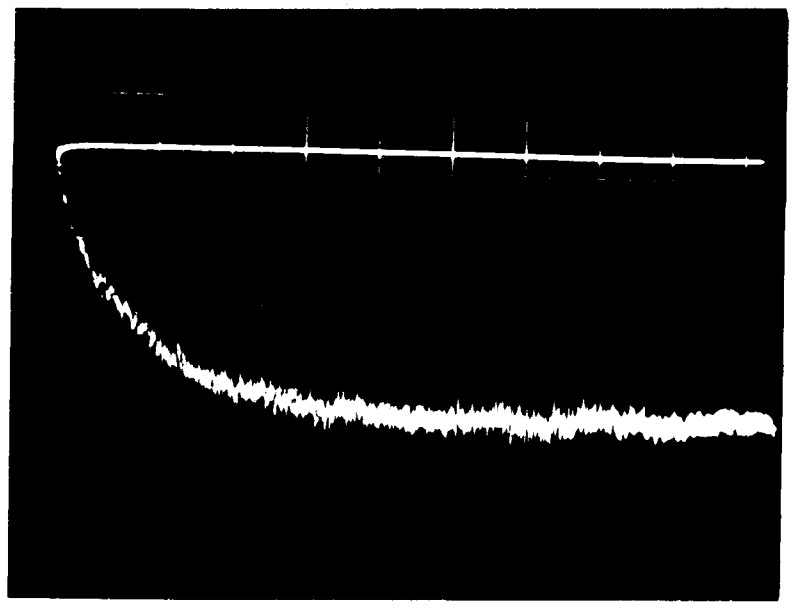

$H_f = H_i + \Delta H = 7.771 + 0.677$ KG
$T = 2.06^{\circ}K$
T. B. = 5 msec/div

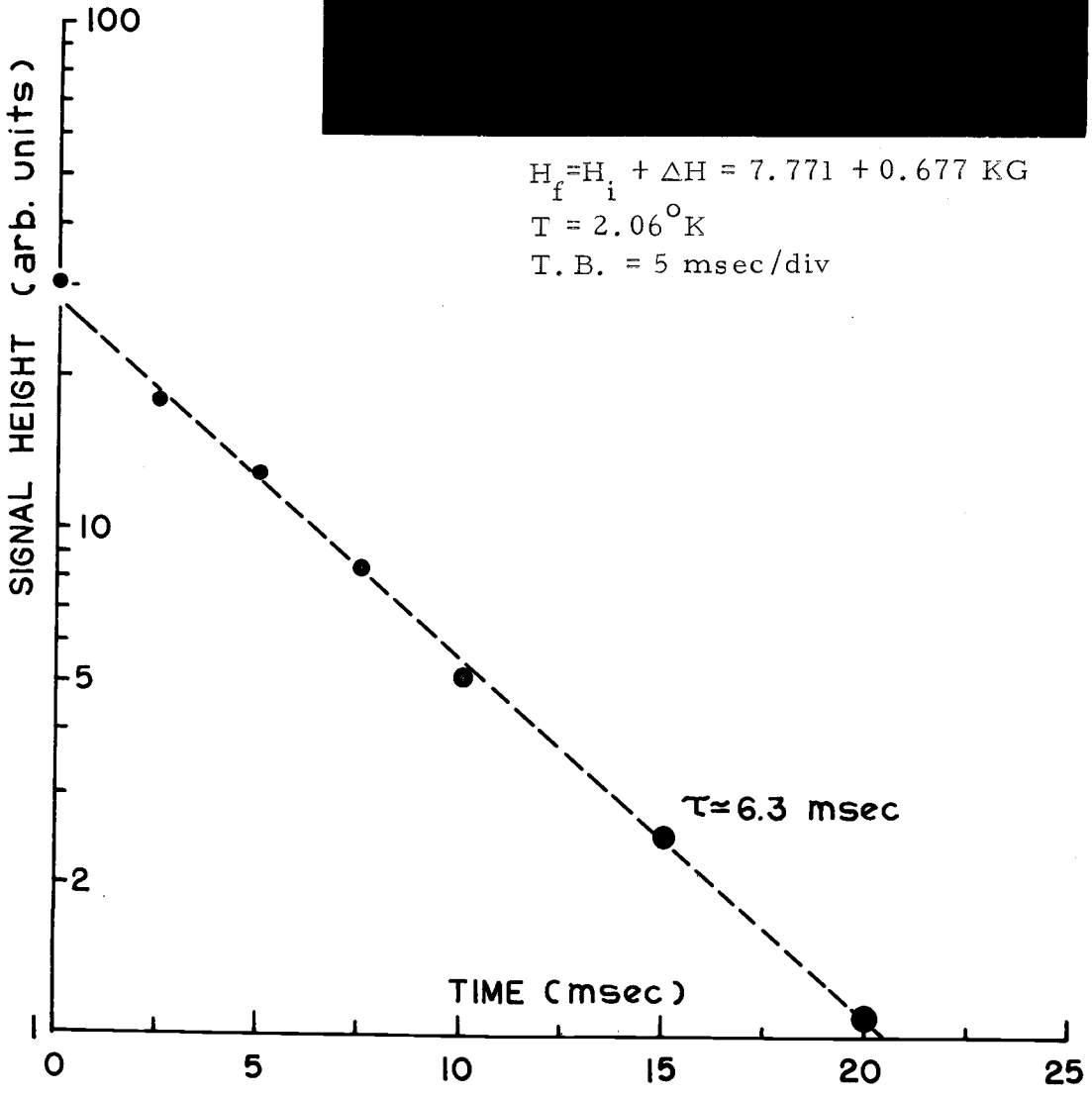

Figure 25. Typical relaxation trace obtained from 0.5%, H‖[100] crystal with its semi-logarithmic plot.

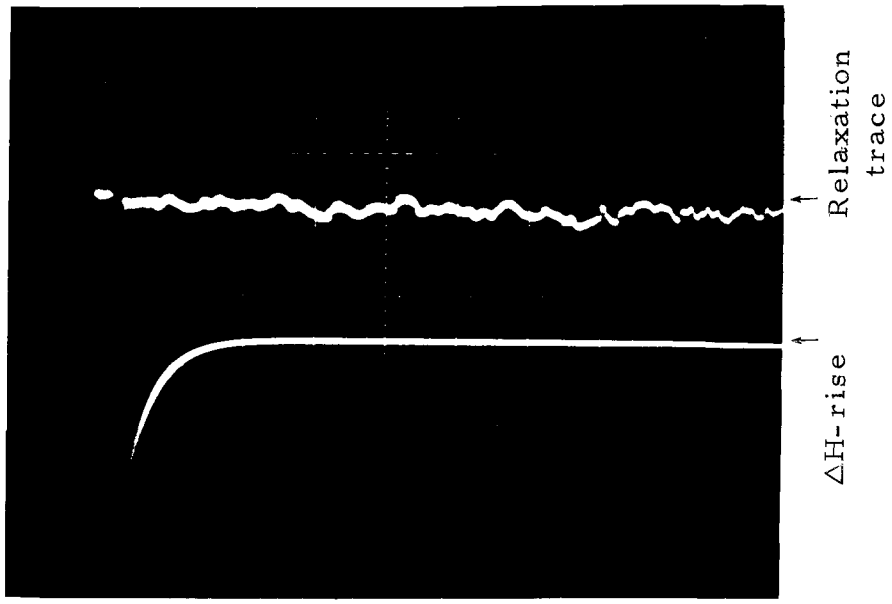

(A) 1%, H‖[100] crystal; $H_f=H_i + \Delta H = 0.971 + 0.300$ KG; T=2.00°K; T. B. =0.2 msec/div

(B) 0.5%, H‖[100] crystal; $H_f=H_i + \Delta H = 0.0 + 0.669$ KG; T=2.04°K; T. B. =0.2 msec/div

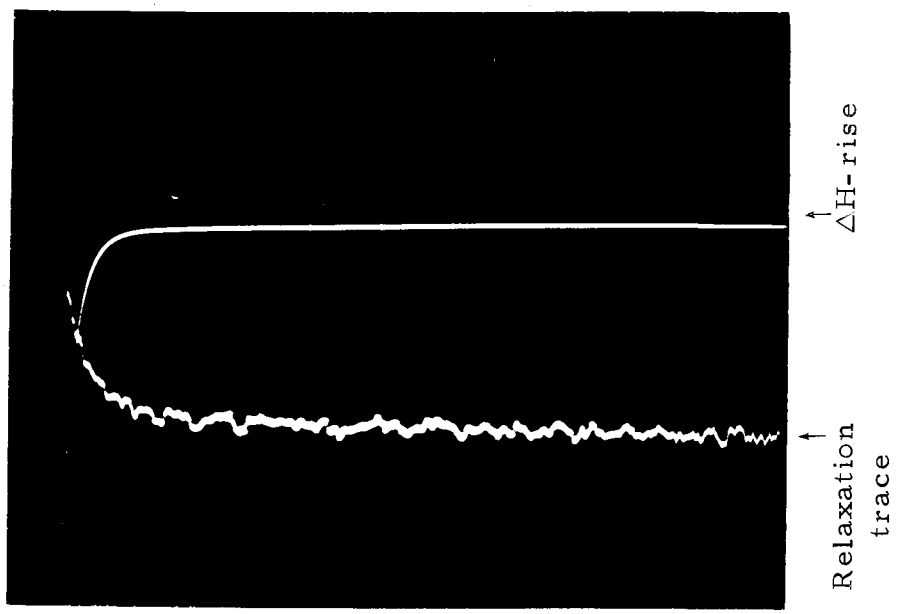

Figure 26. Relaxation traces of 1% (A) and 0.5% (B), H‖[100] crystals taken at a shorter (0.2 msec/div) time base.

relaxation processes. The shape of the increment is reminiscent of the Schottky specific heat curve for this kind of crystal at low fields. Furthermore, the results resemble those obtained from Kapitza limited CeES by Glättli (23). Putting all these facts together, we believe that the best interpretation of our results is obtained by assuming that the return to equilibrium of this system is limited by the phonon-bath coupling through the Kapitza boundary resistance. This model also predicts exponential response of the traces and an increase of relaxation times with the heat capacity of the crystal. The values of the Kapitza resistance per unit surface area, r_k, associated with the assumed model are calculated and applied to the problem in the next chapter.

(2) Results of Other Concentrations and Crystallographic Orientations of Crystals

The field dependent relaxation times of the 1%, H//[111] crystal are shown in Fig. 27 (note that here the data were collected at one common temperature). Figure 28 demonstrates the results of the 3%, H//[100] crystal. Relaxation times of the 0.5%, H//[100] and H//[111] crystals appear in Fig. 29, where many points taken both at low (< 5 KG) and high (> 15 KG) fields were rejected for reasons to be discussed in the next chapter. It will be seen that the limits on field strength which occur in the case of 0.5% impurity can be relaxed for the higher concentrations.

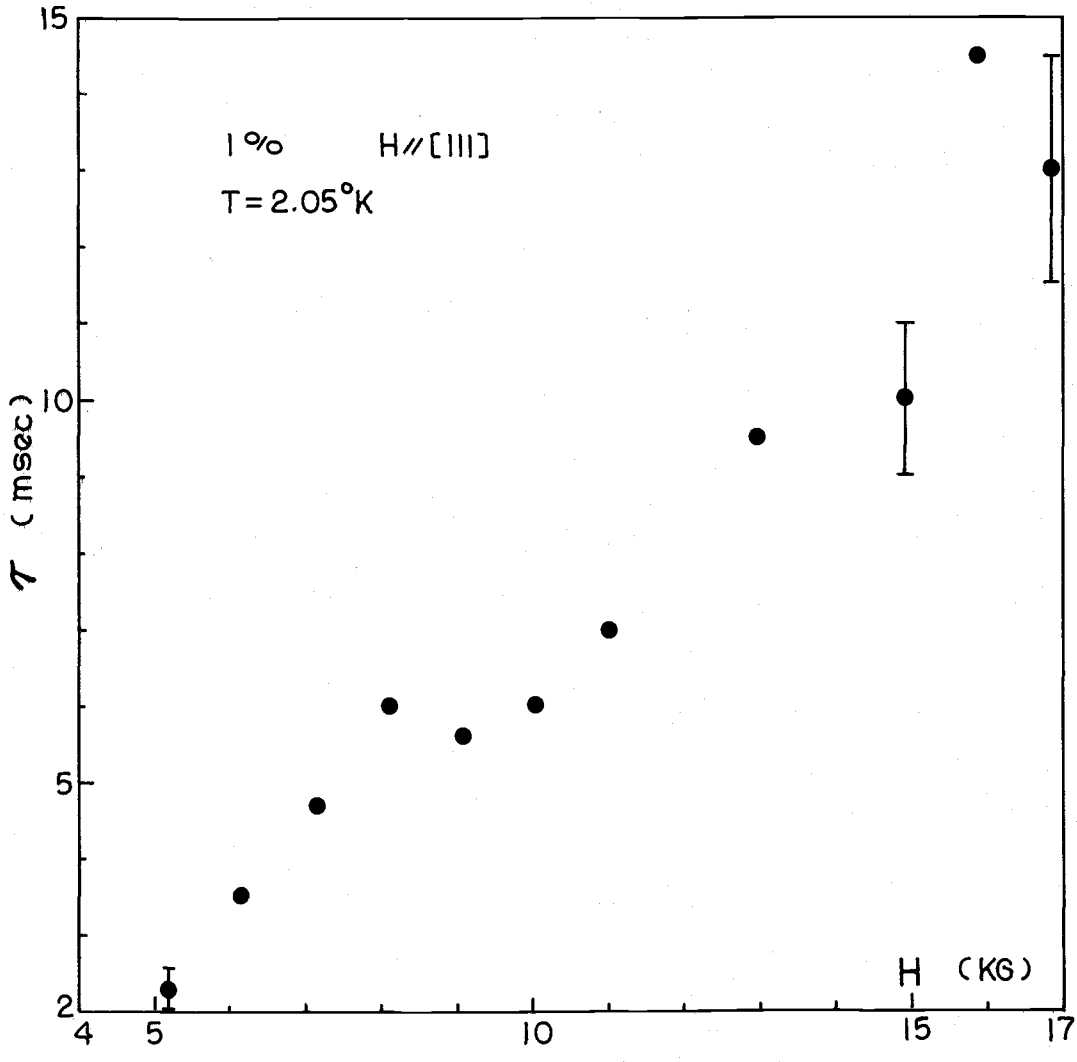

Figure 27. Field dependent spin-bath relaxation times of 1%, H//[111] crystal.

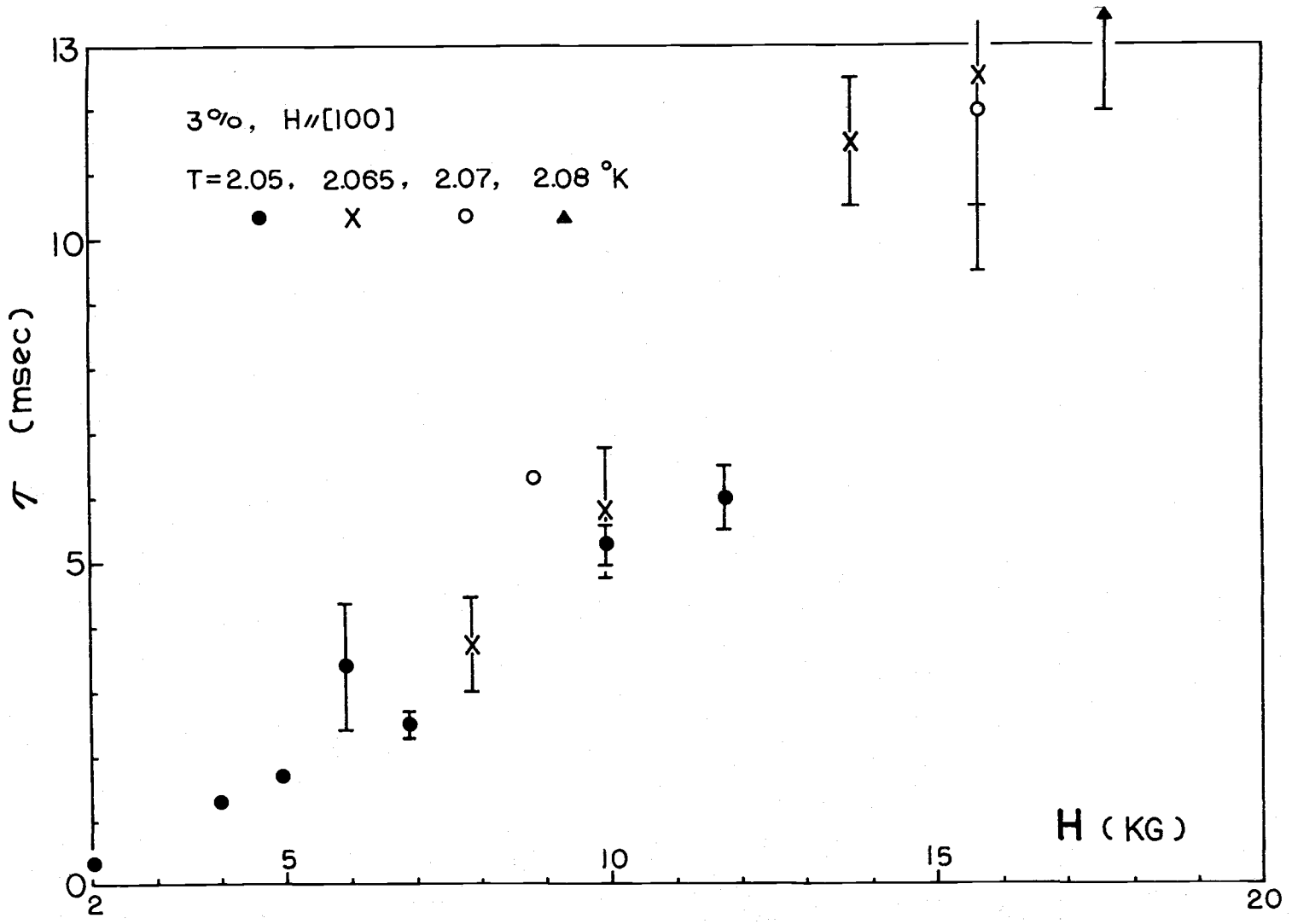

Figure 28. Field dependent spin-bath relaxation times of 3%, H//[100] crystal.

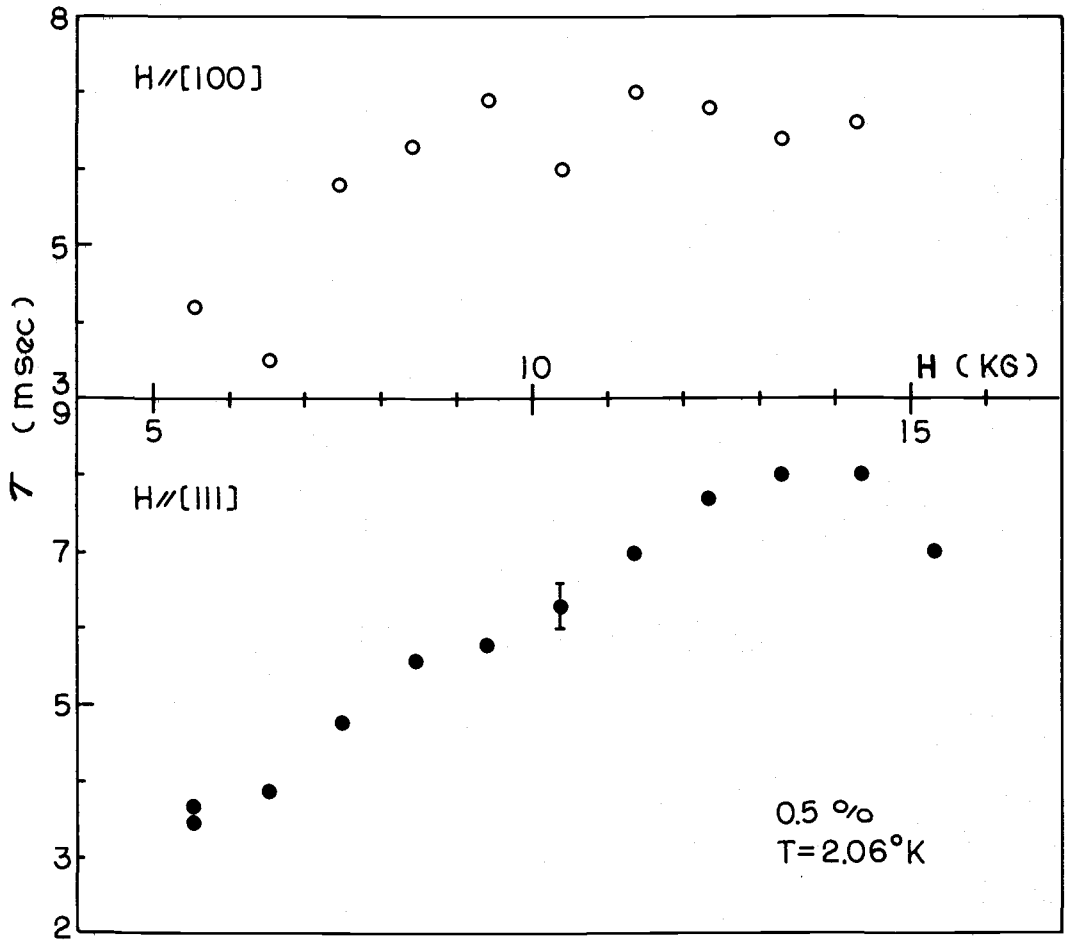

Figure 29. Field dependent spin-bath relaxation times of 0.5%, H//[100] and H//[111] crystals.

5. DISCUSSION

5-1. Spin-Lattice Relaxation Times

(1) Calculation of Spin-Lattice Relaxation Times of Common Processes—Dynamic Crystal Field Treatment

(i) As is discussed in Chapter 2, the ground state $J = 5/2$ multiplet of the Ce^{3+} ion splits into three Kramers doublets when situated in a CaF_2 crystal at a site which exhibits tetragonal symmetry. These doublets are designated as follows:

Energy Spacing (from ground doublet)	Wave Vectors
Δ_2	$\begin{vmatrix} \|f\rangle \\ \|e\rangle \end{vmatrix} = \cos\theta \left\|\pm 3/2\right\rangle - \sin\theta \left\|\mp 5/2\right\rangle$
Δ_1	$\begin{vmatrix} \|d\rangle \\ \|c\rangle \end{vmatrix} = \left\|\pm 1/2\right\rangle$
0	$\begin{vmatrix} \|b\rangle \\ \|a\rangle \end{vmatrix} = \sin\theta \left\|\mp 3/2\right\rangle + \cos\theta \left\|\pm 5/2\right\rangle$

The wave vectors $|a\rangle$, $|b\rangle$, ..., $|f\rangle$ diagonalize the Zeeman perturbation $\Lambda\beta\vec{H}\cdot\vec{J}$ when H is applied in the z-direction and hence are the zeroth order vectors. In order to make use of eq. (2-2-3) we need to consider the first order wave vectors of the ground doublet. When only an admixture within the $J = 5/2$ multiplet is considered, these can be given by

$$|a'\rangle = |a\rangle - \frac{2\Lambda\beta H\sin 2\theta}{\Delta_2}|f\rangle \quad \text{and} \quad |b'\rangle = |b\rangle - \frac{2\Lambda\beta H\sin 2\theta}{\Delta_2}|e\rangle$$

The replacement of $|a\rangle$ and $|b\rangle$ by $|a'\rangle$ and $|b'\rangle$ respectively in eq. (2-2-3) essentially leads to eq. (2-2-4), if higher order terms in H are ignored. The term $|\langle a|V_c|b\rangle|^2$ hence is replaced by

$$|\langle a'|V_c|b'\rangle|^2 = (2\Lambda\beta H\sin 2\theta/\Delta_2)^2 \sum_{n,m} |\langle a|V_n^m|e\rangle - \langle f|V_n^m|b\rangle|^2$$

$$= (2\Lambda\beta H\sin 2\theta/\Delta_2)^2 \sum_{n,m} |\langle -\tfrac{5}{2}|V_n^m|-\tfrac{3}{2}\rangle - \langle \tfrac{3}{2}|V_n^m|\tfrac{5}{2}\rangle|^2$$

$$\equiv (2\Lambda\beta H\sin 2\theta/\Delta_2)^2 \sum_{n,m} |M_n^m|^2 , \qquad (5\text{-}1\text{-}1)$$

where $V_n^m = g_n^{|m|} B_n^0 \hat{o}_n^m$ and the normalizing factors, $g_n^{|m|}$, are given by Scott et al. (39). The $\hat{o}_n^m$'s are operators in $\hat{J}_\pm$, $\hat{J}_z$ and are defined by $\hat{o}_n^m + \hat{o}_n^{-m} = \hat{0}_n^m$, $m > 0$; $\hat{o}_n^0 = \hat{0}_n^0$. The $\hat{0}_n^m$'s are the operators given by Baker et al. (54). Here V_n^m's in V_c are treated incoherently in the evaluation of the matrix elements. This is allowed from the consideration of the time incoherence of the various lattice modes and the random fluctuation of the thermal strains (39). The matrix elements in eq. (5-1-1) vanish for all n and m except n = 2, 4 and m = -1. For example we take

$$M_2^{-1} = g_2^1 B_2^0 (\langle -\tfrac{5}{2}| \hat{o}_2^{-1} |-\tfrac{3}{2}\rangle - \langle \tfrac{3}{2}|\hat{o}_2^{-1}|\tfrac{5}{2}\rangle) .$$

Since the explicit form of $\hat{o}_2^{-1}$ is $\frac{1}{4}[\hat{J}_-\hat{J}_+ + \hat{J}_+\hat{J}_-]$ and $\langle -\frac{5}{2}|\hat{o}_2^{-1}|-\frac{3}{2}\rangle = -\langle \frac{3}{2}|\hat{o}_2^{-1}|\frac{5}{2}\rangle = -\sqrt{5}$, we have $|M_2^{-1}|^2 = 20\,|g_2^1 B_2^0|^2 = 0.12 \times 10^5$ cm^{-2}, if g_2^1 and B_2^0 are taken to be 4.90 (39) and -5.02 cm^{-1} (§ 2-1), respectively. A similar calculation leads to $|M_4^{-1}|^2 = |12\sqrt{5} g_4^1 B_4^0|^2 = 1.02 \times$

10^5 cm^{-2}. The sum of all non-vanishing $|M_n^m|^2$ thus is $\sum_{n,m} |M_n^m|^2 = |M_2^{-1}|^2 + |M_4^{-1}|^2 = 1.14 \times 10^5$ cm^{-2}.

Recalling eq. (2-2-3), we have the relaxation rate of the direct process

$$T_{1d}^{-1} = (3k\beta^2 g_{\parallel}^2 / \pi\rho v^5 \hbar^4) |\langle a' | V_c | b' \rangle|^2 \cdot TH^2$$

$$= (3k\beta^2 g_{\parallel}^2 / \pi\rho v^5 \hbar^4) \cdot (2\Lambda\beta \sin 2\theta / \Delta_2)^2 \sum_{n,m} |M_n^m|^2 \cdot TH^4 . \tag{5-1-2}$$

Taking $\rho = 3.18$ gm/cm^3, $v = 4 \times 10^5$ cm/sec, $g_{\parallel} = 3.038$, $\Lambda = 6/7$, $\sin 2\theta = 0.7546$, $\Delta_2 = 579$ cm^{-1} (§ 2-1), and $\sum_{n,m} |M_n^m|^2 = 1.14 \times 10^5$ cm^{-2}, we evaluate T_{1d}^{-1} from eq. (5-1-2) to find $T_{1d}^{-1} \simeq 1.26 \times 10^{-16}$ $(^oK \cdot gauss^4 \cdot sec)^{-1} \cdot TH^4$. Typically, if we take $T = 2\,^oK$ and $H = 10$ KG, we have $T_{1d}^{-1} \simeq 2.52$ sec^{-1} or $T_{1d} \simeq 0.40$ sec.

If instead, H is applied perpendicular to the crystal z-axis, the first order perturbed wave vectors for the lowest doublet have the form

$$|1'\rangle = |1\rangle + (\sqrt{2}\Lambda\beta H \sin\theta / \Delta_1) |3\rangle - (\sqrt{5}\Lambda\beta H \cos 2\theta / 2\Delta_2) |6\rangle$$

$$|2'\rangle = |2\rangle - (\sqrt{2}\Lambda\beta H \sin\theta / \Delta_1) |4\rangle - (\sqrt{5}\Lambda\beta H \cos 2\theta / 2\Delta_2) |5\rangle$$

where $|1\rangle$, $|2\rangle$, ..., $|6\rangle$ are the zeroth order wave vectors just like $|a\rangle$, $|b\rangle$, ..., $|f\rangle$ in the H//z case. The matrix element of $V_c = \sum_{n,m} V_n^m$ thus is

$$\langle 1' | V_c | 2' \rangle = (\sqrt{2}\Lambda\beta H \sin\theta / \Delta_1)[-\langle 1 | V_c | 4 \rangle + \langle 3 | V_c | 2 \rangle] + \underbrace{0(\Delta_2^{-1}) + 0(H^2)}_{\text{to be ignored}}$$

and the square of it $|\langle 1'|V_c|2'\rangle|^2 = (\sqrt{2}\Lambda\beta H\sin\theta/\Delta_1)^2 \sum_{n,m}|M_n^m|^2$, where $\sum_{n,m}|M_n^m|^2 \equiv \sum_{n,m}|-\langle 1|V_n^m|4\rangle + \langle 3|V_n^m|2\rangle|^2 \simeq 3.4 \times 10^5\ \mathrm{cm}^{-2}$.

Equation (5-1-2) now should bear the following form

$$T_{1d}^{-1} = (3k\beta^2 g_\perp^2/\pi\rho v^5\hbar^4)(\sqrt{2}\Lambda\beta H\sin\theta/\Delta_1)^2 \sum_{n,m}|M_n^m|^2 \cdot TH^4 . \quad (5\text{-}1\text{-}3)$$

The rate, T_{1d}^{-1}, as calculated by taking $g_\perp = 1.396$ and $\Delta_1 = 110\ \mathrm{cm}^{-1}$ (§2-1) from eq. (5-1-3), is $3.35 \times 10^{-16}(^\circ\mathrm{K}\cdot\mathrm{gauss}^4\cdot\mathrm{sec})^{-1}TH^4$, which at $T = 2^\circ\mathrm{K}$ and $H = 10$ KG yields $T_{1d} \simeq 0.15$ sec and thus is slightly shorter than that for the H//z case.

(ii) We next calculate the relaxation rate of the Orbach process, T_{10}^{-1}, for the H//z case from eq. (2-2-5)

$$T_{10}^{-1} = \frac{3}{2\pi\rho v^5\hbar}\left(\frac{\Delta_1}{\hbar}\right)^3 \left[\sum_{n,m}|\langle a|V_n^m|c\rangle|^2 + \sum_{n,m}|\langle a|V_n^m|d\rangle^2\right] \cdot \exp(-\Delta_1/kT) ,$$

where $\sum_{n,m}|\langle a|V_n^m|c\rangle|^2$ and $\sum_{n,m}|\langle a|V_n^m|d\rangle|^2$ have numerical values equal to $5.47 \times 10^4\ \mathrm{cm}^{-2}$ and $8.47 \times 10^4\ \mathrm{cm}^{-2}$, respectively. Employing the values of ρ, v, and Δ_1 we have used in the previous calculation, T_{10}^{-1} is found to be

$$T_{10}^{-1} \simeq 6.87 \times 10^{11}\exp(-\Delta_1/kT)\ \mathrm{sec}^{-1} .$$

Since at $2^\circ\mathrm{K}$, $\Delta_1/kT \simeq 80$ and $\exp(-\Delta_1/kT) \sim 10^{-35}$, the Orbach process takes too long to contribute as a relaxation mechanism. The situation is also true for the H⊥z case.

(iii) After calculating and substituting $\sum_{n,m} |<a|V_n^m|c>|^2 \cdot \sum_{n,m} |<c|V_n^m|b>|^2 \simeq 4.6 \times 10^{10}\ cm^{-4} \simeq 7.27 \times 10^{-54}\ erg^4$ into eq. (2-2-8), the relaxation rate of the Raman process, T_{1R}^{-1}, for the H//z case can be given by

$$T_{1R}^{-1} = \frac{9!\hbar^2}{\pi^3 \rho^2 v^{10} \Delta_1^4} \left(\frac{kT}{\hbar}\right)^9 \sum_{n,m} |<a|V_n^m|c>|^2 \cdot \sum_{n,m} |<c|V_n^m|b>|^2 \simeq 4.95 \times 10^{-6} (sec^{-1} \cdot {}^oK^{-9}) T^9$$

At 2^oK, $T_{1R}^{-1} \simeq 2.35 \times 10^{-3}\ sec^{-1}$ which amounts to $T_{1R} \simeq 400$ sec. The other case, H⊥z, gives approximately the same order of magnitude.

(2) Upper Limit of Spin-Lattice Relaxation Time

In the foregoing chapter we have stated that relaxation times in the high field region cannot be explained on the basis of spin-lattice processes discussed here. The above calculation on T_{1d}, T_{10}, and T_{1R} further confirms this point. In the low field region, say H < 1 KG, the phonon system should serve as a good reservoir for the spins and thus provide an excellent opportunity to observe the spin-lattice behavior. However, the change in the relaxation trace occurring within the time of field switching as indicated in Fig. 26(B) clearly shows that the L/R time constant ($\sim$0.1 msec) can not be shorter

than the spin-lattice relaxation times of our system, i.e., the true spin-lattice relaxation time must be $\lesssim 0.1$ msec.

Although very long relaxation times due to the direct process for the Kramers ion Dy^{3+} have been observed and reported (13), the hidden spin-lattice relaxation times of our system are much too rapid to be in agreement with the results of the calculation.

5-2. Kapitza Limited Process and the Limitation of the Model

(1) Heat Capacity of the Crystal

The contributions of both spin and phonon systems to the heat capacity of the crystal are essential to the discussion of the Kapitza resistance R_k.

(i) Estimation of the phonon specific heat was made by employing Debye's T^3 law (55) and by taking $\theta_D = 505^\circ K$ for CaF_2 at helium temperatures (56). An explicit equation can be written as

$$C_L = 5.833 \times 10^{10} (T/\theta_D)^3 \quad \text{erg}/^\circ\text{K}\cdot\text{mole} . \qquad (5\text{-}2\text{-}1)$$

Since the impurity concentrations and size of the crystals are different, the number of moles n in each crystal are not the same. To calculate n, we first weighed the crystal to obtain the weight W_c, which is then divided by the formula weight of the crystal of specific impurity concentration W_F to yield the value of n. Multiplication of

C_L from eq. (5-2-1) by n at a given temperature then gives the heat capacity of the phonon system.

(ii) The specific heat of the spin system requires information on the total number of spins N, distributed over a presumed two-level system, and the g values of each spin species present. For the case where H//[111] we have only one species and the specific heat can be expressed by

$$C_s = N_k(g\beta x/k)^2 \exp(g\beta x/k) \,/\, [\exp(g\beta x/k) + 1]^2 , \qquad (5\text{-}2\text{-}2)$$

where $x \equiv H/T$ and $g = 2.09$ for the tetragonal site symmetry. However, there are two spin species in the H//[100] case and we have instead

$$C_s = (2Nk/3)(g_\perp \beta x/k)^2 \exp(g_\perp \beta x/k) \,/\, [\exp(g_\perp \beta x/k) + 1]^2 + (Nk/3)(g_{||} \beta x/k)^2 \exp(g_{||} \beta x/k) \,/\, [\exp(g_{||} \beta x/k) + 1]^2 , \qquad (5\text{-}2\text{-}3)$$

where $g_\perp = 1.396$ and $g_{||} = 3.038$ for tetragonal site symmetry. To evaluate N all we need to do is multiply n by N_0, Avogadro's number, and the impurity concentration percentage in the crystal. We list n, C_L, and N for each crystal in Table 3.

Table 3. List of heat capacity and total spin number for each crystal.

Crystal	n (moles)	C_L (erg/°K)		N (10^{20} spins)
3.0%, H//[100]	0.0772	301.1	(2.05°K)	13.948
1.0%, H//[100]	0.0743	294.1	(2.06°K)	4.475
0.5%, H//[100]	0.0810	320.6	(2.06°K)	2.439
1.0%, H//[111]	0.0747	291.4	(2.05°K)	4.499
0.5%, H//[111]	0.0799	316.2	(2.06°K)	2.406

(2) Kapitza Resistance

The experimental values of τ together with the calculated heat capacities of the crystal at specific values of the field and temperature allow us to estimate the Kapitza resistance per unit surface area, $r_k = R_k/S$, from the relation $\tau = C_c R_k/S = C_c r_k$ (§2-3). These r_k's are then taken and plotted against H within the region of applicability of the model to examine their constancy in the field. The results are shown in Figs. 30 and 31 for the cases of 1% and 0.5% impurity concentrations. The plot of the 3% case is precluded by the complexity of the Schottky specific heat of the spin system due to the presence of vague and complex g values in its EPR spectrum (Fig. 19). The average values of r_k of the two 1% crystals may be summarized as shown in Table 4. The field constancy of r_k in both 0.5% crystals as indicated in Fig. 31 is fairly poor and the reason for it is probably due to the temperature lag in the helium vapor thermometer. In

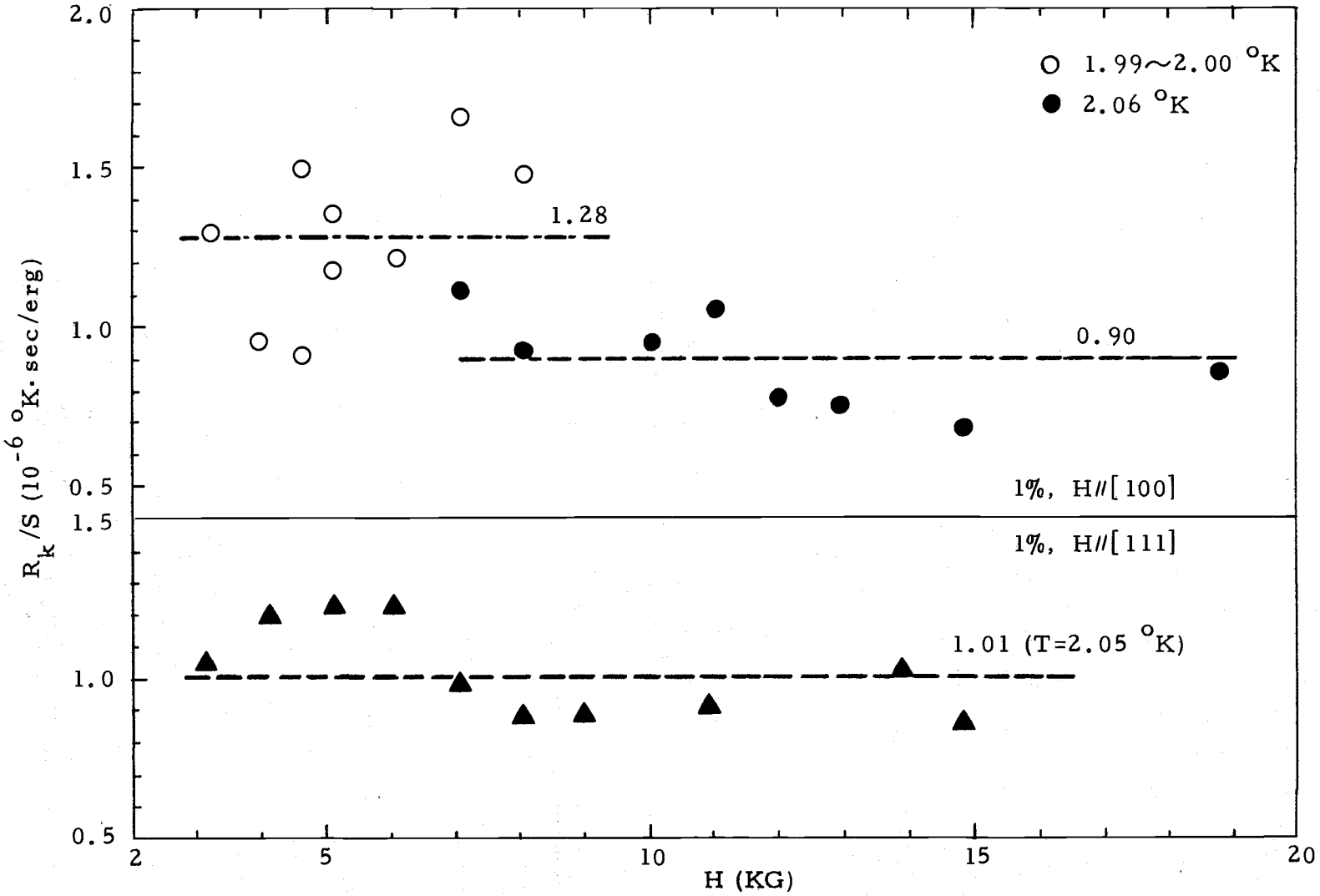

Figure 30. Plot of r_k^* versus H of the 1% crystals.

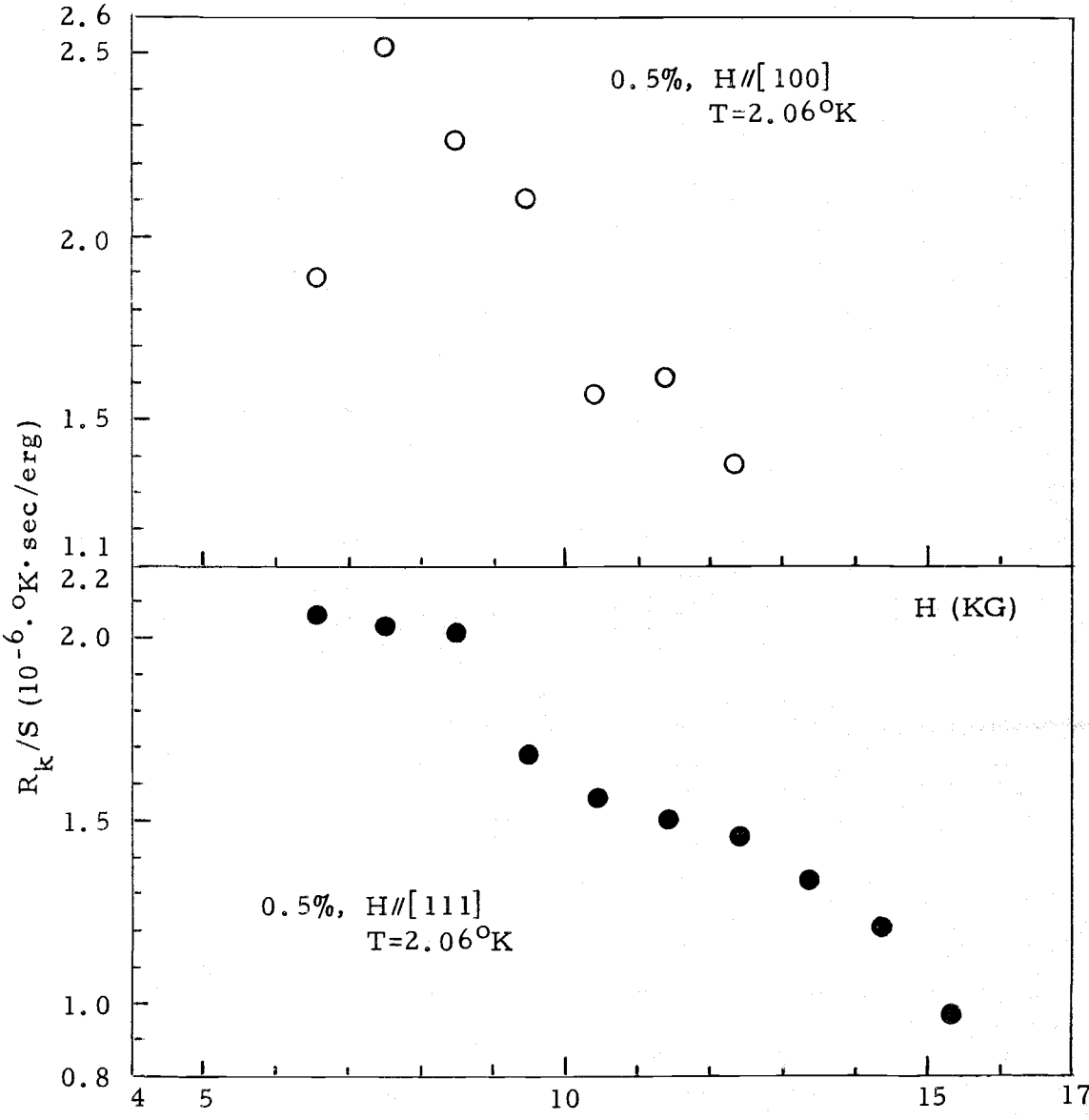

Figure 31. Plot of r_k versus H of the 0.5% crystals.

Table 4. Values of r_k of the 1% crystals.

1% Crystal	r_k (10^{-6} °K sec/erg)
H//[100]	1.28 ± 0.08 (1.99°K)
	0.90 ± 0.05 (2.06°K)
H//[111]	1.01 ± 0.03 (2.05°K)

other words, at high fields and low liquid He level the constant heating of liquid He (this implies a continuously rising T_B) from joule losses in non-superconducting element of the electric current carrier should not be neglected and the true T_B should be recorded as the average T right before and after field switching and not just the temperature recorded before the action. Such a lagging in temperature response means the phonon band we employed to calculate r_k is actually slightly higher than what it was. Moreover, while rising, the higher T_B also causes a smaller value of r_k to be operative which in turn generates a shorter τ. Accordingly, the r_k calculated from the registered trace and temperature is likely to be smaller than its true value and the scattering of r_k toward lower values to be worsened as the fields go to higher values. Assessment of the true values of r_k for the 0.5% crystals hence is of difficulty. The average r_k, despite its physical meaning, can be given respectively as 1.76 and 1.91 (in units of 10^{-6} °K · sec/erg) at $T \simeq 2.06$°K for the H//[111] and H//[100]

crystals. It follows then from facts concluded from Figs. 30 and 31 that a reasonable value of r_k should fall in $(1\sim2) \times 10^{-6}$ °K · sec/erg for all crystals used at temperatures near 2°K.

(3) Lower Field Limit of the Model

(i) There are two facts which govern the lower field limit of the model. We first consider eq. (2-3-3). This equation is valid under the assumptions $T_B \simeq T_s$ and $\sigma \equiv C_s \tau_{ph}/C_L T_l >> 1$. Although $\tau_{ph} \gtrsim T_l$ might be true (but we do not know by exactly how much), at low fields, C_s becomes so small compared to C_L that the condition $\sigma >> 1$ ceases to hold thus causing the breakdown of the model. In order to maintain this condition, our experimental data of the 1% crystal suggest that we take $C_s/C_L \simeq 2.5$, which at T = 2°K requires an external field of 4.5 KG and 3.0 KG for the 0.5% and 1% cases, respectively.

(ii) Another factor we need to consider is the validity of $T_B >> \delta T$ (or $T_s \simeq T_c \gtrsim T_B$). To do this we need to estimate the value of δT and then compare it with T_B. Let us take H_i to be the initial field and $H_f = H_i + \Delta H$ to be the final field after pulsing is applied to a two-level spin system with population numbers N_a and $N_b (= N - N_a)$ for the ground and excited states respectively. The difference in spin population when $H = H_i$ is given by

$$n = N_a - N_b = N\tanh(g\beta H_i/2kT_B) , \tag{5-2-4}$$

and when $H = H_f$ is given by

$$n' = N'_a - N'_b = N\tanh(g\beta H_f/2kT_B) . \tag{5-2-5}$$

The number of spin flips is thus given by

$$\Delta n = (n'-n)/2 = (N/2)[\tanh(g\beta H_f/2kT_B) - \tanh(g\beta H_i/2kT_B)] . \tag{5-2-6}$$

Since most of these flips occur at $H \simeq H_f$, the energy transferred from the crystal to the bath is approximately $\Delta\epsilon = g\beta H_f \cdot \Delta n$. Strong spin-lattice coupling suggests that the crystal reaches a uniform higher temperature T_c^* in a time interval much shorter than the spin-bath relaxation time τ. Thus at the end of field switching the rise in temperature can be given as

$$\delta T = T_c^* - T_B = \Delta\epsilon/C_c = g\beta H_f \cdot \Delta n/C_c , \tag{5-2-7}$$

where Δn is given by eq. (5-2-6). If it so happens that even under the condition $C_s >> C_L$ for $g\beta H/kT_B$ is sufficiently small, eq. (5-2-7) can be expressed by

$$\delta T \simeq \frac{Ng\beta H_f}{2}\left(\frac{g\beta H_f}{2kT_B} - \frac{g\beta H_i}{2kT_B}\right)\frac{4}{Nk}\left(\frac{kT_B}{g\beta H_f}\right)^2$$

$$= \frac{T_B}{H_f}(H_f - H_i) = \frac{\Delta H}{H_f}\, T_B , \tag{5-2-8}$$

where we have used the explicit form of the heat capacity of the spin system

$$C_s = \frac{Nk(g\beta H_f/kT_B)^2 \exp(g\beta H_f/kT_B)}{[\exp(g\beta H_f/kT_B) + 1]^2} \simeq \frac{Nk}{4}\left(\frac{g\beta H_f}{kT_B}\right)^2 \simeq C_c$$

and the small argument approximation of the hyperbolic tangent. Since we need at least a certain level of ΔH to get enough change in rotation and eq. (5-2-8) requires larger H_f for smaller δT at a fixed value of ΔH, we are limited as to how small we can make H_f and still guarantee $\delta T << T_B$.

While eq. (5-2-8) imposes the condition for determining the lower limit of field, the experimental traces themselves also render the criterion for such a limit. Suppose a trace taken from the screen has the shape as indicated in Fig. 32 displaying the relaxing situation of our problem as discussed in §2-3 (actual traces have been found with this general form).

As the rotation is proportional to the difference in spin population, from eq. (5-2-4), the initial rotation ϕ_i of the system is

$$\phi_i = \alpha N \tanh(g\beta H_i/2kT_B) \simeq \alpha N g\beta H_i/2kT_B ,$$

where αN is the saturation rotation and the approximation is made under the condition $g\beta H_i/2kT_B << 1$. Similarly, the rotation at the end of the time interval $\Delta t \sim T_1$, i.e., $t = t_f$, can be given as

$$\phi_f = \alpha N \tanh(g\beta H_f/2kT_c^*) \simeq \alpha N g\beta H_f/2kT_c^* ,$$

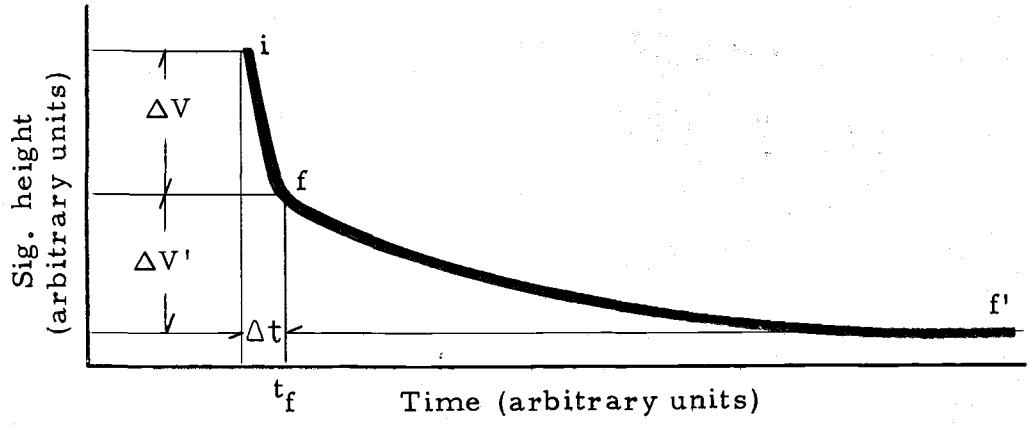

Figure 32. Schematic trace of the spin-phonon-bath relaxation in the case of phonon bottleneck occurring.

and the ultimate rotation as

$$\phi_{f'} = \alpha N \tanh(g\beta H_f/2kT_B) \simeq \alpha N g \beta H_f/2kT_B \ .$$

The change in signal heights ΔV and $\Delta V'$ associated with $\Delta\phi \equiv \phi_f - \phi_i$ and $\Delta\phi' \equiv \phi_{f'} - \phi_f$ are $\Delta V = V(\cos^2\phi_f - \cos^2\phi_i) \simeq -V(\phi_f - \phi_i)$ and $\Delta V' = V(\cos^2\phi_{f'} - \cos^2\phi_f) \simeq -V(\phi_{f'} - \phi_f)$, respectively. Besides their definition, ϕ_i and $\phi_{f'}$ satisfy the relation $(\phi_{f'} + \phi_i)/2 - \phi_a = 45^\circ$, where ϕ_a is the analyzer setting, so as to linearlize the cosine squared function as described in § 3-1(2). We define the heating factor γ by

$$\gamma \equiv \frac{\Delta V'}{\Delta V} = \frac{\Delta\phi'}{\Delta\phi} = \left(\frac{H_f}{T_B} - \frac{H_f}{T_c^*}\right) \Big/ \left(\frac{H_f}{T_c^*} - \frac{H_i}{T_B}\right)$$

$$= \frac{H_f T_c^* - H_f T_B}{H_f T_B - H_i T_c^*} = \frac{H_f(T_c^* - T_B)}{H_f T_B - H_i T_c^*} \gtrsim 0 \qquad (5\text{-}2\text{-}9)$$

If the lattice is really pulled up in temperature in keeping with our hypothesis and model, the heating factor γ must be large ($\Delta V' \gg \Delta V$)

and in the extreme case $\gamma \to \infty$ or $H_f T_B - H_i T_c^* = 0$. This then amounts to

$$(H_i + \Delta H)T_B = (T_B + \delta T)H_i$$

$$\text{or} \quad \delta T = \frac{\Delta H}{H_i} T_B = \frac{\Delta H}{H_f - \Delta H} T_B \xrightarrow{H_f >> \Delta H} \frac{\Delta H}{H_f} T_B , \tag{5-2-10}$$

which is exactly the same expression as eq. (5-2-8) found previously. It is also interesting to examine the general expression for the lattice (phonon band) temperature rise in the case of bottleneck occurring. In terms of γ, T_c^* can be written as

$$T_c^* = (\gamma + 1)H_f T_B / (H_f + \gamma H_i) ,$$

and the temperature rise hence can be given by

$$\delta T = T_c^* - T_B = \Delta H T_B / [(H_f / \gamma) + H_i] . \tag{5-2-11}$$

We see in the extreme case $\gamma \to \infty$, δT reduces to our previous result

$$\delta T \simeq \frac{\Delta H}{H_i} T_B \xrightarrow{H_f >> \Delta H} \frac{\Delta H}{H_f} T_B .$$

Now taking the field that generates $\delta T \simeq 10\%$ of T_B for a specific ΔH as the lower limit of the model, we found $H_f \simeq 3$ KG and 7 KG for the 1% ($\Delta H \simeq 0.3$ KG) and 0.5% ($\Delta H \simeq 0.7$ KG) crystals, respectively. Signal responses taken at these limits in general show single well defined exponential traces and hence are experimentally verified. The limit for the 3% crystal can be pushed down even further ($H_f \simeq 1.5$ KG) due to the application of smaller ΔH.

(4) The Upper Field Limit of the Model

(i) The existence of an upper field limit arises partially from the non-linearity of the Faraday rotation as a function of H/T. As described in § 3-1(2)(iii) the analyzer setting ϕ_a is obtained from $\phi_a = (\phi_i + \Delta\phi/2) - 45^o$, where ϕ_i is the rotation for each H_i and $\Delta\phi$ the additional rotation as the result of the constant ΔH pulsing. Although we have worked out ϕ_i from the calibration curve, we have left $\Delta\phi$ uncalibrated thinking it would not be important due to its smallness. The uncalibrated rotation due to ΔH generates an offset in the analyzer setting which in turn causes the signal to shift from its maximum response as well as to display non-exponential behavior at high fields. A typical trace of this sort is shown in Fig. 33. Traces of this nature were discarded in the analysis. Taking the 0.5%, H//[111] crystal as an example, a coil current of $I_c = 7.7$ amp will generate $\Delta H = 0.737$ KG. $\Delta\phi$ produced by this ΔH at $H_i = 0$ KG is 30^o as we have designed, whereas at $H_i = 14.571$ KG it is only 21^o. In the latter case, the analyzer setting for the experiment was set at 30^o behind the rotation of $H_i(537^o)$, i.e., at 507^o, since we had taken $\Delta\phi = 30^o$ for all H_i's, whereas the correct setting should be 502^o if the calibrated value of $\Delta\phi(=21^o)$ was taken. The error for higher concentrations was somewhat reduced, especially for the 3% case. Therefore, our high field limits should be around $H_f = 15$ KG for the 0.5% crystal,

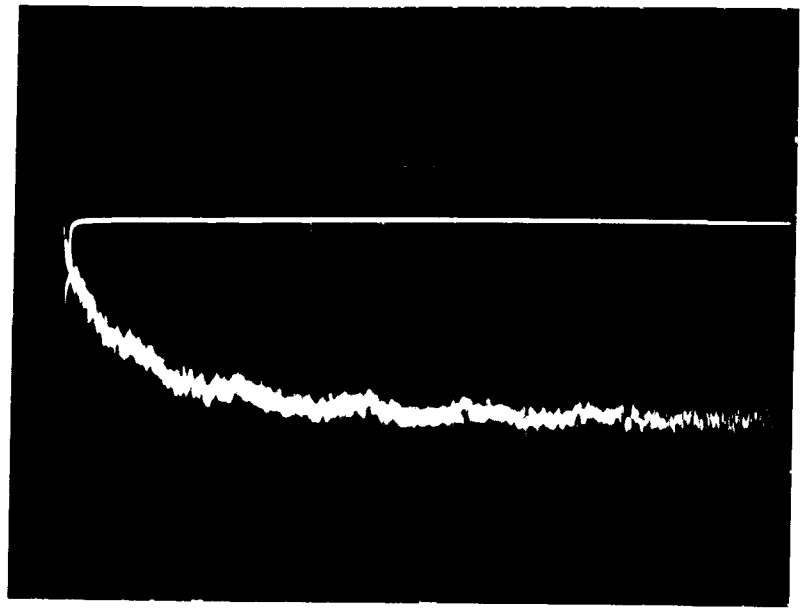

H_f = 18.458 KG, T. B. = 5 msec/div
ΔH = 0.677 KG

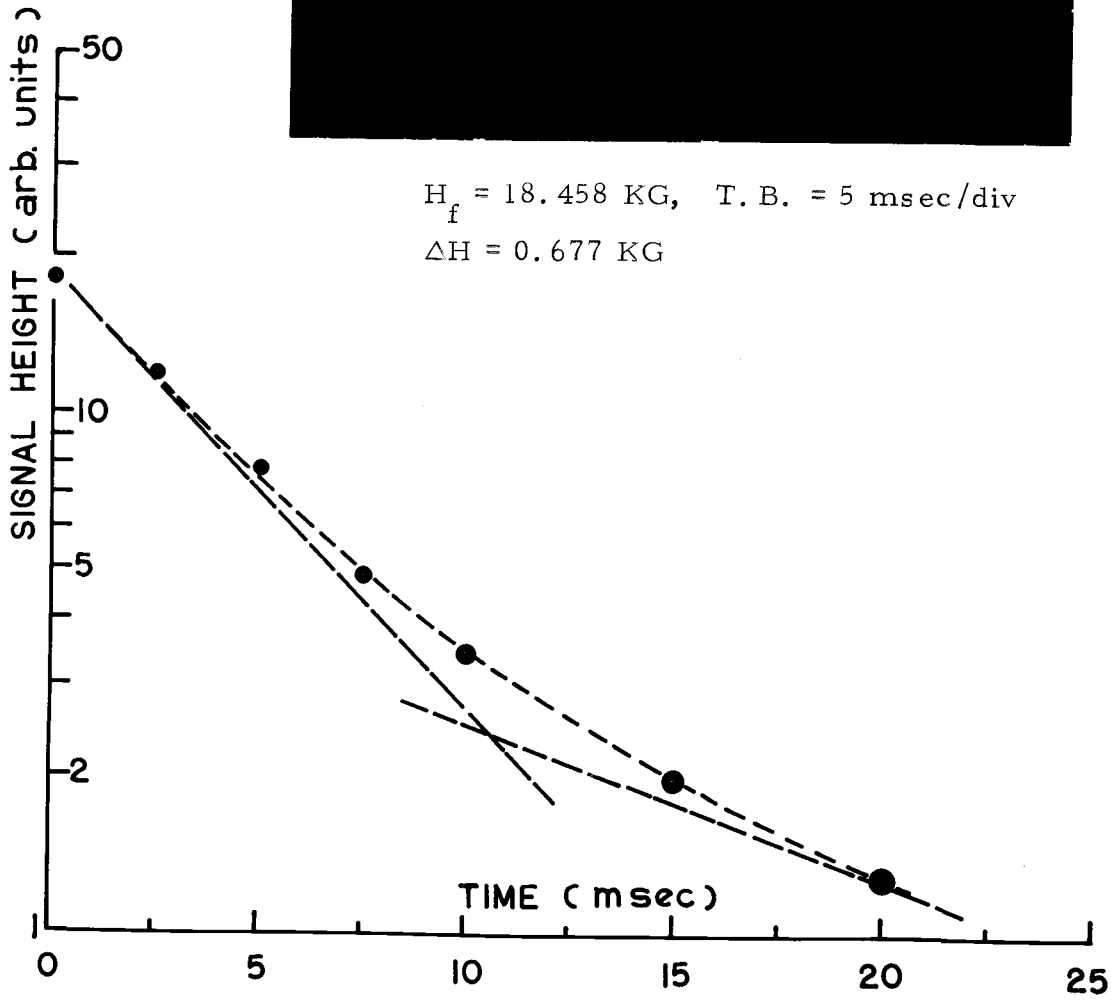

Figure 33. Typical relaxation trace obtained from 0.5%, H‖[100] crystal displaying non-exponential response. The tangents drawn to the curve at t=0 and 20 msec are to show that no single slope is obtainable.

17 KG for the 1% crystal and 20 KG for the 3% crystal.

(ii) Recalling eqs. (2-3-1, 2) which are reached under the assumptions $\delta T << T_B$ and $g\beta H << 2kT$, we see that the field limit imposed by the latter condition can probably be set to $g\beta H/2kT \simeq 0.5$ (about 8% off of its hyperbolic tangent value). Therefore, we have the high field limit $H \simeq kT/g\beta \simeq 14$ KG for all cases when taking $T \simeq 2^{\circ}K$ and $g \simeq 2$.

5-3. Temperature Dependence of the Kapitza Resistance

Systematic measurement of the temperature dependence of r_k has not been attempted due to the small temperature range (only some fraction of a degree under the λ-point of He^4) available for our experiment. Nevertheless, r_k measured at two different temperatures (1.99 and 2.06°K) within this range for the 1%, H//[100] crystal does show a temperature dependence as indicated in §5-2(2). We list them with other r_k's obtained in this range in the following table, where we have used "o" to indicate the value of a single measurement taken at the lower field margin (H_f = 2.73 KG) and "x" the average value of a number of measurements. It should be noted that the errors on single measurement values arise from the error in τ (note that $r_k = \tau/C_c$) associated with the attendant noise imposed on the trace. This has an entirely different meaning from the average deviation of the mean of collective measurements. However, we considered the "o" points

Table 5. Values of r_k of the 1% crystals at different temperatures.

T (^oK)	r_k (10^{-6} $^oK \cdot sec/erg$)	Remarks
1.80	2.43 ± 0.23	o
1.85	1.97 ± 0.12	o
1.90	1.88 ± 0.09	o
1.95	1.65 ± 0.10	o
1.96	1.31 ± 0.09	o
1.99	1.28 ± 0.08	x
2.00	1.34 ± 0.07	o
2.05	1.01 ± 0.03	x
2.06	0.90 ± 0.05	x

only as reference in determining the temperature behavior of r_k. The plot of $\ln(r_k)$ versus $\ln(T)$ is given in Fig. 34. Its slope, m, is about $-(7.5 \pm 2.0)$. The result obtained by Glättli (23) for the case of CeES is that $2.6 \leq m \leq 4.2$. In his experiment, a much more accurate determination of m was possible because of the larger temperature range utilized. Results on other dielectrics such as quartz measured by Challis et al. (19) and Kuang (57), and lithium fluoride by Johnson et al. (58) reveal an m never larger than 4. In addition to the experimental results, the now-existing theories of Khalatnikov (18) and Challis et al. (19) predict that r_k varies with T^{-3} and $T^{-4.2}$, respectively. All these facts favor taking the lower value of our m, $m = -5.5$, although higher values are not definitely precluded. Taking

$m = -5.5$ with T given in units of ^{o}K, $r_k(T)$ calculated from Fig. 34 yields the following expression

$$r_k(T) \equiv R_K/S = 50.65 \times 10^{-6}\ T^{-5.5}\ \ ^{o}K\cdot sec/erg\ , \qquad (5\text{-}3\text{-}1)$$

which at $T = 2^{o}K$ is $1.12 \times 10^{-6}\ ^{o}K\cdot sec/erg$ and equivalent to $R_k = 11.2 \times 10^{-7}\ ^{o}K\cdot cm^2\cdot sec/erg = 11.2\ ^{o}K\cdot cm^2/Watt$, if S is taken to be $1\ cm^2$.

According to Khalatnikov's theory (18), the most important mechanism for the heat exchange between a solid body and the liquid helium II is the radiation of the thermal vibration (sound) from the vibrating surface of the solid and the expression for the Kapitza resistance R_k per unit interfacial area S for a solid of density ρ and transverse velocity c_t, in contact with helium II of density ρ' and velocity of sound c' is

$$r_k \equiv \frac{R_k}{S} = \frac{\delta T}{Sf} = \frac{15h^3\rho\, c_t^3}{16\pi^5 k^4 \rho' c' F T^3 S}\ , \qquad (5\text{-}3\text{-}2)$$

where $f \equiv \dot{Q}/S$, $\dot{Q}$ is the heat flow, and F is a function of the ratio of transverse to longitudinal sound velocities and is about 1.5 (or slightly larger) for most solids. Since $\rho\, c_t^3 \simeq \rho\, v^3 = 4\pi k^3 M\theta_D/3h^3$, where v is the average velocity of sound and M is the molecular weight, eq. (5-3-2) can be re-expressed by, when $S = 1\ cm^2$,

$$r_k = 5M\theta_D^3/4\pi^4 k\rho' c' F T^3 \propto M\theta_D^3\ . \qquad (5\text{-}3\text{-}3)$$

Quartz has $\theta_D = 469^{o}K$ (59) which is very close to $505^{o}K$ for CaF_2,

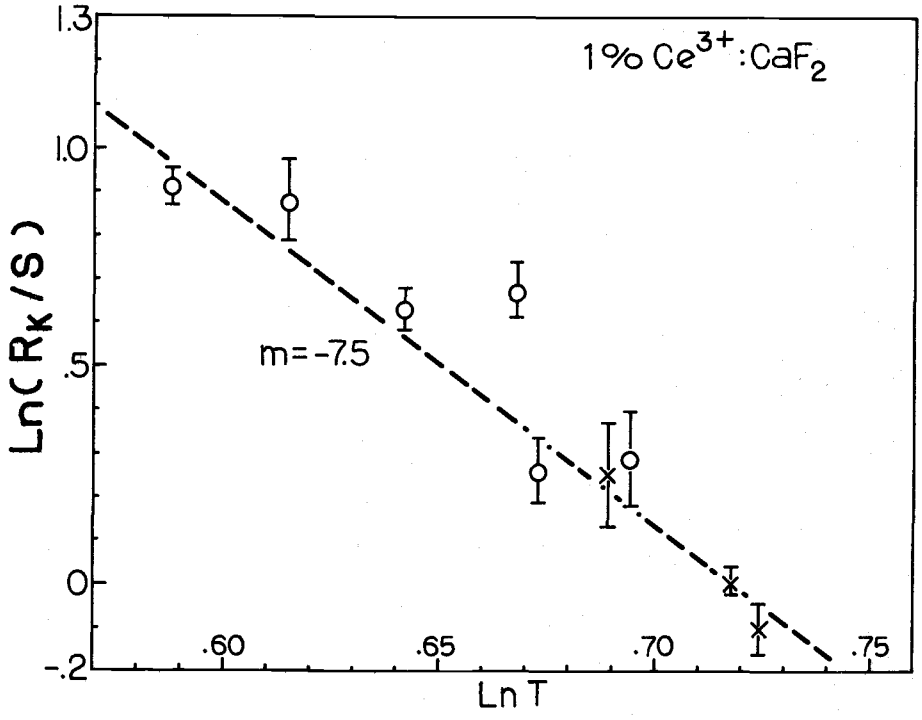

Figure 34. Plot of $\ln(R_k/S)$ versus $\ln T$ to estimate the temperature dependence of r_k.

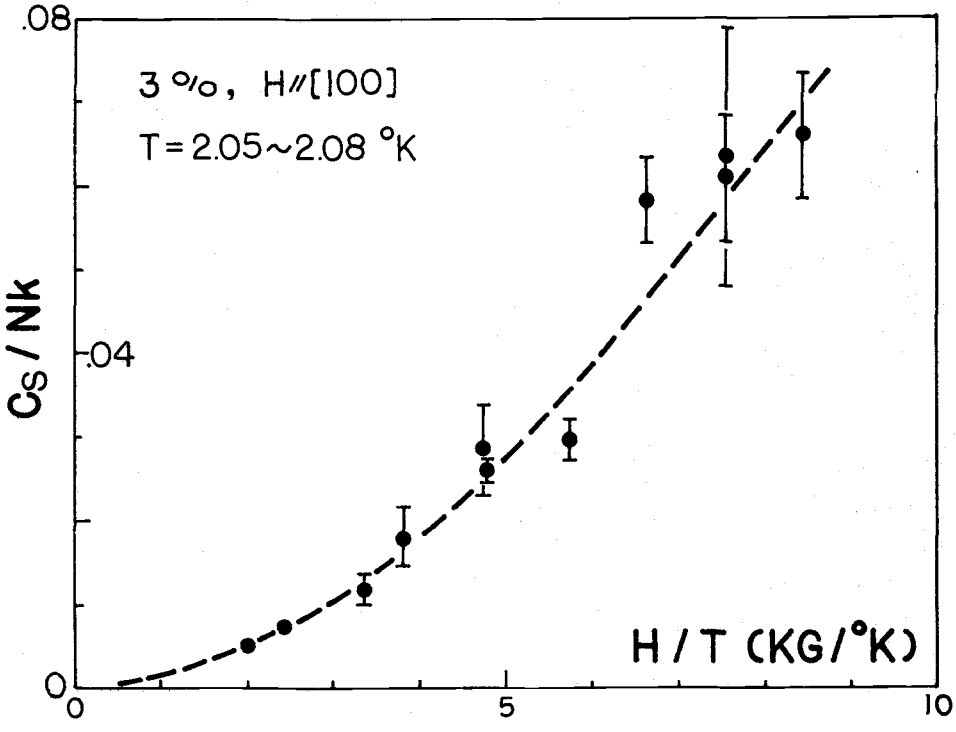

Figure 35. Schottky specific heat of 3%, H//[100] crystal.

$R_k \simeq 2.4\ cm^2 \cdot {}^\circ K/Watt$ at $T = 2^\circ K$ (19), and a very close molecular weight 60.1 gm/mole to 78.1 gm/mole for CaF_2. Assuming they take the same value of F, r_k of CaF_2 calculated from eq. (5-3-3) by the aid of R_k of SiO_2 yields the value $2.4 \times (78.1/60.1) \times (505/469)^3 \simeq 3.9^\circ K/Watt$. This value is about three times as small as our measured $r_k \simeq 11.2^\circ K/Watt$ and is probably due to different surface conditions (over which we have little control), the not so well-matched temperature dependence of our r_k, and the incompleteness of the acoustic mismatch theory.

5-4. Specific Heat of the Spin System in the 3% Ce^{3+}:CaF_2 Crystal

So far, we have not discussed the 3% crystal because of the lack of detailed knowledge about its Schottky specific heat. We now proceed to determine it from the known r_k of the 1% crystals. The average r_k for the 1%, H//[100] crystal at $T = 2.06^\circ K$ is 0.90×10^{-6} $^\circ K \cdot sec/erg$ and that for the H//[111] crystal at $T = 2.05^\circ K$ is 1.01×10^{-6} $^\circ K \cdot sec/erg$. Since the majority of the T's of the 3%, H//[100] crystal are measured at $T = 2.05^\circ K$, we therefore assume $r_k = 1 \times 10^{-6}$ $^\circ K \cdot sec/erg$ is a reasonable value for this crystal. Assuming that the present model applies, the specific heat of the spin system can be calculated from $C_s = C_c - C_L = (T/r_k) - C_L$ at $2.05^\circ K$. The result (C_s/Nk vs. H/T) is given in Fig. 35.

6. CONCLUSIONS

In light of the results and discussions of the spin-bath relaxation study on Ce^{3+} x at. %:CaF_2, the following conclusions were reached:

(1) The spin-lattice relaxation time, T_1, of Ce^{3+}:CaF_2 is extremely rapid (< 100 μsec at $T \simeq 2^{\circ}K$ in fields higher than 300 gauss for all samples used), an observation which the theory of common relaxation processes does not predict. Becker et al. (60) have explained the anomalous phonon effects on specific heat and rapid spin-lattice relaxation in concentrated CeES using a thermodynamic Green's function approach for incoherent spins and phonons. While it seems doubtful that our system of Ce^{3+}:CaF_2 satisfies all the conditions necessary for a proper application of this method; nevertheless, a start has been made theoretically to explain the unexpected rapid spin-lattice relaxation of trivalent cerium.

(2) Incorrect identification of spin-bath relaxation time, τ, with spin-lattice relaxation time T_1 can be made unless a sufficient examination of field dependence is made, since the return to equilibrium of a strongly coupled spin-phonon system experiencing Kapitza limitation proceeds in an exponential fashion within the range of field and temperature examined in this thesis.

(3) The experimental method provides us with a means of determining the rise in lattice temperature during the relaxation process as described in §5-2(3)(ii). An explicit example giving the order of magnitude of the temperature rise, δT, of the 1% crystals can be taken by setting H_i = 10 KG (this is in the region of $\gamma \longrightarrow \infty$) and ΔH = 0.3 KG at $T_B = 2^{\circ}K$. In this case δT is approximately equal to $(\Delta H/H_i)T_B \simeq 0.06^{\circ}K$ (i.e., 3% of T_B).

(4) As the result of item (3), the possibility arises that the field switching method may serve as a means of contactless heating of dielectrics through the intermediary of implanted paramagnetic impurities.

(5) Different methods of establishing thermal contact between the host crystal and reservoir (different surface conditions) can give rise to much of the variation seen by different investigators in relaxation time measurements on a given system. The relaxation times (τ vs. T) of $Ce^{3+}:CaF_2$ measured by Bierig et al. (12) show an overall faster τ than ours. Their samples were mounted on a high heat conducting sapphire tube connected to a microwave cavity which was itself in contact with the reservoir by means of helium exchange gas. Others have mounted samples directly to the cavity.

(6) Regardless of a poorly defined $r_k = r_k(T)$, a rather good relative dependence of C_s ($\simeq C_c = T/r_k$) at fixed T on magnetic field can be determined. The Schottky specific heat, C_s/Nk, of the 3% Ce^{3+} spin system in CaF_2 so determined was found to be 0.05 at a H/T value of 7 KG/^oK. Thus, the Schottky specific heat for any complicated system with known r_k which obeys the conditions of rapid spin-lattice relaxation in the range of H/T where $C_c \simeq C_s >> C_L$ can be measured by our dynamic method.

(7) The CaF_2 crystal exhibits a somewhat larger Kapitza resistance R_k ($\simeq$ 11 $cm^2 \cdot {}^oK$/Watt for S = 1 cm^2) than dielectrics examined hitherto. This could be ascribed to the relatively higher θ_D and the degree of roughness of our crystal surface.

Some recommendations for future research can be suggested on the basis of our experimental method:

(1) It seems natural that similar studies can be extended to other rare-earth ions if the sensitivity of the apparatus is improved. Indeed, the divalent europium ion, Eu^{2+}, in CaF_2 could be done with the present setup. This system is known to possess a fairly large paramagnetic Faraday rotation (61). Eu^{2+} is a Kramers ion having a ground state $^8S_{7/2}$ and being divalent is spared the complications arising from charge compensation when doped into CaF_2. The

complications, however, in this case are two-fold; first, it is difficult to obtain a pure Eu^{2+}-doped crystal without the presence of Eu^{3+} (ground state $^7F_0$ which exhibits only diamagnetic Faraday rotation not detectable by our apparatus), and secondly, the ground state of $Eu^{2+}:CaF_2$ is an octet, all levels of which in moderate magnetic field are populated at liquid helium temperatures.

(2) Lee (62) has recently formulated the thermodynamic properties of spin-phonon interactions in a paramagnetic system in a self-consistent manner using a variational principle for the free energy. A phase transition qualitatively similar to a structural phase transition should occur at a temperature T_0 determined by the strength of the spin-phonon coupling, characterized by a parameter ξ, and the Zeeman energy spacing, $g\beta H_0$. For a given $\xi^2 > 1$, which corresponds to a strong coupling condition, they are related by $\xi^{-2} = \tanh(g\beta H_0/2kT_0)$. Although his treatment seems to predict that such a phase transition will occur for all systems as long as their spin-lattice coupling is strong, the effect has so far been found only in few rare-earth compounds (63). Another consequence of Lee's results is that the spin specific heat, C/Nk, rises from $T = 0^{\circ}K$ to a peak at T_0, abruptly drops off to the value of the normal Schottky specific heat and continues for $T > T_0$ with the tail of the unperturbed Schottky specific heat. If now C/Nk is plotted against H/T for a given

T and ξ, one sees that the specific heat obeys the unperturbed Schottky curve at low fields until the value of H defining T_0 (i.e., $H = (H_0/T_0)T = (2kT/g\beta)\tanh^{-1}(\xi^{-2})$ at T) is reached. It then suddenly jumps to a higher point and subsequently decreases from there on as H increases. It is, therefore, noteworthy that our experimental method could quite possibly map out the specific heat as a function of H at fixed T in an effort to detect the discontinuity (sudden enhancement in C/Nk) associated with the crystal (structural) phase transition.

(3) To gain a more precise knowledge of the temperature dependence of R_k for CaF_2 as well as its absolute magnitude, a series of experiments should be conducted on crystals whose surfaces have been prepared under well controlled conditions. Such results will be important for any accurate determination of the actual temperature of CaF_2 under conditions of thermal conduction at liquid helium temperatures.

BIBLIOGRAPHY

1. Kalbfleisch, H. 1964. Paramagnetische relaxation in holmium und dysprosium-äthylsulfat. Zeitschrift für Physik 181:12-13.

2. Becher, W. and Kalbfleisch, H. 1970. An apparatus for non-resonant measurements of magnetic relaxation times as short as 10 μsec by use of a superconducting coil. Physica Status Solidi (a) 2:109-13.

3. Daniels, J.M. and Rieckhoff, K.E. 1960. Spin lattice relaxation in neodymium ethylsulphate at liquid helium temperatures. Canadian Journal of Physics 38:604-15.

4. Kastler, A. 1951. La détection optique de la résonance électronique paramagnétique par la mesure de la polarisation rotatoire paramagnétique d'une radiation visible. Comptes Rendus 232:953-5.

5. Opechowski, W. 1953. Magneto-optical effects and paramagnetic resonance. Reviews of Modern Physics 25:264-8.

6. Daniels, J.M. and Wesemeyer, H. 1958. The influence of paramagnetic resonance saturation on the Faraday effect. Canadian Journal of Physics 36:405-6.

7. Rieckhoff, K.E. and Griffiths, D.J. 1963. Optical Faraday rotation studies of paramagnetic resonance in neodymium ethylsulphate. Canadian Journal of Physics 41:33-45.

8. Griffiths, D.J. and Glättli, H. 1965. Optical Faraday rotation studies of paramagnetic resonance and relaxation in praseodymium ethylsulphate. Canadian Journal of Physics 43:2361-73.

9. Kahle, H.G., Kalbfleisch, H., and Kump, U. 1965. Paramagnetische relaxation und phonon-engpass im terbium-äthylsulfat. Zeitschrift für Physik 188:193-8.

10. Kahle, H.G., Kalbfleisch, H., and Stein, E. 1967. Paramagnetic relaxation and observation of a phonon bottleneck in terbium ethyl sulfate. Physica Status Solidi 22:537-40.

11. Baker, J.M., Hayes, W., and Jones, D.A. 1959. Paramagnetic resonance of impurities in CaF_2. Proceedings of the Physical Society (London) 73:942-5.

12. Bierig, R.W., Weber, M.J., and Warshaw, S.I. 1964. Paramagnetic resonance and relaxation of trivalent rare-earth ions in calcium fluoride. II. Spin-lattice relaxation. Physical Review 134:A1504-16.

13. Zapasskii, V.S. 1972. Spin-lattice relaxation mechanisms in the crystal CaF_2-Dy^{3+} (I). Soviet Physics - Solid State 14: 1069-70.

14. Zapasskii, V.S. and Feofilov, P.P. 1974. Magnetooptic investigations of the spin system in a CaF_2:Dy^{3+} (I) crystal. Soviet Physics - Solid State 15:1642-6.

15. Zapasskii, V.S. and Klimachev, A.F. 1974. Orientational dependence of the spin-lattice relaxation times in a CaF_2:Dy^{3+} (I) crystal. Soviet Physics - Solid State 15:1647-9.

16. Sabisky, E.S. and Anderson, C.H. 1970. Spin-lattice relaxation of Tm^{2+} in CaF_2, SrF_2, and BaF_2. Physical Review B 1:2028-40.

17. Kapitza, P.L. 1941. The study of heat transfer in helium II. Journal of Physics (U.S.S.R.) 4:181-210.

18. Khalatnikov, I.M. 1952. Heat exchange between a solid body and helium II. Zhurnal Eksperimental' noĭ ĭ Theoreticheskoi Fiziki 22:687-704.

19. Challis, L.J., Dransfeld, K., and Wilks, J. 1961. Heat transfer between solids and liquid helium II. Proceedings of the Royal Society (London) A260:31-45.

20. Pollack, G.L. 1969. Kapitza resistance. Reviews of Modern Physics 41:48-80.

21. Challis, L.J. 1974. Kapitza resistance and acoustic transmission across boundaries at high frequencies. Journal of Physics C: Solid State Physics 7:481-95.

22. Van den Broek, J. and Van der Marel, L.C. 1963. Spin lattice relaxation in rare-earth ethylsulphate, I. Physica 29:948-64.

23. Glättli, H. 1968. Kapitza resistance of cerium ethylsulphate. Canadian Journal of Physics 47:103-9.

24. Atsarkin, V.A. 1968. Role of finite lattice heat capacity and Kapitz thermal resistance in paramagnetic relaxation under phonon superheating condition. Soviet Physics JETP 26:149-52.

25. Lang, R.J. 1936. The spectrum of trebly ionized cerium. Canadian Journal of Research A14:127-30.

26. Bleaney, B., Llewellyn, P.M., and Jones, D.A. 1956. Paramagnetic resonance of uranium ions. Proceedings of the Physical Society (London) 69B:858-60.

27. Batchelder, D.N. and Simmons, R.O. 1964. Lattice constants and thermal expansivities of silicon and of calcium fluoride between 6° and 322°K. Journal of Chemical Physics 41:2324-9.

28. Stevens, K.W.H. 1952. Matrix elements and operator equivalents connected with the magnetic properties of rare earth ions. Proceedings of the Physical Society (London) 65A:209-15.

29. Kramers, H.A. 1930. Théorie générale de la rotation paramagnétique dans les cristaux. Proceedings of the Koninklijke Nederlandse Akademie van Wetenschappen te Amsterdam 33:959-72.

30. Manthey, W.J. 1973. Crystal field and site symmetry of trivalent cerium ions in CaF_2: The C_{4v} and C_{3v} centers with interstitial-fluoride charge compensator. Physical Review B 8:4086-98.

31. Weber, M.J. and Bierig, R.W. 1964. Paramagnetic resonance and relaxation of trivalent rare-earth ions in calcium fluoride. I. Resonance spectra and crystal fields. Physical Review 134:A1492-503.

32. Bleaney, B. 1959. A new class of materials for Bloembergen-type masers. Proceedings of the Physical Society (London) 73:937-9.

33. Dvir, M. and Low, W. 1960. Paramagnetic resonance spectra of impurities in calcium fluoride. Proceedings of the Physical Society (London) 75:136-8.

34. Waller, I. 1932. Über die magnetisierung von paramagnetischen kristallen in wechsilfeldern. Zeitschrift für Physik 79:370-88.

35. Kronig, R. de L. 1939. On the mechanism of paramagnetic relaxation. Physica 6:33-43.

36. Van Vleck, J.H. 1940. Paramagnetic relaxation times for titanium and chrome alum. Physical Review 57:426-47.

37. Mattuck, R.D. and Strandberg, M.W.P. 1960. Spin-phonon interaction in paramagnetic crystals. Physical Review 119:1204-17.

38. Orbach, R. 1961. Spin-lattice relaxation in rare-earth salts. Proceedings of the Royal Society (London) A264:458-84.

39. Scott, P.L. and Jeffries, C.D. 1962. Spin-lattice relaxation in some rare-earth salts at helium temperatures; observation of the phonon bottleneck. Physical Review 127:32-51.

40. Bernstein, E.R. and Franceschetti, D.R. 1974. Spin-lattice relaxation in an isotropic elastic continuum with spherical lattice waves and a cubic crystal field. Physical Review B 9:3678-704.

41. Van Vleck, J.H. 1941. Paramagnetic relaxation and the equilibrium of lattice oscillators. Physical Review 59:724-9.

42. Faughnan, B.W. and Strandberg, M.W.P. 1961. The role of phonons in paramagnetic relaxation. Journal of Physics and Chemistry of Solids 19:155-65.

43. Stoneham, A.M. 1965. The phonon bottleneck in paramagnetic crystals. Proceedings of the Physical Society (London) 86:1163-77.

44. Wooldridge, J. 1969. Optical detection of a phonon bottleneck in Nd-doped lanthanum ethyl sulfate. Physical Review 185:602-10.

45. Becquerel, H. 1897. Sur une interprétation applicable au phénoméne de Faraday et au phénoméne de Zeeman. Comptes Rendus 125:679-85.

46. Kramers, H.A. and Heisenberg, W. 1925. Über die streuung von strahlung durch atome. Zeitschrift für Physik 31:681-708.

47. Rosenfeld, L. 1930. Zur theorie des Faradayeffekts. Zeitschrift für Physik 57:835-54.

48. Van Vleck, J.H. and Hebb, M.H. 1934. On the paramagnetic rotation of tysonite. Physical Review 46:17-32.

49. Bloembergen, N., Pershan, P.S., and Wilcox, L.R. 1960. Microwave modulation of light in paramagnetic crystals. Physical Review 120:2014-23.

50. Shen, Y.R. 1964. Faraday rotation of rare-earth ions. I. Theory. Physical Review 133:A511-15.

51. Griffiths, D.J. 1971. An optical magnetometer for superconductivity measurements. The Review of Scientific Instruments 42:444-7.

52. Griffiths, D.J. 1972. Paramagnetic relaxation initiated by flux jumping. Physics Letters 41A:21-2.

53. Gordon, J.P. 1961. Variable coupling reflection cavity for microwave spectroscopy. The Review of Scientific Instruments 32:658-61.

54. Baker, J.M., Bleaney, B., and Hayes, W. 1958. Paramagnetic resonance of S-state ions in calcium fluoride. Proceedings of Royal Society (London) A247:141-51.

55. Debye, P. 1912. Theory of specific heats. Annalen der Physik 39:789-839.

56. Huffman, D.R. and Norwood, M.H. 1960. Specific heat and elastic constants of calcium fluoride at low temperatures. Physical Review 117:709-13.

57. Kuang, W.-Y. 1962. An investigation of the temperature discontinuity at the boundary between a solid and superfluid helium. Soviet Physics JETP 15:635-45.

58. Johnson, R.C. and Little, W.A. 1963. Experiments on the Kapitza resistance. Physical Review 130:596-604.

59. Jones, G.H.S. and Hollis Hallett, A.C. 1960. The specific heat of crystalline quartz between 2°K and 4°K. Canadian Journal of Physics 38:696-700.

60. Becker, E. and Clover, R.B. 1968. Anomalous phonon effects on specific heat and spin-lattice relaxation in cerium ethyl sulfate. Physical Review Letters 21:1327-31.

61. Shen, Y.R. and Bloembergen, N. 1964. Faraday rotation of rare-earth ions in CaF_2. II. Experiments. Physical Review 133:A515-20.

62. Lee, B.S. 1973. Thermodynamic properties of spin-phonon interactions in a paramagnetic system. Journal of Low Temperature Physics 13:81-104.

63. Elliott, R.J., Harley, R.T., Smith, S.R.P., and Hayes, W. 1972. Raman scattering and theoretical studies of Jahn-Teller induced phase transitions in some rare-earth compounds. Proceedings of Royal Society of London A328:217-66.